Development, Assembly and Characterization of ELIPS for ELI-NP

Entwicklung, Aufbau und Charakterisierung von ELIPS für ELI-NP
Zur Erlangung des Grades eines Doktors der Naturwissenschaften (Dr. rer. nat.)
Genehmigte Dissertation von Ilja Homm aus Karatau
Tag der Einreichung: 23.01.2023, Tag der Prüfung: 13.02.2023

1. Gutachten: Prof. Dr. Thorsten Kröll
2. Gutachten: Prof. Dr. Joachim Enders
Darmstadt, Technische Universität Darmstadt

TECHNISCHE UNIVERSITÄT DARMSTADT

Fachbereich Physik
Institut für Kernphysik
AG Kröll

Development, Assembly and Characterization of ELIPS for ELI-NP
Entwicklung, Aufbau und Charakterisierung von ELIPS für ELI-NP

Accepted doctoral thesis by Ilja Homm

Date of submission: 23.01.2023
Date of thesis defense: 13.02.2023

Darmstadt, Technische Universität Darmstadt

Bitte zitieren Sie dieses Dokument als:
URN: urn:nbn:de:tuda-tuprints-240417
URL: http://tuprints.ulb.tu-darmstadt.de/24041
Jahr der Veröffentlichung auf TUprints: 2023

Dieses Dokument wird bereitgestellt von tuprints,
E-Publishing-Service der TU Darmstadt
http://tuprints.ulb.tu-darmstadt.de
tuprints@ulb.tu-darmstadt.de

Erklärungen laut Promotionsordnung

§ 8 Abs. 1 lit. c PromO

Ich versichere hiermit, dass die elektronische Version meiner Dissertation mit der schriftlichen Version übereinstimmt.

§ 8 Abs. 1 lit. d PromO

Ich versichere hiermit, dass zu einem vorherigen Zeitpunkt noch keine Promotion versucht wurde. In diesem Fall sind nähere Angaben über Zeitpunkt, Hochschule, Dissertationsthema und Ergebnis dieses Versuchs mitzuteilen.

§ 9 Abs. 1 PromO

Ich versichere hiermit, dass die vorliegende Dissertation selbstständig und nur unter Verwendung der angegebenen Quellen verfasst wurde.

§ 9 Abs. 2 PromO

Die Arbeit hat bisher noch nicht zu Prüfungszwecken gedient.

Darmstadt, 23.01.2023

I. Homm

Abstract

The field of nuclear physics is generally concerned with the study of the structure and dynamics of nuclei. ELI-NP will be able to deliver photons with energies of a few keV up to 19.5 MeV for this kind of fundamental research. The nuclei to be studied will be excited by the photons and the subsequent decay observed in the form of γ rays in germanium detectors, which offer the highest energy resolution up to date. During the interaction of γ radiation with matter effects occur in the germanium detectors, which increase the background in a spectrum. These can be reduced by using a combination of scintillation crystals with semiconductor diodes around the detector, as a so-called anti-Compton shield (ACS).

For gamma quanta with high energies the pair production is the dominant interaction process in matter. In the case of germanium this energy lies at 8 MeV. The produced positrons escape from the material or annihilate with the electrons from the surrounding and two 511 keV γ quanta are generated and emitted in opposite directions. This can lead generally to the case that one of those quanta, as well as both, can escape out of the detector and thus do not deposit the full energy of the primary gamma quantum. Thereby single-escape and double-escape peaks arise that make the recorded spectrum more complex. Another source of background is Compton scattering. Here, the incident photon is scattered out of the detector without having deposited all of its energy in it. To prevent this impurities, as well as to reduce the Compton background, often an ACS out of an efficient material (mostly BGO) to stop gamma quanta is built around a detector. Coincident events from HPGe detector and ACS will be neglected whereby the spectrum becomes cleaner.

The present work is about the development, the assembly and the characterization of a HPGe-BGO pair spectrometer, also called ELIPS (**ELI**-NP **P**air **S**pectrometer), on the gamma beam of ELI-NP in Bucharest-Magurele, Romania. The ELI-NP is an unique European research facility, which should in future provide among other things brilliant gamma radiation with high intensity up to an energy of 19.5 MeV. ELIADE is there an important instrument for the γ-spectroscopic study of photonuclear reactions and consists of 8 HPGe-clover detectors. With the help of the pair spectrometer the efficiency of one of those detectors at high energies should be increased and hence the high-resolution gamma spectroscopy extended. The use of 64 BGO crystals makes the pair spectrometer an improved version of an ACS as it allows a more accurate determination for the position of the gamma quanta. Coincident events from, for example, two 511 keV γ rays in two opposing BGO crystals and one double-escape energy in the HPGe detector can be considered as one

coherent process and thus the full energy of the primary gamma ray can be reconstructed, but at the expense of statistics. However, the higher granularity also requires additionally smaller readout electronics to ensure the mechanical compatibility with ELIADE, for which reason MPPC arrays are used for this purpose.

ELIPS can also be used as a stand-alone device. By inserting of a target instead of a HPGe detector into the spectrometer, it can be used as an intensity monitor for a gamma beam or for instance for the investigation of the pair-production cross section close to the threshold.

The first experiments with the completed pair spectrometer were performed for testing purposes at the TU Darmstadt, at the institute for nuclear physics in Cologne, as well as at the institute Laue-Langevin in Grenoble. The results of these tests are presented in this work.

Zusammenfassung

Der Bereich der Kernphysik beschäftigt sich im Allgemeinen mit der Untersuchung der Struktur und der Dynamik von Kernen. ELI-NP wird Photonen mit Energien von wenigen keV bis zu 19.5 MeV für diese Art von Grundlagenforschung liefern können. Die zu untersuchenden Kerne werden dabei von den Photonen angeregt und der anschließende Zerfall in Form von Gammastrahlung in Germanium-Detektoren, die bis heute die höchste Energieauflösung bieten, beobachtet. Bei der Wechselwirkung von Gammastrahlung mit Materie kommt es in den Germanium-Detektoren zu Effekten, die den Untergrund in einem Spektrum erhöhen. Diese können durch den Einsatz einer Kombination von Szintillationskristallen mit Halbleiterdioden um den Detektor, als ein sogenanntes Anti-Compton-Schild (ACS), reduziert werden.

Für Gammaquanten mit hohen Energien ist die Paarbildung der dominante Wechselwirkungsprozess in Materie. Im Falle von Germanium liegt diese Energie bei 8 MeV. Die entstehenden Positronen entkommen aus der Materie oder annihilieren mit den Elektronen aus der Umgebung und es entstehen zwei 511-keV-γ-Quanten, die in entgegengesetzte Richtungen emittiert werden. Dies kann im Allgemeinen dazu führen, dass eins dieser Quanten, oder auch beide, aus dem Detektor entkommen können und somit nicht die volle Energie des primären Gammaquants deponiert wird. Dadurch entstehen sogenannte Single-Escape- und Double-Escape-Peaks, die das aufgenommene Spektrum komplexer machen. Eine weitere Quelle für Untergrund ist die Compton-Streuung. Hierbei wird das einfallende Photon aus dem Detektor herausgestreut ohne seine gesamte Energie darin deponiert zu haben. Um diesen Verunreinigungen vorzubeugen, sowie Compton-Untergrund zu verringern, wird oftmals ein ACS aus einem effizienten Material (meist BGO) zum Stoppen von Gammaquanten um einen Detektor gebaut. Koinzidente Events von HPGe-Detektor und ACS werden unterdrückt, wodurch das Spektrum sauberer wird.

In der vorliegenden Arbeit geht es um die Entwicklung, den Aufbau und die Charakterisierung eines HPGe-BGO-Paarspektrometers, auch ELIPS (**ELI**-NP **P**aar**S**pektrometer) genannt, am Gammastrahl von ELI-NP in Bukarest-Magurele, Rumänien. Das ELI-NP ist eine einzigartige europäische Forschungseinrichtung, die in Zukunft u. a. brillante Gammastrahlung mit hoher Intensität bis zu einer Energie von 19.5 MeV liefern soll. ELIADE ist dort ein wichtiges Instrument zur gammaspektroskopischen Untersuchung von photonuklearen Reaktionen und besteht aus 8 HPGe-Clover-Detektoren. Mithilfe des Paarspektrometers soll die Effizienz von einem dieser Detektoren bei hohen Energien erhöht und somit die hochauflösende Gammaspektroskopie erweitert werden. Durch die Verwendung von 64

BGO-Kristallen wird das Paarspektrometer zu einer verbesserten Version eines ACS, da eine genauere Positionsbestimmung für die Gammaquanten ermöglicht wird. Koinzidente Ereignisse aus beispielsweise zwei 511-keV-Gammastrahlen in zwei gegenüberliegenden BGO-Kristallen und einer Double-Escape-Energie im HPGe-Detektor können als ein zusammenhängender Vorgang betrachtet und somit die volle Energie des primären Gammastrahls rekonstruiert werden, allerdings auf Kosten von Statistik. Die höhere Granularität erfordert jedoch auch zusätzlich eine kleinere Ausleseelektronik um die mechanische Kompatibilität mit ELIADE zu gewährleisten, weshalb MPPC-Arrays dazu benutzt werden.

ELIPS kann auch alleinstehend verwendet werden. Durch das Einsetzen eines Targets anstatt des HPGe-Detektors in das Spektrometer kann es als Intensitätsmonitor für einen Gammastrahl benutzt werden oder z.B. zur Untersuchung des Wirkungsquerschnitts für Paarproduktion nahe an der Schwelle.

Die ersten Experimente mit dem fertigen Paarspektrometer wurden zu Testzwecken an der TU Darmstadt, am Institut für Kernphysik in Köln, sowie am Institut Laue-Langevin in Grenoble durchgeführt. Die Ergebnisse dieser Tests werden in dieser Arbeit vorgestellt.

Contents

1. Introduction

The **E**xtreme **L**ight **I**nfrastructure (ELI) is a research facility of the EU countries which works with the most intense laser beams in the world and currently consists of three pillars - ELI Beamlines, ELI Attosecond and the ELI-NP. The latter is the **E**xtreme **L**ight **I**nfrastructure - **N**uclear **P**hysics facility which has been built recently in Bucharest-Magurele, Romania [1] (see Fig. 1.1). This facility is going to do research in the field of nuclear physics in combination with high power lasers and already collaborates with more than 70 industrial and research institutions worldwide [1]. The **V**ariable **E**nergy **GA**mma (VEGA) system at ELI-NP will be used to create high-energy γ rays of up to $E_\gamma = 19.5$ MeV in a process called "Inverse Compton Scattering" (ICS) [2]. Here, low-energy photons of a few eV emitted by a laser can be boosted continuously to high-energy γ rays through the collision with electrons of an energy up to $E_\mathrm{e} = 742$ MeV. This will provide a very intense and brilliant γ ray beam with an average bandwidth below 0.5 %, a spectral density of more than $5 \cdot 10^3 \ \frac{\text{photons}}{\text{eV} \cdot \text{s}}$ and a linear polarization of ≥ 95 %. With this performance the bandwidth is at least a factor of two smaller and the gamma-ray flux around one order of magnitude higher than the current state-of-the-art systems like for example the High Intensity γ-ray Source (HIγS) at the Duke Free Electron Laser Laboratory (DFELL), which has a bandwidth of a few percent and a maximum total flux of $3 \cdot 10^9 \ \frac{\text{photons}}{\text{s}}$ [3]. These parameters are going to make VEGA one of the most advanced gamma-ray sources in the world. Such specifications will allow further insights into nuclear physics topics like photofission, the decay of the Giant Dipole Resonance (GDR) or the Nuclear Resonance Fluorescence (NRF). As a direct consequence, these new understandings can lead to new opportunities, for example, in fundamental, nuclear and astrophysics. But also in applied research like material science, industrial tomography, radioactive waste management or medical applications which even implicates socio-economic benefits [4]. A key instrument for studying photonuclear reactions with γ spectroscopy will be ELIADE (**ELI**-NP **A**rray of **DE**tectors) (see Fig. 1.2 (a)) [5]. This array consists of 8 clover detectors with four high-resolving 8-fold segmented HPGe (**H**igh-**P**urity **Ge**rmanium) crystals each (see Fig. 1.2 (b)) [6]. For high-energy photons in the order of several MeV, Compton effect and pair production dominate and add additional features to the spectra. A main task of this work is to develop one of those clovers further into a pair spectrometer. The detection of escaping γ rays produced by pair annihilation should extend the high-resolution spectroscopy to higher energies.

Compared to conventional pair spectrometers, which are magnetic spectrometers, that use the momentum of positron and electron to reconstruct the initial photon energy, this

Figure 1.1.: A photo of the new ELI-NP facility in Magurele, Romania, 2019.

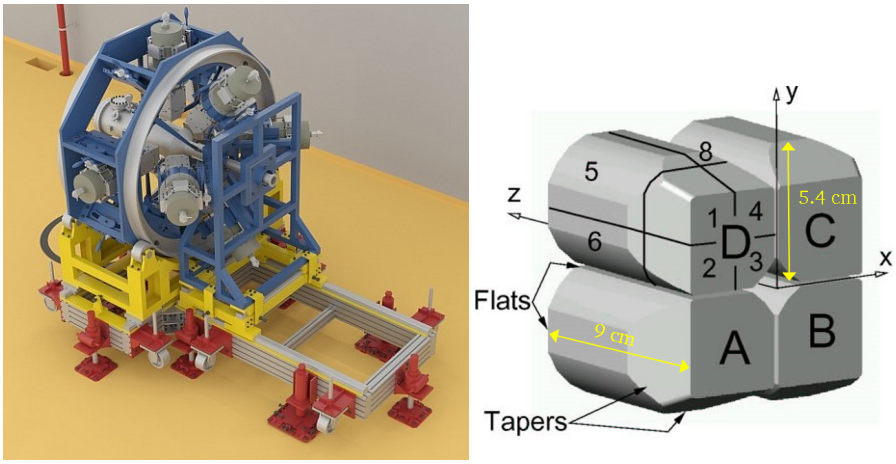

(a) (b)

Figure 1.2.: (a) shows a sketch of the ELIADE array with its 8 clover detectors. Figure (a) is taken from [5]. (b) depicts one clover detector, its dimensions, including the separation in four 8-fold segmented HPGe crystals. Reprinted from [6]. Copyright 2023, with permission from Elsevier.

one is based on the detection of γ rays, only, and does not need additional magnetic fields.

Its working principle is sketched in the following. When an incident gamma ray with an energy above 1022 keV hits the HPGe detector there is a possibility for pair production. The kinetic energy of the produced electron and positron can be detected and the latter annihilates with another electron in the Germanium. The annihilation produces two photons with an energy of 511 keV which are emitted in opposite directions.

For the registration in the detectors several cases need to be distinguished as they produce distinct signals. In the first case both photons could be absorbed by the HPGe detector and the energy of the primary γ ray would be fully reconstructed. This would be visible in the so called "full-energy peak". As second, if one or both of the 511-keV gammas escape the detector, additional lines, the "single-escape peak" or the "double-escape peak", respectively, are visible in the spectrum (see Fig 1.3).

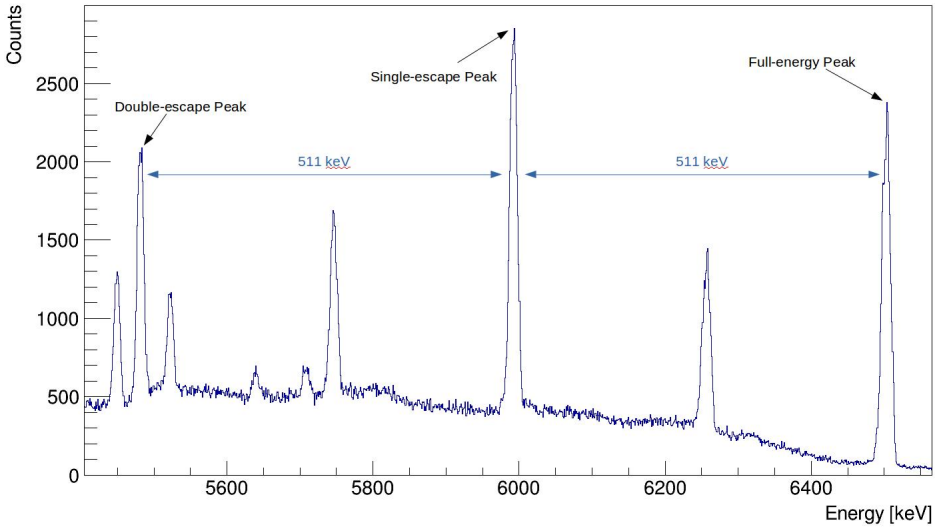

Figure 1.3.: Germanium spectrum with a 6.5 MeV full-energy peak and its corresponding single-escape and double-escape peaks. The data stems from a ^{143}Nd(n,γ) experiment with the EXOGAM setup at ILL in Grenoble, France [7].

To suppress these disturbing additional lines and all combinations, where the γ rays with an energy of 511 keV perform Compton scattering, most HPGe detectors are surrounded by a standard Anti-Compton (AC) shield (see Fig. 1.4), which consists of an efficient scintillator material with a low energy resolution, but high efficiency. All events showing coincidences

between AC shield and HPGe detector can be vetoed thus suppressing Compton background as well as escape peaks stemming from pair annihilation. This suppression improves the peak-to-total ratio ($\frac{P}{T}$), but reduces the statistics, while good events are not affected.

To improve this situation, the AC shield can be upgraded to an escape-γ-rays pair spectrometer. Since two photons with an energy of 511 keV and a 180° correlation, which are detected by the AC shield, are a sign for a double-escape event, the missing energy is known. Therefore during the analysis, 1022 keV can be added to the energy detected in the HPGe detector.

The mandatory, precise spatial resolution requires smaller crystals for the AC shields and thus transforms it to a pair spectrometer. The higher granularity also demands small readout devices to keep the mechanical compatibility with ELIADE. Therefore, **p**hoto**m**ultiplier **t**ubes (PMTs) can not be used in this case.

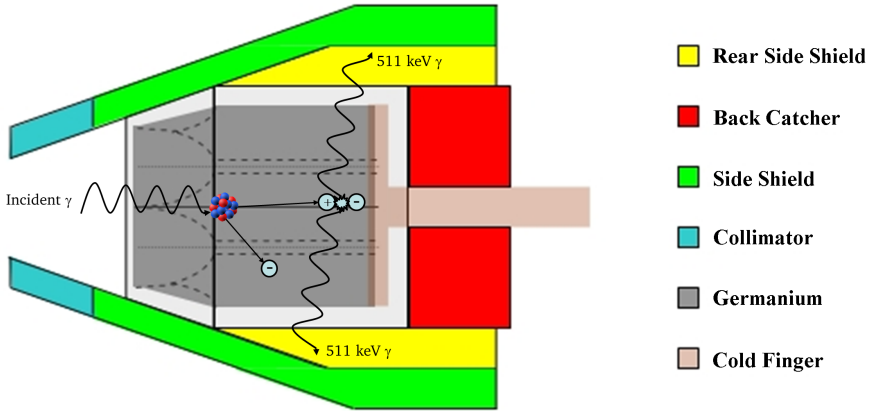

Figure 1.4.: Scheme of Anti-Compton shield surrounding a HPGe clover detector. Pair production process is highlighted. Figure taken from [8] and modified, with courtesy of Călin A. Ur.

Further to this, the pair spectrometer can be used as a γ-ray beam-intensity monitor by exchanging the Germanium crystal with a converter inside the AC shield (see Fig. 1.5). Since this works with various targets the monitoring would be possible for the whole energy range of the γ beam from ELI-NP. With a standard AC shield there is no such possibility due to the bulky crystals that can not provide the information for the 180° correlation from the emitted γ pairs.

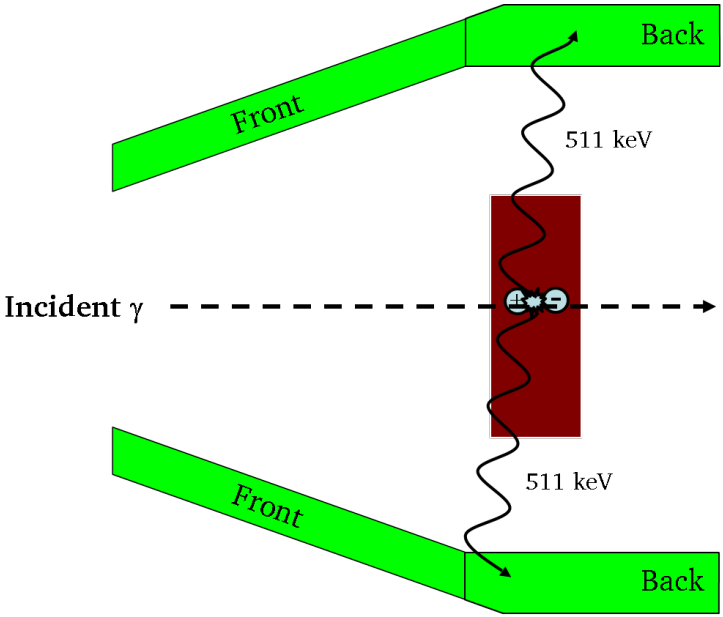

Figure 1.5.: Scheme of the intensity monitor (green) with converter target (brown).

After a successful proof of principle of a pair spectrometer with a HPGe detector surrounded by CsI(Tl) (cesium iodide doped with thallium) crystals in the master's thesis of Ilja Homm [9] the main tasks of this dissertation have been to develop, assemble and characterize an improved version of an AC shield. This consists of BGO (bismuth germanate or $Bi_4Ge_3O_{12}$) crystals, which are coupled to MPPC (multi pixel photon counter) arrays, that are used as readout devices.

2. Basic Principles

2.1. Interaction of γ Rays with Matter

When γ rays interact with matter several processes can take place. The three main interaction processes for the energies of interest in this thesis are the photoelectric effect, Compton scattering and pair production. In all cases the photon energy is partially or completely transferred to the electron of an atom and in the case of pair production to the produced positron as well. Fig. 2.1 shows the dominant regions of the processes depending on the γ ray energy $E_\gamma = h\nu$ and the atomic number of the absorbing material Z.

A detailed description of the interaction mechanisms is discussed in the following subsections.

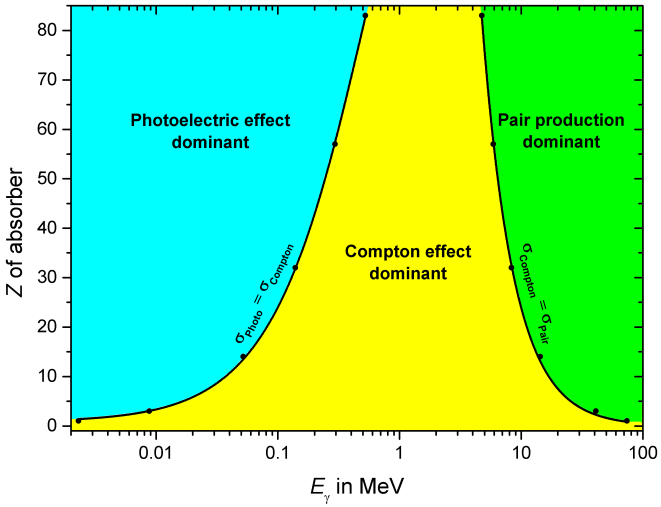

Figure 2.1.: The three main interactions of γ rays with matter and their dominance depending on the photon energy $E_\gamma = h\nu$ and the atomic number Z. Along the lines the two neighboring effects are equal.

2.1.1. Photoelectric Absorption

When a photon interacts with the electron of an atom and transfers its energy completely to the electron the process is called “photoelectric absorption” or “photoelectric effect”. The so called “photoelectron” is removed from its bound state in the atom, mostly from the K shell. The energy of the photoelectron is

$$E_{\mathrm{e}} = E_{\gamma} - E_{\mathrm{b}}, \tag{2.1}$$

with the energy of the photon $E_{\gamma} = h\nu$, where h is the Planck constant and ν the frequency of the photon and E_{b} the binding energy of this electron. The photoelectron in the detector material and its energy is detected. The vacancy of this bound shell is filled by the rearrangement of the electrons from other shells or by catching a free electron from the medium and can cause characteristic X-ray photons, which are absorbed by the detector as well. The photoelectric absorption is the most probable effect for X-rays and γ rays with very low energy and is enhanced by absorber materials with a high atomic number Z. Due to this fact, the preferred detectors and shields for γ radiation have a high Z to increase the probability for this kind of interaction. The cross section is roughly given by [10]

$$\sigma_{\mathrm{PE}} \propto \frac{Z^n}{E_{\gamma}^{3.5}}. \tag{2.2}$$

The exponent n varies between 4 and 5 depending on the energy of the γ ray. A rough scheme of this process is shown in Fig. 2.2.

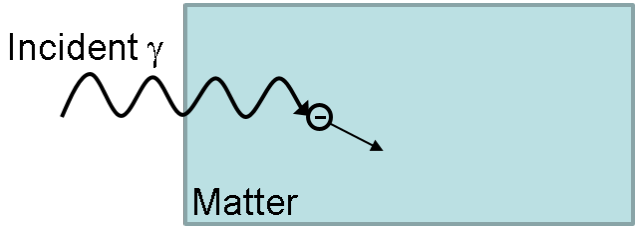

Figure 2.2.: Scheme of the working mechanism of the photoelectric effect.

2.1.2. Compton Scattering

Above γ-ray energies of a few hundred keV the Compton scattering becomes the predominant effect. The incident photon undergoes an interaction with a quasi-free electron (to simplify the calculation) in the absorbing material and is deflected with an angle θ to its original direction. θ can vary between $0°$ and $180°$ which means the energy transfer from the γ ray

to the so called “recoil electron” can reach from zero to a large fraction. The corresponding Compton formula is given by [10]:

$$h\nu' = \frac{h\nu}{1 + \frac{h\nu}{m_0 c^2}(1 - \cos\theta)} \tag{2.3}$$

with h as the Planck constant, ν and ν' as the frequency of the incident and the deflected photon and $m_0 c^2$ as the rest-mass energy of the electron (511 keV).
The cross section for Compton scattering σ_{CS} is proportional to the γ-ray energy E_γ and to the atomic number Z since the probability for this kind of scattering increases linearly with a higher number of electrons in the atom:

$$\sigma_{\mathrm{CS}} \propto \frac{Z \ln(E_\gamma / m_0 c^2)}{E_\gamma / m_0 c^2} \tag{2.4}$$

with $E_\gamma = h\nu = \frac{hc}{\lambda}$ where c is the speed of light and λ the wavelength of the incident photon.
The Klein-Nishina formula [10] describes the differential cross section $\frac{d\sigma}{d\Omega}$ of the Compton scattering of photons on free electrons:

$$\frac{d\sigma}{d\Omega} = Z r_{\mathrm{e}}^2 \left(\frac{1}{1 + \alpha(1 - \cos\theta)} \right)^2 \left(\frac{1 + \cos^2\theta}{2} \right) \left(1 + \frac{\alpha^2 (1 - \cos\theta)^2}{(1 + \cos^2\theta)[1 + \alpha(1 - \cos\theta)]} \right) \tag{2.5}$$

with $\alpha = h\nu / m_{\mathrm{e}} c^2$ and r_{e} as the classical electron radius. Fig. 2.3 shows a simplified sketch of the Compton Scattering mechanism. Photons with low energy are scattered in backward direction and move in forward directions with increasing energies. For this reason standard AC shields as shown in Fig. 1.4 have not only side shields, but a back catcher for the forward direction as well.

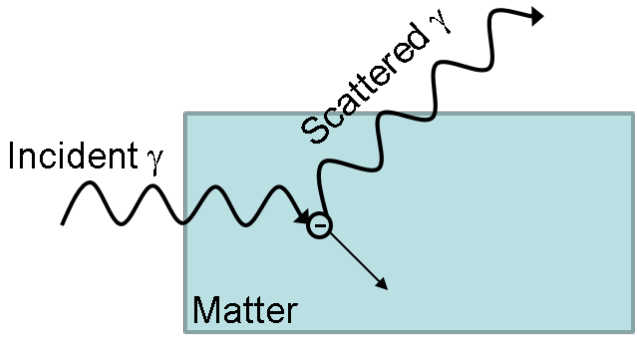

Figure 2.3.: Scheme of the process of Compton scattering.

2.1.3. Pair Production

The process of pair production can occur in the Coulomb field of a nucleus if the energy of the photon exceeds 1022 keV which is the double rest-mass energy of the electron. As a result of this interaction the γ ray disappears and a positron and an electron are generated. The energy above the 1022 keV is shared as kinetic energy among these two particles. After the positron slows down it annihilates with an electron from the medium and two 511 keV γ rays are emitted in opposite directions as secondary radiation. In lead a positron or an electron with a kinetic energy of 5 MeV can reach up to around 3.2 mm [11, 12]. The cross section for pair production σ_{PP} increases with the energy of the γ ray and is proportional to Z^2 of the absorbing material [10, 13]:

$$\sigma_{\mathrm{PP}} \propto Z^2 \ln E_\gamma, \text{ for } \frac{E_\gamma}{m_e c^2} < 137/Z^{1/3}. \tag{2.6}$$

A scheme of the pair production process is shown in Fig. 2.4.

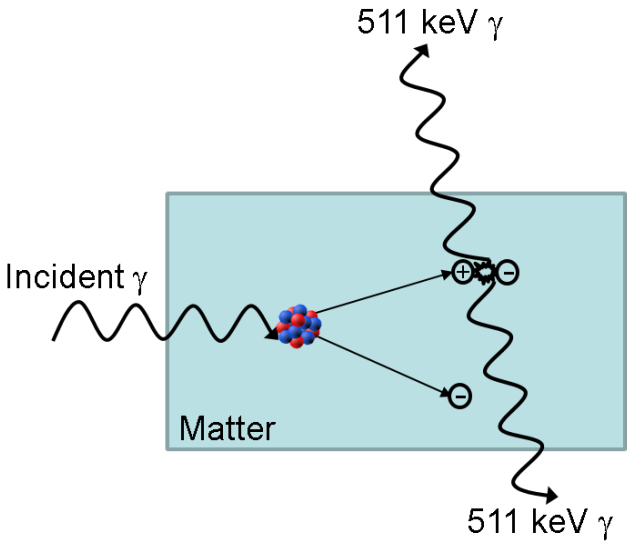

Figure 2.4.: Sketch of the pair production mechanism.

2.2. Detection Efficiency

The efficiency of detectors plays an important role in the detection of particles. Charged particles like alpha or beta radiation have a continuous energy loss and therefore a more or less well defined range. They create an electric pulse that is high enough already after a short distance in the sensitive medium and if the detector is thick enough, 100 % of the energy is detected. Uncharged neutrons or γ rays have one or more isolated interactions and need to travel a longer range for absorption, which makes it almost impossible to reach counting efficiencies of 100 %.

The intrinsic efficiency, ϵ_{int}, is a measure of how well a detector is capable to register an incident particle. It has no dependence on the geometry of the detector and is the ratio of registered events to the events incident on the sensitive medium [10]:

$$\epsilon_{\text{int}} = \frac{\text{registered events}}{\text{events incident on detector}} \tag{2.7}$$

The absolute or total efficiency ϵ_{abs} describes the ratio of the registered events to the

events emitted by the source in all directions [10]

$$\epsilon_{\text{abs}} = \frac{\text{registered events}}{\text{events emitted by source}}. \tag{2.8}$$

The total efficiency depends on the geometry of the detector as well as on the probability for interaction with the detector material.

The correlation between these two efficiencies is $\epsilon_{\text{abs}} = \epsilon_{\text{int}} \cdot \frac{\Omega}{4\pi}$ with Ω as the detector's solid angle (in steradians) looking from the source position. ϵ_{int} depends on the material and thickness of the detector and on the energy of the incident radiation, while the undetected particles just pass the detector without interaction.

The peak-to-total ratio describes the relation of counts in a peak P to the total number of counts T in a spectrum. It shows how well a peak is visible in between the other events from the spectrum and is also called the full-energy-peak or photo-peak efficiency ϵ_{FE}[10, 14]:

$$\epsilon_{\text{FE}} = \frac{P}{T}. \tag{2.9}$$

The relative efficiency ϵ_{rel} helps to compare the absolute full-energy-peak efficiency for the 1332 keV γ of one detector $\epsilon_{\text{abs, det}}$ with that from a 3"×3" sodium iodide (NaI) detector $\epsilon_{\text{abs, NaI}}$, which is used as a standard. The measurement has to be performed with a ^{60}Co point source of known activity in a distance of 25 cm to the detector to find out the count rate of the 1332 keV line in the spectrum. The relative efficiency reads [15]

$$\epsilon_{\text{rel}} = \frac{\epsilon_{\text{abs, det}}}{\epsilon_{\text{abs, NaI}}} = \frac{\epsilon_{\text{abs, det}}}{1.2 \cdot 10^{-3}}. \tag{2.10}$$

2.3. Scintillators

Scintillators are materials which emit light after interacting with γ rays or charged particles. In such a scintillation process the atoms of the material get excited by the incoming radiation and their deexcitation leads to the emission of scintillation light. This technique is one of the oldest known for the detection of ionizing radiation. There are organic and inorganic types of scintillators. This work will focus on the latter one.

2.3.1. Material Requirements

An ideal scintillator is described by the following list of qualifications:

- Possessing a high scintillation efficiency where the kinetic energy of the ionizing radiation is converted into many detectable light photons is a requirement for a good energy resolution.

- Linearity of the conversion from deposited energy to the light yield is provided over a maximum possible energy range.
- Good light collection demands transparency to the own emission wavelength of the medium.
- To achieve a good time resolution fast signal pulses on the basis of a short decay time of induced luminescence are necessary.
- The production of the scintillator should be possible in practical sizes while maintaining a good optical quality.
- To provide a convenient light coupling the scintillator should have an index of refraction close to that of the readout device ($\sim$1.5 for glass).

Since no real material can possess all of these properties at once the choice for a specific scintillator always depends on the demands of the experiment. While inorganic scintillators in general have a better energy resolution and linearity, organic crystals show a faster response time. Because of the high Z and the high density, inorganic scintillators are mainly used for γ spectroscopy. For fast neutron detection and β spectroscopy organic scintillators are in favor.

The luminescence is the emission of photons after the excitation of the electrons of a material and can be divided in two types. The prompt emission of visible light after an excitation is called fluorescence. It occurs within a time scale of around 10^{-8} s. If this emission time takes much longer it is called delayed fluorescence. In the case of phosphorescence the decay time is orders of magnitude slower ($> 10^{-6}$ s) and additionally the wavelength is longer than that from fluorescence. In general, delayed fluorescence and phosphorescence are unwanted effects and should be kept to a minimum for a good scintillator while the conversion to prompt fluorescence has to be as high as possible [10, 14, 16].

2.3.2. Inorganic Scintillators

Inorganic materials are insulators or semiconductors with a certain lattice structure and energy bands. They can be described as outlined below.

The higher band consists of some electrons which have enough energy to move throughout the crystal and is called the “conduction band”. In the lower “valence band” the electrons possess not sufficient energy to travel and are bound to the lattice site. In a pure crystal there exists a forbidden band gap without any electrons in between these two bands. The excitation of an electron from the valence band by irradiation can lift it into the conduction band and leave a “positive” hole in the valence band. Hole and electron can migrate independently through the crystal or form a correlated electron-hole pair, also

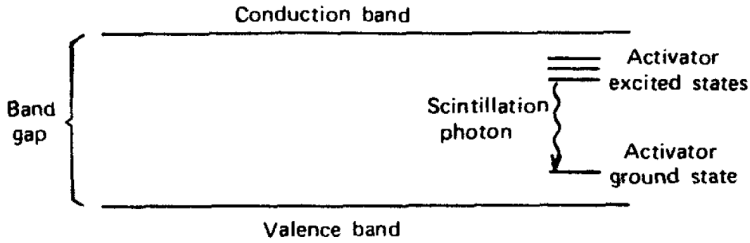

Figure 2.5.: Energy band structure of an activated inorganic scintillator [10].

called “exciton”. When an electron meets such a hole it can fall back in the valence band by the emission of a photon. In a pure scintillator this process would be inefficient since the energy of the photon is high enough to excite another electron from the valence band and also the band gap is too high to emit light in the visible range. For this reason small portions of impurities are added to the crystal. These so-called “activators” form additional energy states in the forbidden gap and the electrons from the conduction band can de-excite to the valence band through these states (see Fig. 2.5). This kind of transition creates photons with lower energy especially in the visible range.
In some cases an electron can occupy an activator excited state from which the transition to the ground state is forbidden. An additional fraction of energy which can be just thermal excitation can lift this electron to a higher configuration whose transition is possible. This competing process needs more time and is called “phosphorescence”.
Some transitions can even take place without the emission of scintillation light and are called “quenching” [10, 14].

2.4. Silicon Photomultiplier

Conventional photodiodes are semiconductors that convert incident light, for instance from a scintillator, into electron-hole (e-h) pairs and produce electrical pulses. Unlike PMTs or **a**valanche **p**hoto**d**iodes (APDs) they have no internal gain. The typical band gap in a semiconductor is around 1-2 eV while the energy of a scintillation photon with approximately 3-4 eV is enough to create an electron-hole pair. The conversion of incident photons into e-h pairs is called quantum efficiency (QE). For a silicon photodiode the maximum QE is around 60-80 %, while for a PMT it is around 20-30 %. A typical silicon sensor consists on its opposite surfaces of an n-type and a p-type layer. These layers are doped with impurities from the fifth main group with five valence electrons or the third main group with three valence electrons, respectively (see Fig. 2.6). The four valence electrons from the silicon

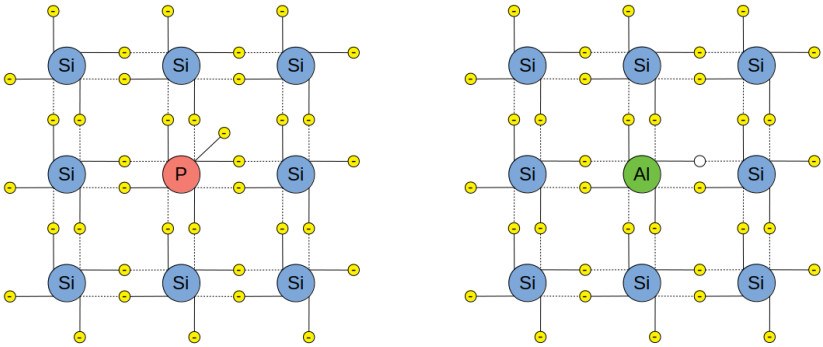

Figure 2.6.: (a) Scheme of silicon n-type doped with phosphorus and (b) p-type doped with aluminum.

make a covalent bond with the ones from the foreign atoms. In the case of five valence electrons one is left over and only slightly bound to the lattice, so it takes just little energy to lift it to the conduction band. The corresponding impurity atom is the donor and the silicon is called n-type doped. In the other case the foreign atom has three valence electrons and one electron is missing for the covalent binding with the silicon. This missing electron forms a hole, the crystal is p-type doped and the impurity atom is called acceptor. The "free" electrons diffuse towards the p-doped region and fill the holes. This process creates a space charge region with a positive space charge in the n-type region and a negative one in the p-type region causing an electric field (see Fig. 2.7). Since there are no free charge carriers in this p-n junction this area is also called depletion or junction layer. The application of a reverse voltage enlarges the p-n interface and consequently the radiation detection zone. Incident photons, e.g. from a scintillator, produce e-h pairs in this region and cause a net current that is proportional to the amount of photons and their energy. In an APD a higher reverse voltage and thus higher velocities of the charge carriers can produce further e-h pairs through collisions and cause a chain reaction. This avalanche process leads to an internal gain and gives the APD its name.
The **si**licon **p**hoto**m**ultiplier (SiPM), also called "**m**ulti-**p**ixel **p**hoton **c**ounter" (MPPC), is a dense array of many small, optically and electrically isolated APDs (microcells). Each microcell has a size in the range of around 10 to 75 µm. It is mechanically robust, insensitive to magnetic fields, has a quite uniform response and works with low voltage, as the electric field is large anyway, because of a smaller size than that for a normal APD, that requires a

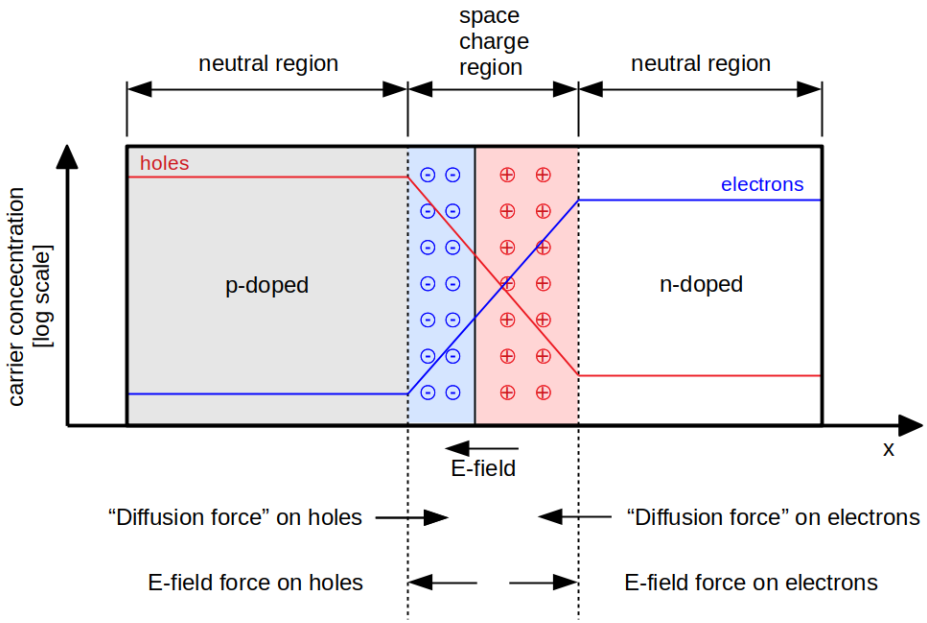

Figure 2.7.: Scheme of a p-n junction in a semiconductor.

higher bias voltage. A high electric field of more than $5 \cdot 10^5$ V/cm, called "Geiger" mode, accelerates an initially produced charge carrier in such a way that secondary charges can be created through "impact ionization" up to a "limitless" amount. Through the consequential breakdown the Silicon becomes conductive. A quenching resistor of typically a few hundred kΩ is used to stop (quench) the current flow. One single microcell can not provide the number of the incident photons since the current flow for one incoming photon is the same as for two or more. This is the reason why arrays of typically 100 to several 10000 photodiodes per mm^2 are used and their output signals are integrated to get the proportional information about the incoming photon flux.
But not each incident photon produces a Geiger pulse in the photodiode. The statistical probability for this process is defined as the photon detection efficiency (PDE) of a SiPM:

$$PDE(\lambda, V) = \eta(\lambda) \cdot \epsilon(V) \cdot F. \tag{2.11}$$

$\eta(\lambda)$ is the quantum efficiency of Silicon which describes the ratio of the created electron-hole pairs to the incident photons. The avalanche initiation probability $\epsilon(V)$ specifies how likely it is for a photoelectron to trigger an avalanche and F is the fill factor that gives the ratio of the active to the total area of the SiPM. With bigger microcells the fraction of gaps for optical and electrical isolation as well as for signal tracks and quench resistors that all result in "dead space" becomes smaller and F increases. Typically the calculation of the PDE can be done via the responsivity of the detector $R = \frac{I_\mathrm{p}}{P_\mathrm{op}}$ with the measured photocurrent I_p and P_op as the incident optical power at a particular wavelength over the sensor area:

$$PDE = \frac{R \cdot h \cdot c}{\lambda \cdot G \cdot e \cdot (1 + P_\mathrm{AP}) \cdot (1 + P_\mathrm{XT})} \cdot 100\% \tag{2.12}$$

h is the Planck constant, c the speed of light, λ the wavelength of the incident light, G the gain and e the elementary charge. P_AP and P_XT are the probabilities for afterpulsing and crosstalk.
The bias voltage V_bias of a SiPM is defined as the sum of the breakdown voltage V_br and the overvoltage ΔV:

$$V_\mathrm{bias} = V_\mathrm{br} + \Delta V \tag{2.13}$$

V_br marks the point of a sudden increase in current and where the electric field is high enough to produce a Geiger pulse. Typically an overvoltage of around 10 to 25% above the breakdown voltage is applied for the operation of the SiPM.
A typical gain G of a SiPM is located around 10^6 and is defined as the ratio of the charge from an activated microcell to the charge of an electron.

$$G = \frac{C \cdot \Delta V}{e}, \tag{2.14}$$

with C as the capacitance of a microcell.
There are mainly three different sources that contribute to the noise of a SiPM. The dark

count rate forms the biggest part of it and is a result of thermally generated electrons that trigger avalanches in the high electric field. It depends on active area, overvoltage and temperature. Another noise component is the optical crosstalk which depends on overvoltage and fill factor. The acceleration of charge carriers during an avalanche emits secondary photons in the near infrared region and these photons can activate further avalanches in the neighboring microcells. The third effect is called “afterpulsing”. In this case the charge carriers can be trapped in defects in the silicon during a breakdown and initiate pulses after a time delay of up to several ns [10, 17].

2.5. Germanium Detector

The **h**igh-**p**urity **ge**rmanium (HPGe) detector is one type of semiconductor detectors which is often used for gamma spectroscopy. Its unprecedented energy resolution of considerably less than 1% makes this detector so unique compared to inorganic scintillators like sodium iodide (NaI) with around 5-10% relative energy resolution (see Fig. 2.8). But this comes not without disadvantages. Some of them are the higher price, the need to keep the detector at liquid nitrogen temperatures during operation, the high supply voltage of several kV and the lower photopeak efficiency (see Fig. 2.8) due to a lower atomic number and smaller sizes available.

The germanium is highly purified to impurity levels of below 10^{10} atoms/cm^3 [10]. However, just like for other semiconductors (e.g. photodiodes) these impurities classify the germanium detector as p type if the impurities are acceptors or n type if they are donors. Applying a high reverse bias voltage on the p-n junction increases the detector’s depletion region where the incoming photons can generate pulses through the production of electron-hole pairs. This depletion region depends on the level of impurities and therefore the large volumes of expensive high purity material increase the price of the detector. With a small band gap of around 0.7 eV the detector has to be operated at temperatures below 130 K since higher temperatures could already cause leakage currents resulting in a worse energy resolution. For this reason normally a dewar with liquid nitrogen is attached to the HPGe detector making it hard to handle due to its weight and, in addition to that, very space extensive. Anyway, up to now there exists no substitute for this kind of detector in high-precision gamma spectroscopy hence it is still widely used [10, 14]. Fig. 2.9 shows the cross section for photoelectric absorption, Compton scattering and pair production in germanium depending on the energy of the photon [18].

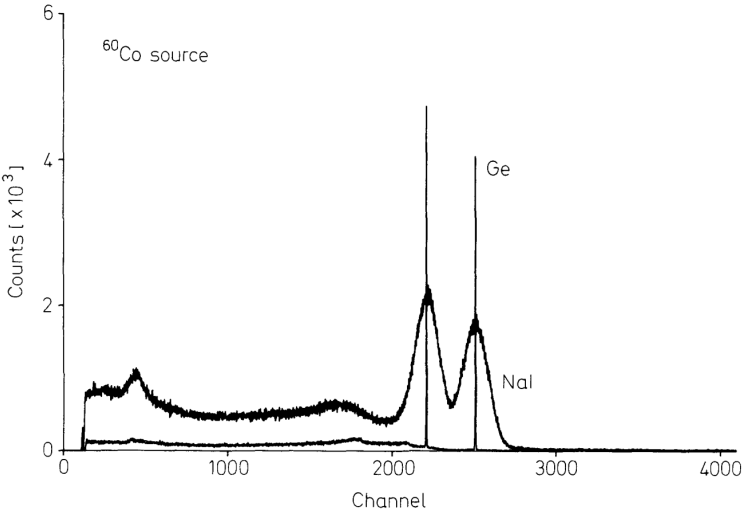

Figure 2.8.: Comparison of ^{60}Co spectra taken with a NaI and a Ge detector [14]. The peaks of the germanium detector are narrower, but contain less counts, than the broad peaks from NaI.

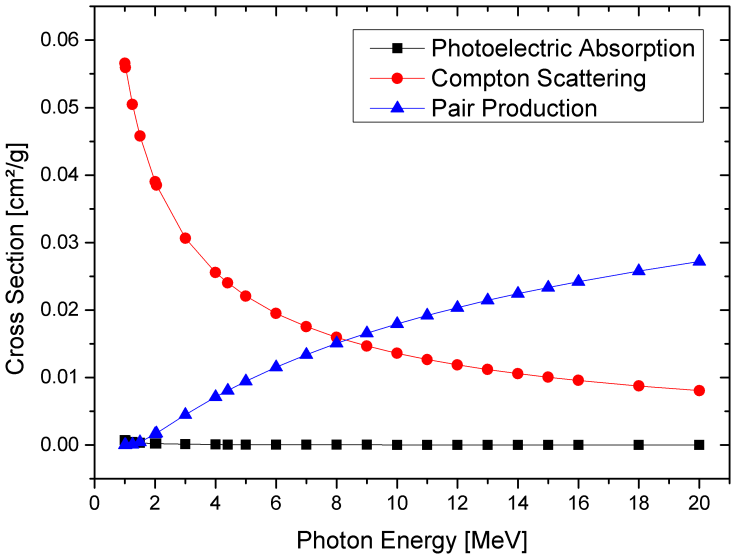

Figure 2.9.: Cross section for photoelectric effect, Compton scattering and pair production in germanium depending on the photon energy [18].

3. Pair Spectrometer

This chapter is going to deal with the ELI-NP pair spectrometer (ELIPS) mentioned in chapter 1. It will describe the details about geometry, design, component parts, electronics and data acquisition.

3.1. Geometry and Design

The whole pair spectrometer consists of 8 aluminum boxes - 4 for the front part and 4 for the back part. The boxes were built together out of multiple aluminum plates (see Appendix B). All of the sides of the boxes have a thickness of 4 mm except of the ones that are facing towards the inner part of the pair spectrometer where the target or the (germanium) detector is located. These plates are 3 mm thick, therefore, more than 93% of the γ rays with an energy of 511 keV can pass through them without interaction according to the Lambert-Beer law (see Eq. 3.1). This law describes the attenuation of the intensity of electromagnetic radiation in matter, and reads,

$$I = I_0 e^{-\mu d}, \tag{3.1}$$

with I_0 as the initial intensity and I as the intensity after passing through the material with the absorption coefficient μ and thickness d. Each aluminum box contains 8 BGO crystals (see Fig. 3.2) which makes 64 crystals in total. The choice on BGO as material was governed by the following reasons. The higher atomic number and density of BGO crystals provide a higher efficiency to absorb γ rays with an energy of 511 keV compared to some common inorganic scintillators as CsI(Tl) or $LaBr_3$(Ce). The density of BGO is 7.13 g/cm³ [19] while it is for CsI(Tl) 4.51 g/cm³ [20] and for $LaBr_3$(Ce) 5.08 g/cm³ [21]. The atomic number for bismuth is $Z_{\mathrm{Bi}} = 83$ (see Chapter 2.1). For cesium it is $Z_{\mathrm{Cs}} = 55$ and for lanthanum $Z_{\mathrm{La}} = 57$. The light yield of BGO is with 8000-10000 photons/MeV much lower than that for CsI(Tl) with 54000 photons/MeV or that for $LaBr_3$(Ce) with 63000 photons/MeV. The relative energy resolution at 662 keV for CsI(Tl) [22] and $LaBr_3$(Ce) [21] is around 5.9 % and 2.8 %, respectively. The BGOs used in this work have energy resolutions from 11-14 % at 511 keV (see Fig. 3.1). The maximum emission wavelength of BGO is at 480 nm which corresponds to 2.6 eV. A γ ray with an energy of 1 MeV could produce $3.8 \cdot 10^5$ photons. This rough calculation shows that the scintillation efficiency and thus the energy resolution for BGO is relatively low. But since the energy that is searched for in the BGOs is known

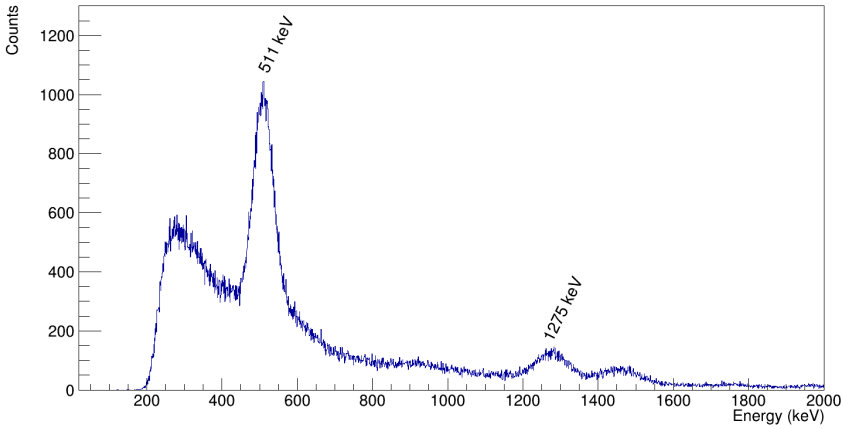

Figure 3.1.: Calibrated BGO spectrum of ^{22}Na.

(511 keV) the energy resolution is not as important as the efficiency to stop high-energy-γ rays. The price of BGO is lower as well, so the choice fell for this material for the pair spectrometer.

The intrinsic efficiency for the photo absorption of a 511 keV γ ray in a back-part BGO with a thickness of 19 mm is $\epsilon_{\text{int, back, 511 keV}} = 0.53$. And in a front-part BGO with a thickness of 8.4 mm it is $\epsilon_{\text{int, front, 511 keV}} = 0.28$. The basis for the design and the dimensions of the crystals was the mechanical compatibility with ELIADE. The shape of the pair spectrometer is for the back part cubelike while the front part looks like a pyramid which is connected to the back part (see Fig. 3.3). Fig. 3.4 shows the whole pair spectrometer with its cabling. The 32 BGOs from the back part cover a solid angle of $\Omega_{\text{back}} = 6.464$ sr [23] looking from a point source in the center between those crystals. This leads to a geometric acceptance of the back part of

$$\epsilon_{\text{geo, back}} = \frac{\Omega_{\text{back}}}{4\pi} = \frac{6.464 \text{ sr}}{4\pi} = 0.514. \tag{3.2}$$

The choice for 8 BGOs in one box was a cost-benefit factor. Actually, the more scintillators are available the better the spatial resolution and the higher the probability for the readout of the scintillation photons. But on the other hand with a higher amount of crystals they become smaller and the efficiency decreases. Additionally, the space and number for electronics and SiPMs is limited as the pair spectrometer has to be mechanically compatible with the ELIADE detector array. Moreover, one FEBEX4 card provides 16 channels which

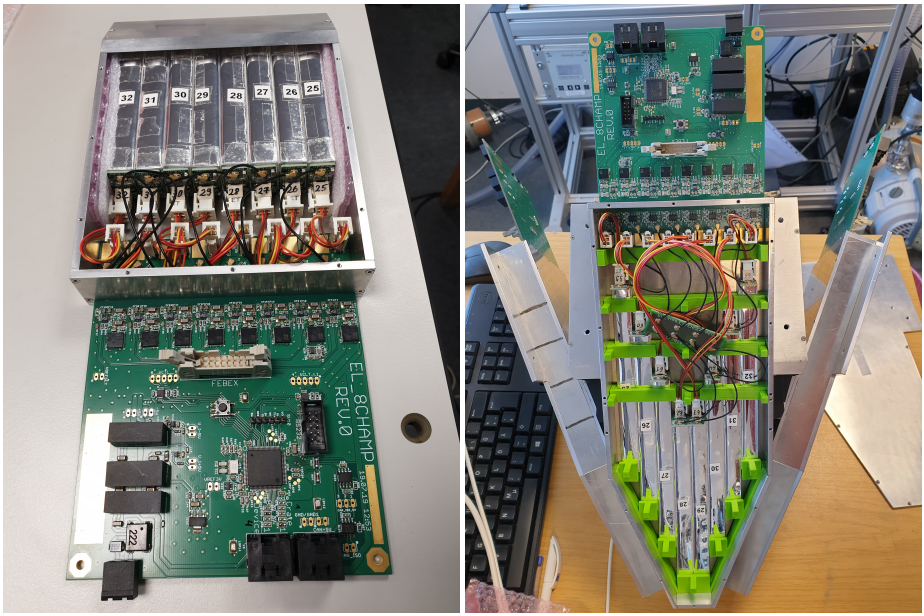

(a) (b)

Figure 3.2.: Pictures of 8 BGO crystals in (a) a box from the back part and (b) a box from the front part of the pair spectrometer.

can be easily shared by two boxes.

The technical drawings for the crystals (see Appendix A) as well as a short instruction manual for the pair spectrometer (see Appendix E) can be found in the appendix.

3.2. Detector Components

3.2.1. Scintillator

ELIPS is composed of a back and a front part. Each part consists of 32 BGO scintillators with different shapes produced by SCIONIX [24]. The crystals of the back part have a size of (113.48×13.5×19) mm³ and are shorter but thicker (see Fig. 3.5(a)) than the front-part crystals which measure (156.43×13.5×8.4) mm³ (see Fig. 3.5(b)). They have different shapes for the reason that the front part of the ELIADE clovers is tapered and so the pair

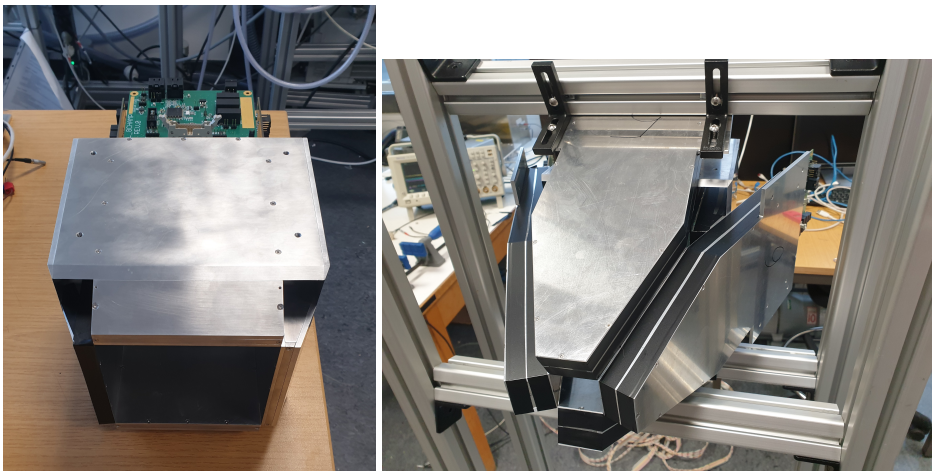

(a) (b)

Figure 3.3.: Picture of the shape of the (a) back part and (b) the front part of the pair spectrometer. The front is coupled to the back part and mounted to a holding structure.

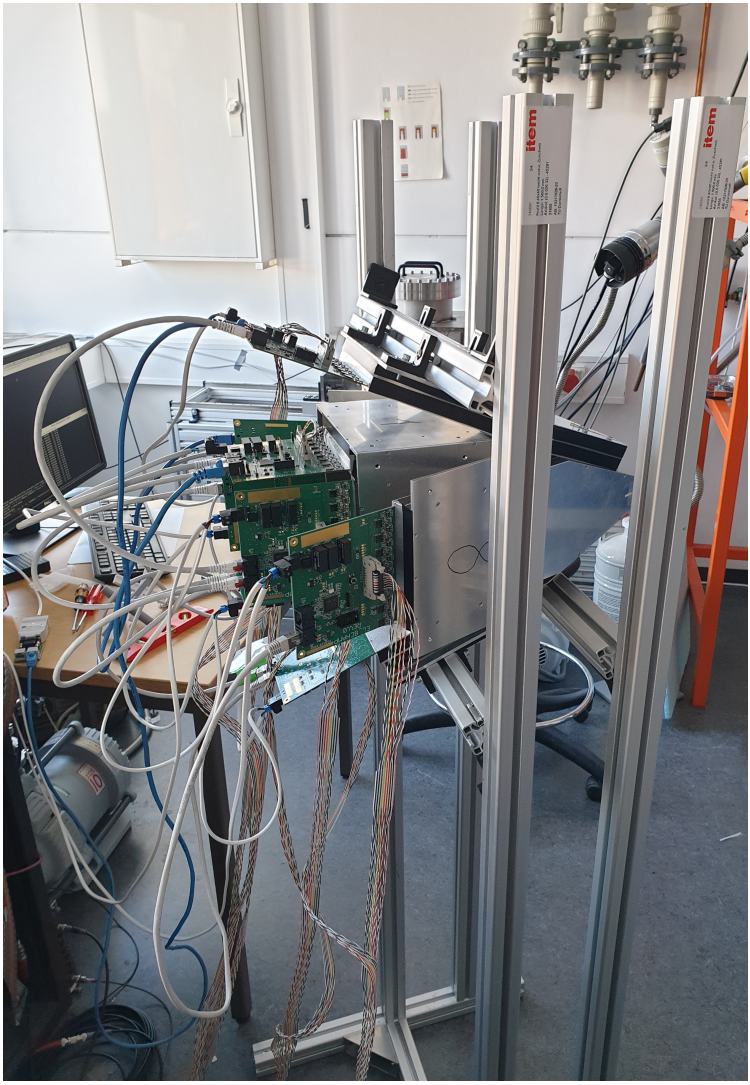

Figure 3.4.: Photo of the completely mounted pair spectrometer with its cabling.

spectrometer's front has to taper as well. This leads to the fact that the front part becomes longer than the back part. For the final pair spectrometer all of the crystals were wrapped into reflective 3M Vikuiti™enhanced specular reflector (ESR) foil [25] since there was already made good experience in other experiments with it [9]. Each crystal has an MPPC array coupled to one edge for the readout of the scintillation photons (see Fig. 3.6). The foil is necessary to reflect the scintillation photons and keep them inside of the crystal until they hit the MPPC. In preparatory measurements, when ELIPS was still in preparation the resolution in ESR foil and in multiple layers of teflon tape showed for a back part BGO around 16 % at 511 keV. Fig. 3.5(a) and (b) show one bare BGO and one covered in teflon, respectively. Contrary to the ESR foil which reflects the scintillation light in a straight way, teflon does it like a diffuser. But as it shows no better results and it is difficult to wrap each crystal with several layers of teflon in the same way and also the thickness of the teflon creates more "dead" space in between the BGOs the ESR foil has been preferred. The ESR film has a thickness of 65 µm and reflects more than 98 % [25] of the visible light spectrum. In order to produce the foils with the exact desired measures, a laser cutting system from the faculty of architecture of the Technical University of Darmstadt was used.

3.2.2. Multi Pixel Photon Counter (MPPC) Array

For the readout of the BGO crystals, arrays of 4×4 MPPCs with the series number S14161-3050HS-04 and temperature compensation have been used. This SiPMs have their maximum PDE of $\approx$ 51 % at a wavelength of around 450 nm (see Fig. 3.8) which is close to the maximum emission wavelength of BGO at 480 nm (see Fig. 3.7 (a)). The emission wavelength of the CsI(Tl) (see Fig. 3.7 (b)) or the $LaBr_3$(Ce) crystals (see Fig. 3.7 (c)) is not well suited for this type of MPPC.

The temperature compensation is important to suppress the gain shift of the SiPMs, as the gain strongly depends on breakdown- and overvoltage, which in turn depends on the temperature, the voltage has to be adapted to keep the shift as small as possible [26].

Each single MPPC has an effective photosensitive area of 3×3 mm² (13×13 mm² for the whole MPPC array) and a pixel size of 50 µm with a geometrical fill factor of 74 %. Each SiPM encompasses 3531 pixels, with 56496 pixels for the whole array, while a γ ray with an energy of 511 keV creates 4088-5110 photons in a BGO crystal. The breakdown voltage is $U_{\text{br}} = 37$ V and the recommended operating voltage $U_{\text{op}} = U_{\text{br}} + 2.7$ V at a temperature of 25°C. The gain is $M = 2.5 \cdot 10^6$ at the recommended $U_{\text{op}} = 39.7$ V [27]. The spectral response range λ reaches from 270 nm to 900 nm and the PDE at 480 nm is around 50 % [27].

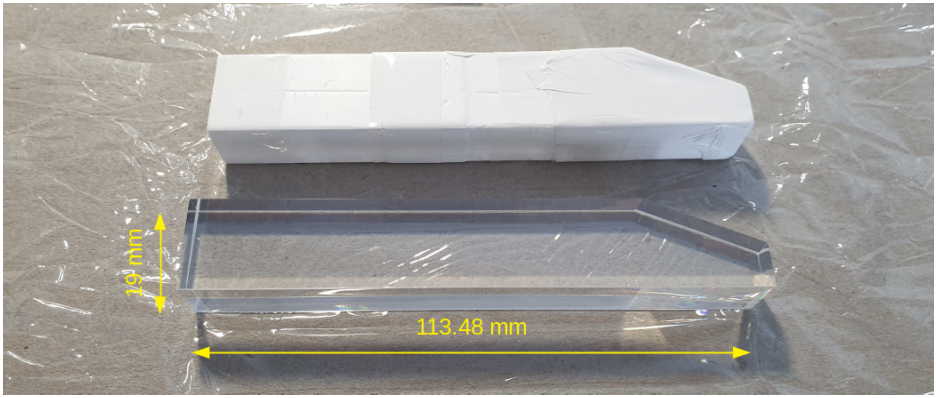

(a)

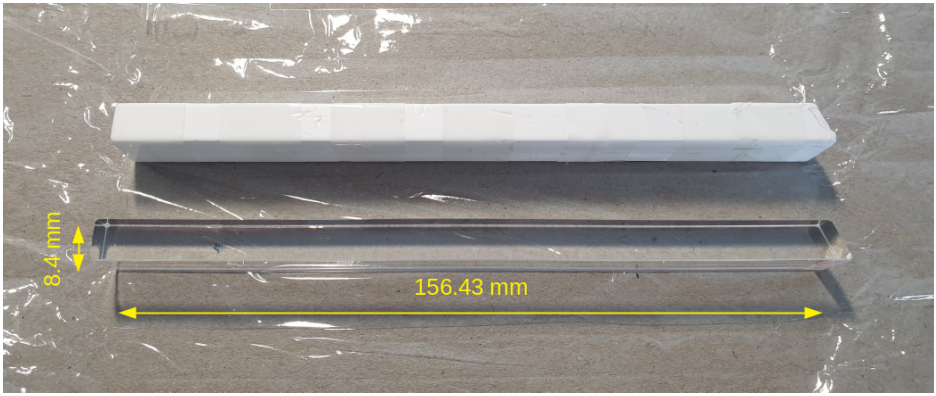

(b)

Figure 3.5.: Pictures of the BGO crystals of (a) the back part and (b) the front part of the pair spectrometer.

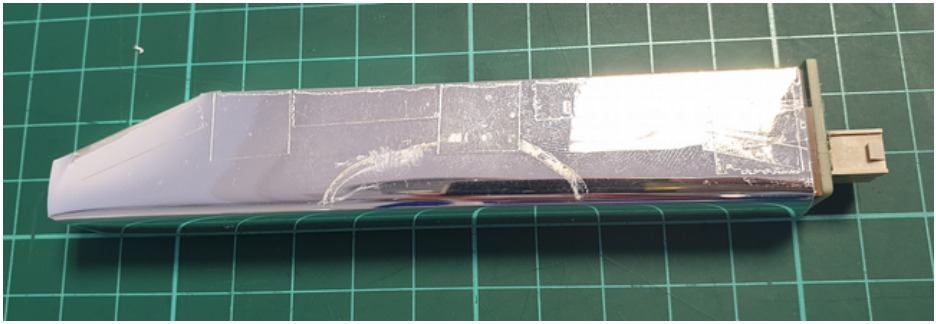

(a)

(b)

Figure 3.6.: Photographs of the (a) back-part and (b) front-part BGOs wrapped into 3M ESR foil with a coupled MPPC array.

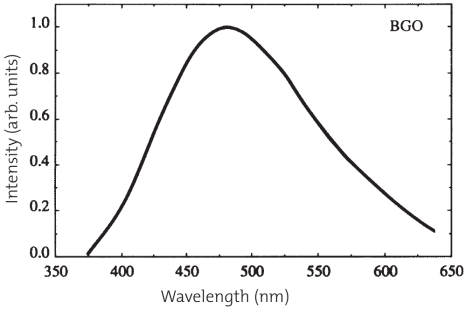

(a)

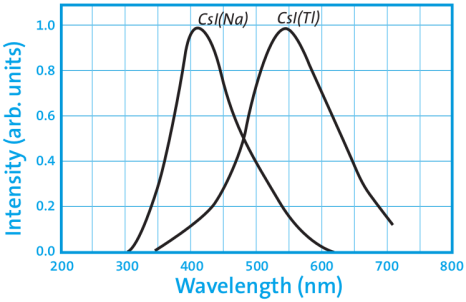

(b)

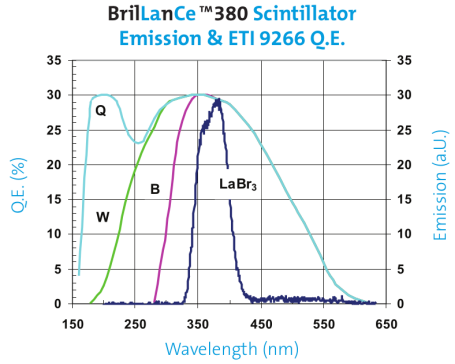

(c)

Figure 3.7.: Emission spectrum of (a) BGO, (b) CsI(Tl) and (c) $LaBr_3(Ce)$. Figure (a) taken from [19]. Figure (b) taken from [20]. Figure (c) taken from [21].

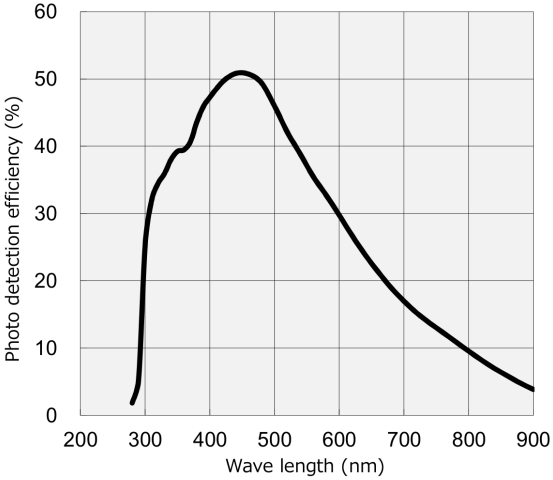

Figure 3.8.: PDE of the used MPPC. Figure taken from [27].

3.2.3. Electronics and Data Acquisition (DAQ)

For the control of the MPPC arrays that are coupled with silicon grease by Saint Gobain to the BGOs, 8 PCBs (printed circuit boards) have been produced by the in-house electronics workshop. The PCBs contain the power supplies with temperature compensation [28] as well as the preamplifier for the MPPCs and produce differential signals that are needed for the FEBEX system. Each PCB is mounted to one aluminum box and regulates the voltage for each individual of the 8 MPPC arrays inside of it. The voltage for each channel can be set with CAN (Controller Area Network) commands via a PCAN-USB adapter by PEAK [29](see Fig. 3.9) which is connected to the USB interface of the PC.

A FEBEX (**F**ront **E**nd **B**oard with optical link **Ex**tension) system has been used for the data acquisition in the measurements. It is developed by the Experiment-Electronics Department of the GSI Helmholtzzentrum für Schwerionenforschung GmbH in Darmstadt, Germany. One FEBEX4a card (see Fig. 3.10) provides a 16 channel sampling ADC with 14 Bit resolution and a sampling rate of 100 MS/s, which is good enough for the needed purposes, as other group members made already satisfying experiences with previous versions of FEBEX. The DC coupled inputs accept differential signals up to 1 V per polarity. The entire control and readout code is implemented on a FPGA (Field Programmable Gate Array) chip [30, 31]. It can be operated in triggerless mode as well as with an external trigger. For the following experiments the triggerless mode has been used since there was enough disk space available and the analysis was performed offline. Storage-intensive or experiments with high rates

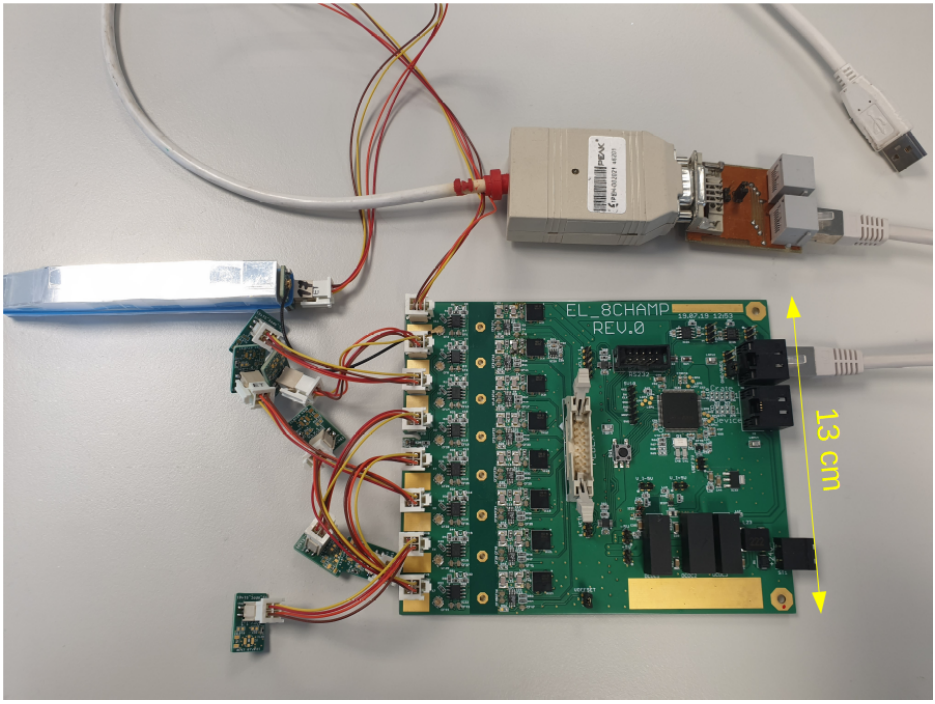

Figure 3.9.: Photograph of one BGO with coupled MPPC array and 7 dummies that are connected to the in-house manufactured PCB. The PCAN-USB adapter communicates via Ethernet with the PCB.

(>10 kHz per FEBEX card) or a HPGe detector inside of ELIPS can use the external trigger. For the use as an intensity monitor the triggerless mode has to be used, as the target in the center is passive. FEBEX applies trapezoidal filters to the sampled pulses and extracts their energy and time information.

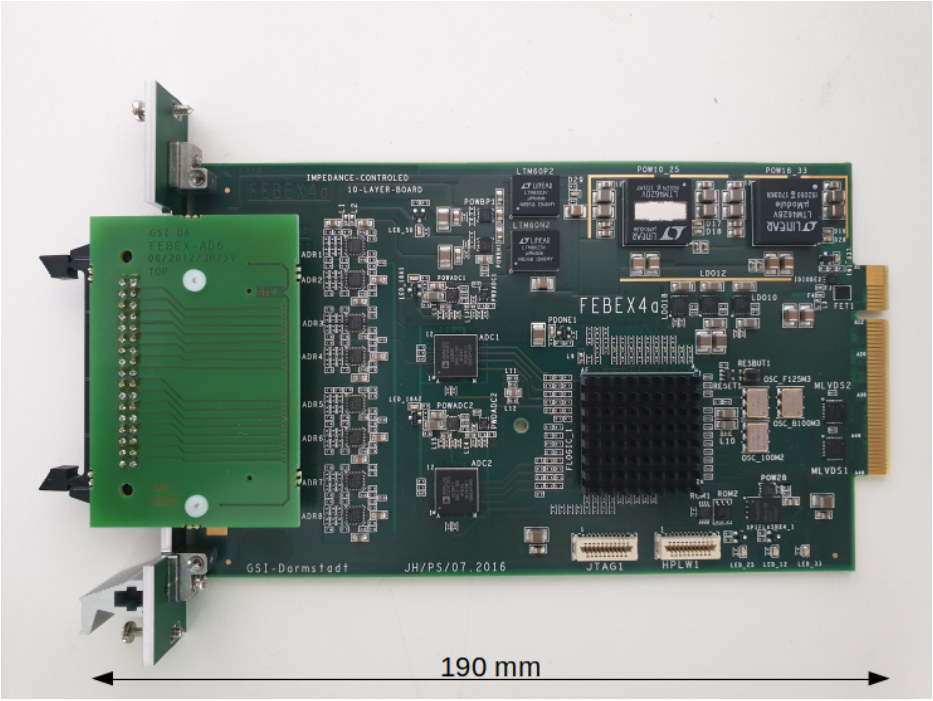

Figure 3.10.: Picture of a FEBEX4a card from the data acquisition system.

4. Experiments

4.1. Proof of Principle with a ^{22}Na Source at the TU Darmstadt

A test with a sodium source was performed in the laboratory to test the pair spectrometer without any other detectors inside. It served also as a comparison with the simulation (see Chapter 5) in connection of the bachelor's thesis of Diandra Richter [32]. The source was placed in the back part of ELIPS centrally in between the back part crystals. For this reason the front part BGOs were not taken into consideration. The data for this measurement was taken for around 185 minutes. The spherical ^{22}Na source had a diameter of 1 mm and an activity of $(A_0 = 309 \pm 9)$ Bq according to the data sheet and an extrapolation to the day of measurement. It was encapsulated in the center of an acrylic glass plate with rectangular shape and dimensions of (23.5×11×2) mm³ [33] (see Fig. 4.1). The alignment of the BGOs around the source is shown in Fig. 4.2. The uncertainty of the position of the source is estimated to be 3 mm in x, y and z direction and the position of the crystals has an uncertainty of 1 mm in each direction [32].

With a probability of 89.90 % ^{22}Na decays through the emission of β^+ and to 10.04 % via electron capture to an excited state of ^{22}Ne [34] (see Fig. 4.3). There is also a small probability of 0.06 % to decay through a β^+ into the ground state. The deexcitation from the excited to the ground state of ^{22}Ne happens via a 1275 keV γ ray. The produced positron from the β^+ decay annihilates with an electron from the surrounding matter while two 511 keV γ rays are emitted with a 180° correlation and can deposit their full energy in two opposite BGO crystals of the pair spectrometer.

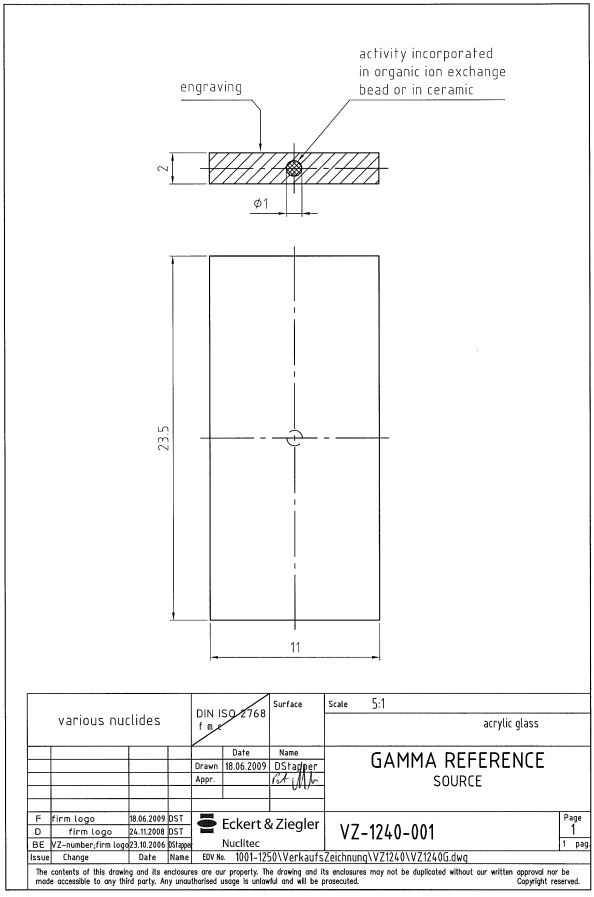

Figure 4.1.: Scheme of the ^{22}Na source with its encapsulation. Figure taken from [33].

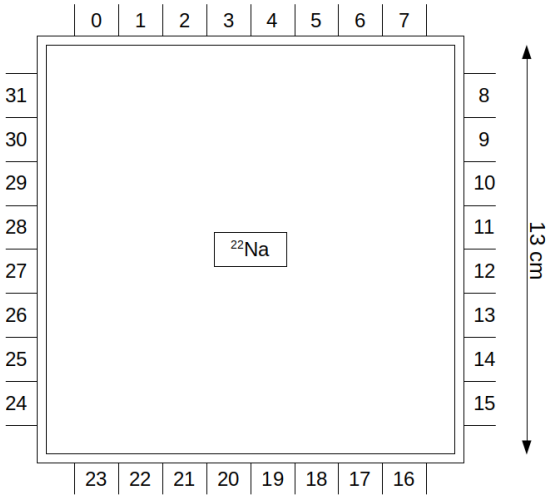

Figure 4.2.: Alignment of the back BGOs around the ^{22}Na source. The source has a true to scale size.

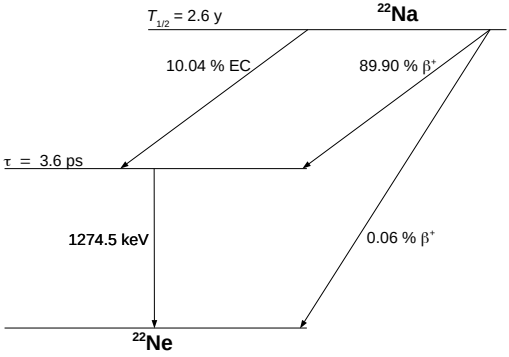

Figure 4.3.: Decay scheme of ^{22}Na.

4.1.1. Data Preparation

The energy calibration for the BGO crystals has been performed with the 511 keV and the 1275 keV γ rays from the same ^{22}Na source that was used for the test itself. Fig. 4.4 shows the calibrated spectrum of one back BGO crystal without background subtraction. The threshold was set to around 200 keV and the source is weak enough that the 1461 keV peak from the ^{40}Ar decay is visible. ^{40}Ar is a daughter nucleus and originates from the electron capture of ^{40}K [35], which is in the concrete walls.

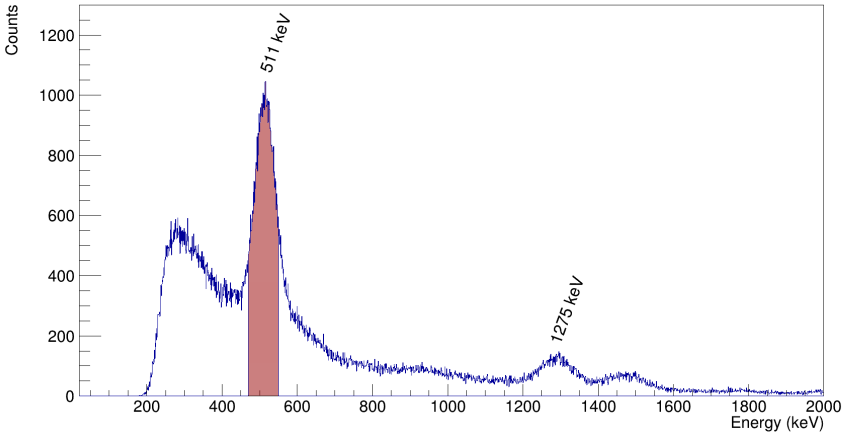

Figure 4.4.: ^{22}Na spectrum of one calibrated back BGO crystal. The red area is used as the coincidence window to mark the 511 keV γ rays in the BGOs.

4.1.2. Results

The total number of all expected decays from the source within the time of 185 minutes is around $(3.4 \pm 0.1) \cdot 10^6$ and for the β^+ decays it is $N_{\beta+} = (3.0 \pm 0.1) \cdot 10^6$. Fig. 4.5 shows the counts of γ rays with an energy of 511 keV detected by each individual BGO crystal under the condition that the back-to-back crystal registered coincidentally another 511 keV. The number in the center gives the total quantity of opposite coincidences and has to be divided by two to get the number of pairs which leads to $N_{\text{pairs}} = 227274 \pm 477$. The range to mark the 511 keV peak in the BGOs was set from 470 to 550 keV which is slightly more than the FWHM that reached up to 73 keV for some BGOs in this measurement. Thus the

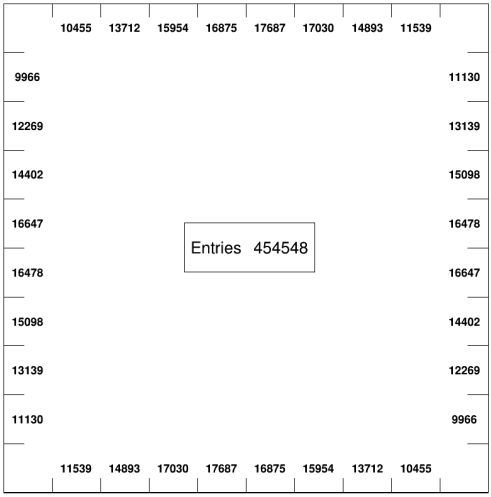

Figure 4.5.: Numbers of the coincident 511 keV γ rays detected by the opposite BGOs from the experiment. The source was placed in the center between the back part crystals. The sum of all numbers (entries) is shown in the center and has to be divided by two to get the number of pairs.

detector efficiency is

$$\epsilon_{\text{det, exp}} = \frac{N_{\text{pairs}}}{N_{\beta+}} = (7.4 \pm 1.1)\ \%. \tag{4.1}$$

For the uncertainty of the position of the source 3 mm in x, y and z direction has been taken and for the position of the crystals it was 1 mm in each direction [32]. Fig. 4.6 shows the BGO IDs from the back part of the pair spectrometer that detected γ rays with an energy of 511 keV in coincidence. An example of a spectrum with a 511 keV coincidence in the back-to-back crystal without background correction is shown in Fig. 4.7.

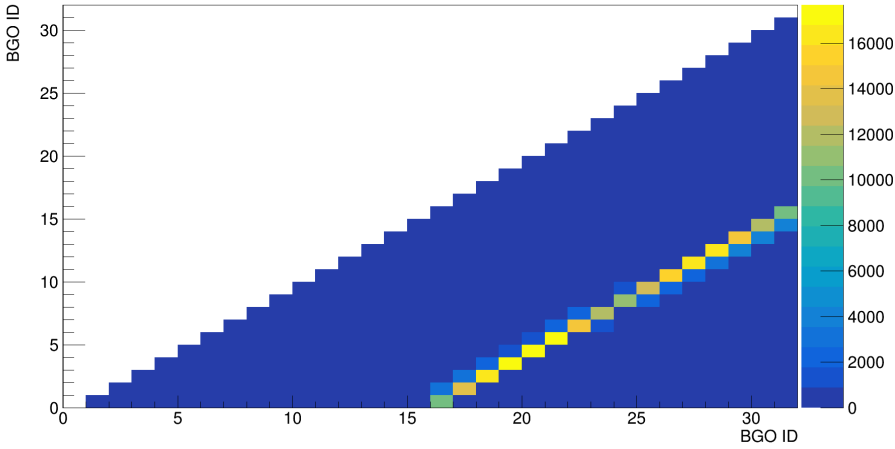

Figure 4.6.: Correlation plot of the back BGOs that detected 511 keV γ rays in coincidence.

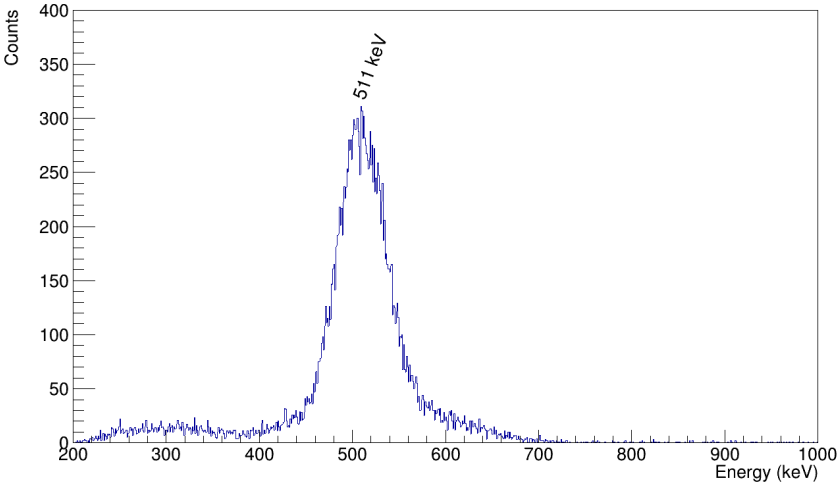

Figure 4.7.: Spectrum of a BGO crystal in coincidence with 511 keV in the corresponding back-to-back BGO without background subtraction.

4.2. Experiment at the University of Cologne

4.2.1. Miniball Detector

For the experiment at the institute of nuclear physics in Cologne a Miniball detector was used in combination with ELIPS. It is a 12-fold segmented HPGe crystal, which has a hexagonal shape at the front and turns into a circular form on the back side. The crystal is mounted inside of an aluminum capsule, which in turn is placed inside of a vacuum sealed cylindrical can (see Fig. 4.9). Some pictures of an identical crystal in an aluminum capsule are shown in Fig. 4.8. The length of one side of the hexagonal front surface is 34 mm [36, 37]. The distance between two opposite sides of the hexagonal surface is 59 mm and between the opposite corners 68 mm. The length of the whole crystal from the front to the back side is 78 mm and the diameter of the rear side is 70 mm. The thickness of the aluminum can is 0.5 mm and the crystal inside is just a little bit smaller than the capsule. The distance from the front face and from the sides of the can to the crystal is approximately 1 mm. From the back side the distance is around 10-15 mm since there are springs which hold the crystal inside the capsule. The segmentation follows six-fold radially through the centers of the hexagonal sides and additionally the crystal is two-fold segmented longitudinally at a distance of 26 mm from the front [38].

The used Miniball detector was cooled with liquid nitrogen during operation and is shown in Fig. 4.9. It is attached with its dewar to a wooden holding structure. The signals from the Miniball detector were coming from the 12 segments and a core. As the charge to voltage conversion of the core signal for the 17.6 MeV γ ray was too high for the DAQ system, which accepts signals up to 1 V, the core has been split with a T-piece into two signals. One of those signals (split core) had half of the original amplitude and the other one (attenuated core) has been attenuated with a sixfold attenuator so it was only $\frac{1}{12}$ of the amplitude. But the latter had a worse energy resolution (0.3 % at 6.1 MeV) and linearity (see Fig. 4.12) therefore it was neglected for the further analysis while only the split core has been used as the core signal.

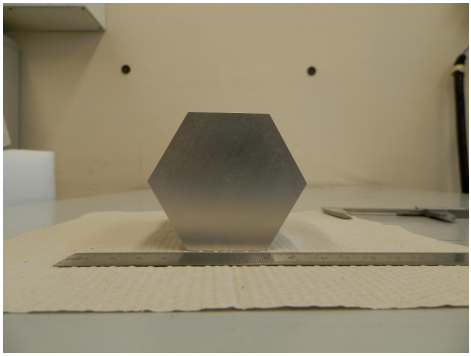

(a)

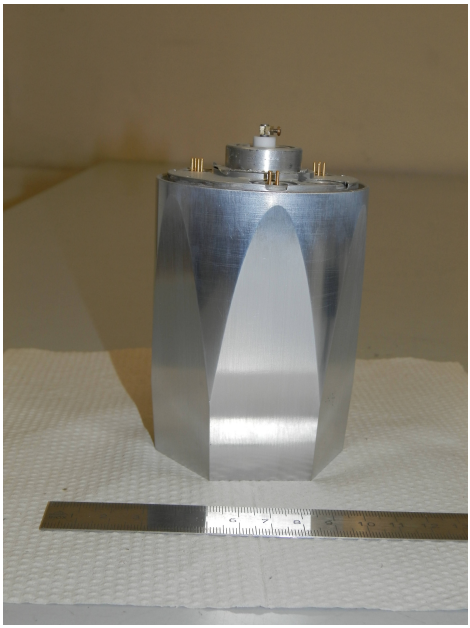

(b)

Figure 4.8.: Pictures of the capsule from a Miniball detector with view (a) from the front and (b) from the side [39].

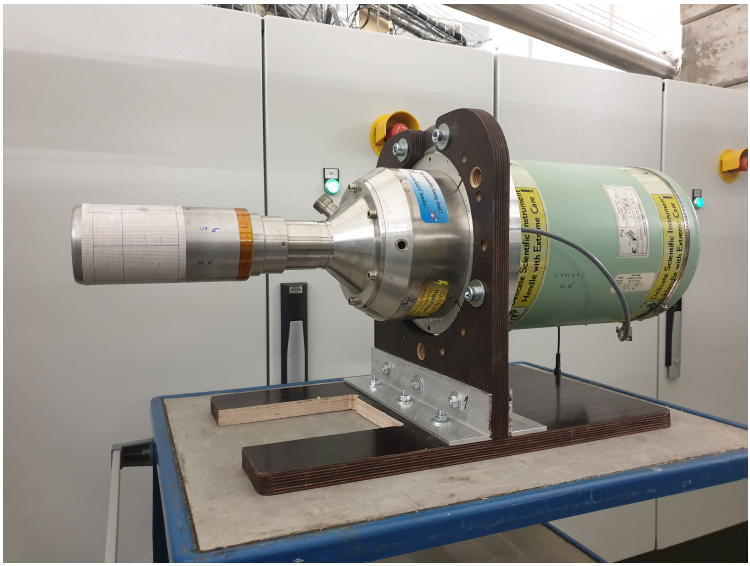

Figure 4.9.: Photograph of the used Miniball detector with dewar and holding structure in Cologne. The graph paper shows the real sizes of the segments.

4.2.2. Measurement with Protons on LiF

For the measurement of pair production in beam, especially in combination with a HPGe detector, γ rays of high energy are required. Some other goals are also to measure the geometric distribution of coincident 511 keV gammas in the BGOs and the efficiency of the reconstruction of double-escape events. For these reasons a proton beam was shot on a LiF target at the tandem accelerator of the University of Cologne.

In the tandem accelerator an ion source produces negative $^{1}\mathrm{H}^{-}$ ions which are accelerated in a high electrostatic field of about 1 MV to a positive high-voltage terminal. At this point the ions pass the terminal and get stripped of their electrons by a stripping carbon foil or gas. As a consequence the ions become protons and experience a second acceleration from the positive potential difference between terminal and ground. This two-stage acceleration leads to protons with a kinetic energy of around 2 MeV [39, 40].

The $^{19}\mathrm{F}(p,\gamma\alpha)^{16}\mathrm{O}$ reaction provides a sharp 6.1 MeV line and the $^{7}\mathrm{Li}(p,\gamma)^{8}\mathrm{Be}$ creates 17.6 MeV γ rays. The proton resonances for these reactions are around 1.34-1.37 MeV [41] and at 441 keV [42] respectively, while the cross sections are at 43(6) mb [43, 44] and at 4.7(5) mb [45]. As the incident protons have an energy of 2 MeV a tantalum degrader with

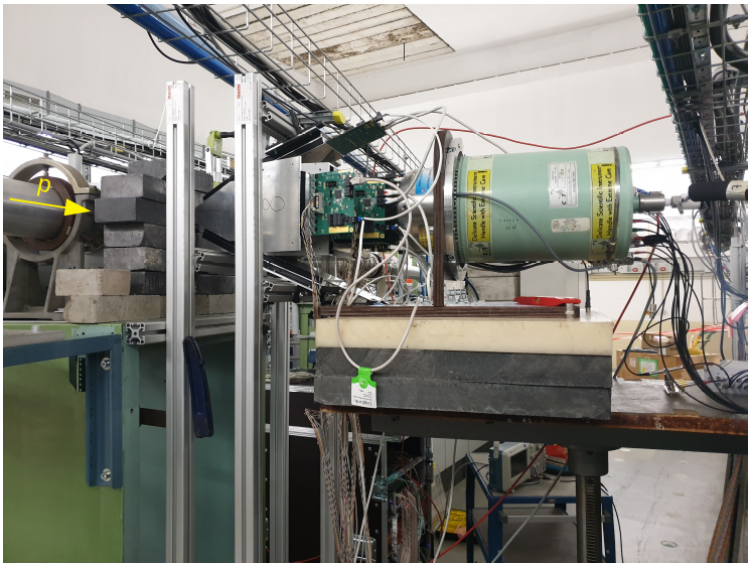

Figure 4.10.: The Miniball detector inside of the pair spectrometer standing next to the beam pipe at the University of Cologne.

4.28 mg/cm^2 thickness was placed in front of the target to decrease the energy to below 1.88 MeV to avoid the ^{7}Li(p, n) reaction which produces neutrons. The latter can result in (n, γ) reactions with the surrounding materials and increase the background [46].

The LiF target was a 2 mm thick optical window with a diameter of 38 mm. It was fixed on a target ladder. The protons lose energy in the thick LiF and pass subsequently the two resonance regions before being stopped completely. The pair spectrometer was standing in a 90° angle to the beam pipe with a 10 cm layer of lead in between to shield the BGOs from direct irradiation from the target (see Fig. 4.10). This collimator had a (4×4) cm^2 hole pointing in the direction of the Miniball detector that was sitting in the back part inside of ELIPS. Fig. 4.11 shows a sketch of the back BGO alignment around the Miniball detector. The distance from the target to the aluminum can of the HPGe detector was around 452 mm. The data with the LiF target has been taken for about 62.5 hours with a count rate of about 7 kHz for the germanium detector. The dead time was around 44 µs. The beam intensity on the target is unknown due to poor focusing through the aperture, as there was only one quadrupole magnet in front of the setup.

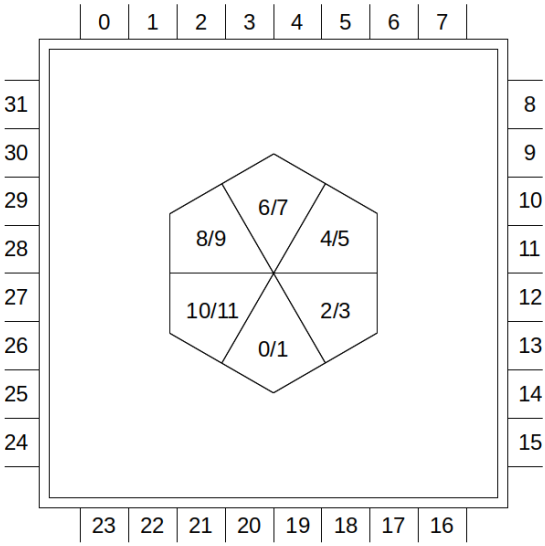

Figure 4.11.: The sketch is showing the alignment of the back BGOs around the Miniball detector looking from the front. The numbers in the center describe the segmentation of Miniball. The first number is showing the front segment and the second stands for the segment which is behind it.

4.2.3. Data Preparation

For the calibration measurement of the Miniball detector and the BGO detectors the sources ^{22}Na and ^{137}Cs were used. The sodium source was very weak and the 511 keV peak only poorly visible next to the 662 keV peak of the stronger cesium source in the BGOs. For this reason the calibration was performed with the 662 keV line from cesium and the 1275 keV line from sodium. Even with the γ lines at low energies the calibration fits well for the high energy region of the (split) core around 6.1 MeV and 17.6 MeV in the LiF measurement. This shows a good linearity of the germanium detector and its electronics. The relative energy resolution of the core for the 6129 keV line is 0.13 % FWHM. The core signal, that was additionally attenuated with a sixfold attenuator, shows a worse performance in connection with resolution (0.3 % at 6129 keV) and linearity (see Fig. 4.12) and was not further considered for these reasons.

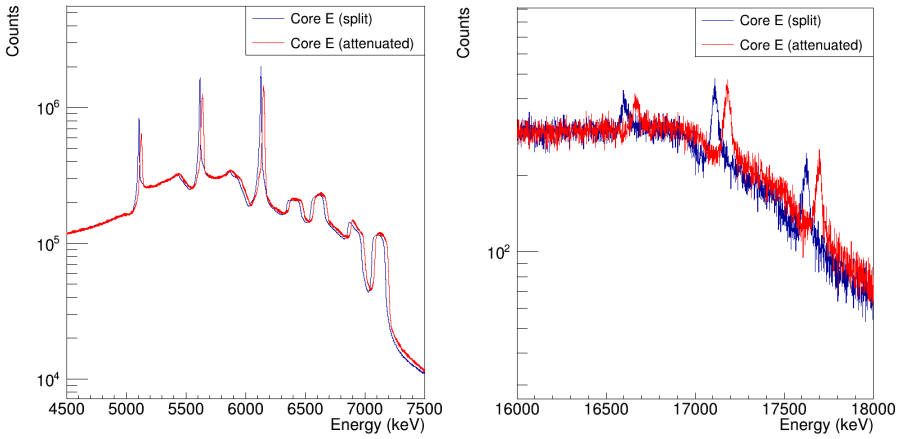

Figure 4.12.: Comparison of the split core signal with the attenuated one for energies around (a) 6 MeV and (b) 17 MeV. The energy resolution and linearity are visibly worse for the attenuated spectrum.

Fig. 4.13 and 4.14 show the residua of the 511 keV peak for the back and front BGO crystals. The calibration for the crystals of the back part fits well since the deviation is within 1 % ($\approx$5 keV). The deviation for the front part goes up to more than 6 % ($\approx$30 keV).

The uncertainties are around 0.08 % for the back and about 0.6 % for the front part. One possible interpretation for the high divergence in the front BGOs could be the light output non-uniformity (LONU) where the light yield of the crystal depends on the position of the γ hit in the crystal and is not the same throughout the BGO [47].

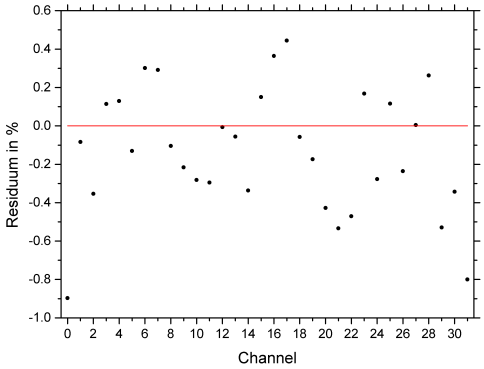

Figure 4.13.: Plot of the residua of the 511 keV peak in percent for the back BGO crystals.

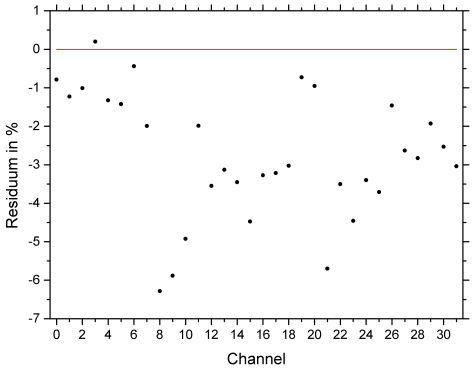

Figure 4.14.: Plot of the residua of the 511 keV peak in percent for the front BGO crystals.

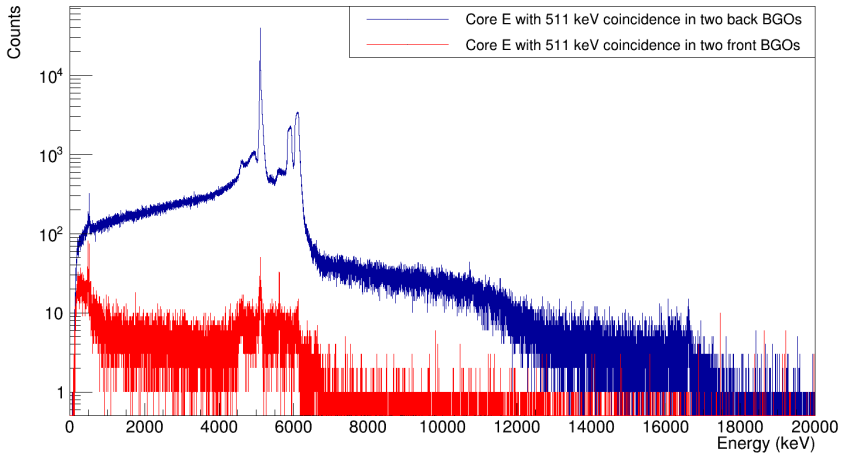

Figure 4.15.: Comparison of the Miniball core energy in coincidence with two 511 keV γ rays in two back BGO crystals (blue) and with two 511 keV γ rays in two front BGOs (red).

As the Miniball detector was placed in the back part of the pair spectrometer the coincidence spectrum of the germanium core with two 511 keV γ rays in the BGOs from the back part (blue) looks different and shows orders of magnitude more statistics than with two 511 keV γ rays in the BGOs from the front part (red), which is visible in Fig. 4.15. Due to this fact the front part BGOs were neglected for the data analysis and results.

The range for the 511 keV peak in the BGOs reaches from 470 to 550 keV. The most coincident events with an energy of 511 keV in the BGOs occur within a time difference of 100 ns to the germanium signals (see Fig. 4.16), that is why this value was set for the coincidence window. The tail in the low-energy region is produced by the Miniball electronics. Low-energy-γ rays interact mainly at the front edge of the detector and have slower time signals than high-energy-γ rays which is the reason for this “walk effect” on the left side [48, 49]. Anyway, this effect does not affect the measurement since the time window is large enough and the focus is on the high-energy part.

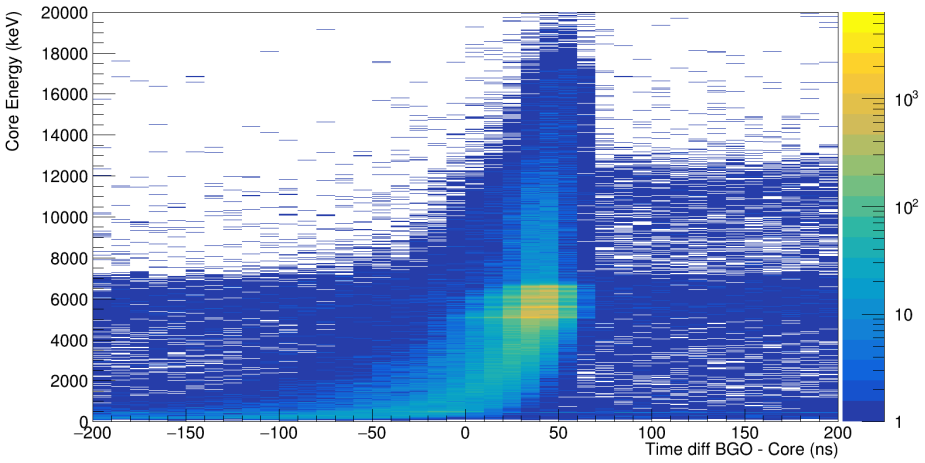

Figure 4.16.: Plot of the γ-ray energy in the germanium core in dependence of the time difference between the core signal of the Miniball detector and a 511 keV γ ray in BGO 3 from the back part of the pair spectrometer.

4.2.4. Results

Fig. 4.17 shows the important parts of the energy spectrum of the (split) core signal from the Miniball detector. In Fig. 4.17 (a) a strong 478 keV line comes from a $^{7}\mathrm{Li}(p,p')^{7}\mathrm{Li}$ reaction [46] and the 511 keV line comes from the pair annihilation in the lead collimator. The expected 6.1 MeV full energy (FE) peak with the corresponding single-escape (SE) and double-escape (DE) peak are clearly visible in Fig. 4.17 (b). Additionally, peaks from the $^{19}\mathrm{F}(p,\gamma\alpha)^{16}\mathrm{O}$ reaction exist at 6.9 MeV and 7.1 MeV as well as their SE and DE peaks. Due to the short lifetimes of below 10 fs the emission of these γ rays from the excited $^{16}\mathrm{O}$ nucleus happens in-flight. For this reason these peaks are Doppler broadened [41]. The three small peaks around 12 MeV in Fig. 4.17 (c) are the results of the sum up of a FE, SE or DE event corresponding to an energy of 6.1 MeV together with another FE, SE or DE event of a γ ray with an energy of 6.1 MeV. Since the intensity for SE and DE events is lower compared to the FE, the probability for the combinations of one DE and one SE event or for two DE events are lower, which is the reason why there are only three peaks visible in this region. Fig. 4.17 (d) shows the highest energy of the spectrum at 17.6 MeV with the SE and DE peaks.

Fig. 4.18 (a) and (b) show additionally to the energy of the core (blue spectrum) a red

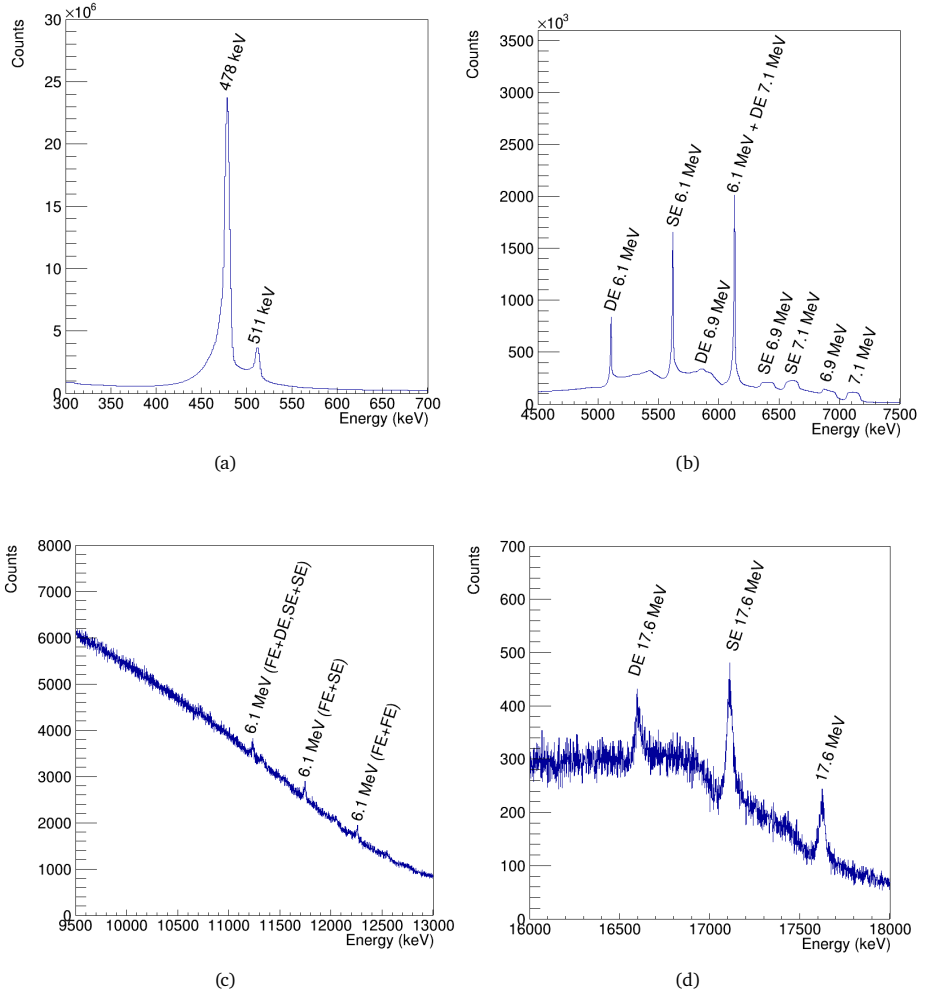

Figure 4.17.: Spectrum of the Miniball core in the region of (a) 300-700 keV, (b) 4500-7500 keV, (c) 9500-13000 keV and (d) 16000-18000 keV.

spectrum which is the core energy in coincidence with two 511 keV γ rays in two BGOs in the back part of the pair spectrometer. The red spectrum shows way less statistics, only around 0.2 % of the blue spectrum, but it is also much "cleaner" since a lot of Compton background as well as FE and SE peaks are removed. There is also a broad DE peak corresponding to the 7.1 MeV line sitting under the 6.1 MeV peak. With the help of ELIPS this DE peak could be made visible. The DE peak from the 6.1 MeV γ ray makes around 36(5) % of its FE peak in the blue spectrum and in the case of the 17.6 MeV FE peak the volume of the DE peak is around 83(2) %.

The DE peaks corresponding to the 6.1 MeV line have a slope on their left and on their right side. The left edge comes most likely from neutron damages in the germanium detector [50] and is also visible in the calibration data. The right one is caused by escape events that deposit a small part of their energy in the germanium before leaving it and in the blue spectrum additionally from the Compton continuum. Due to the more complicated shape of the peaks the comparison of the volume of the 6.1 MeV DE peak from the red coincidence spectrum with the one from the core singles spectrum has been made in a twofold manner - once by taking the integral of only the Gaussian part of the peaks without the slopes and once additionally with the flanks. These limits were used to determine the maximum uncertainty. In the red coincidence spectrum the DE peak from 6.1 MeV has around 5.2(11) % of the DE peak from the core single events. The origin of the high uncertainty lies in the above mentioned evaluation procedure.

In the case of the DE peak from 17.6 MeV the ratio of this peak from the coincidence spectrum to that from the core makes approximately 7.1(5) %.

The 2-dimensional histogram in Fig. 4.19 shows the Miniball core energy on the x axis and the sum energy of two BGO crystals from the back part on the y axis. The yellow spot at around 5.1 MeV core energy and about 1022 keV BGO sum energy marks the double-escape events from the Miniball detector that were registered by two BGO crystals. The light blue diagonal line that runs to the right bottom of the histogram represents the double-escape events that left part of their energy in the germanium detector before being absorbed by the BGOs. The coincidence matrix of the Miniball core energy against the energy of one BGO crystal is shown in Fig. 4.20.

An example of how the spectrum of one back part BGO looks like is shown in Fig. 4.21, while Fig. 4.22 shows the germanium single spectrum of one segment from the Miniball detector. It is visible that in the single segment the ratio of full-energy peak to double-escape peak is much smaller than in the core. The reason is the lower probability for a segment to absorb both 511 keV γ rays while for the core the signals from all segments are added up and increase this ratio. The correlation plots in Fig. 4.23 and Fig. 4.24 indicate the BGOs that registered 511 keV in coincidence with a gate on the double-escape line at 5.1 MeV for the core and segment 2 respectively. For segment 2 some BGO pairs like 7 and 19 show more coincidences than pairs like 12 and 27 which are more "shielded" by other segments (see Fig. 4.11).

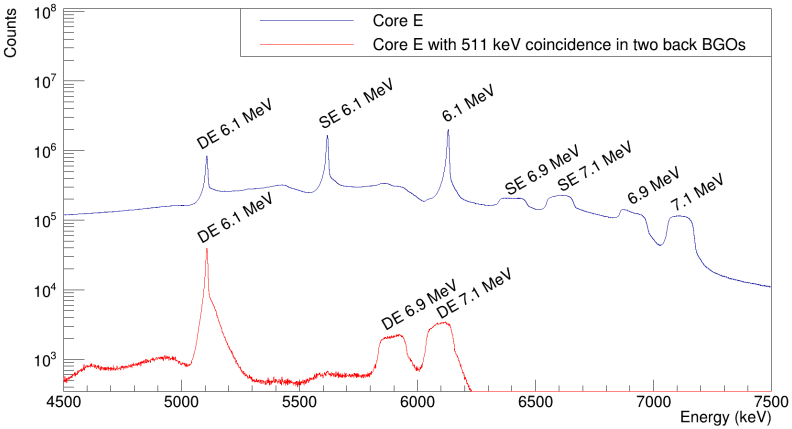

(a)

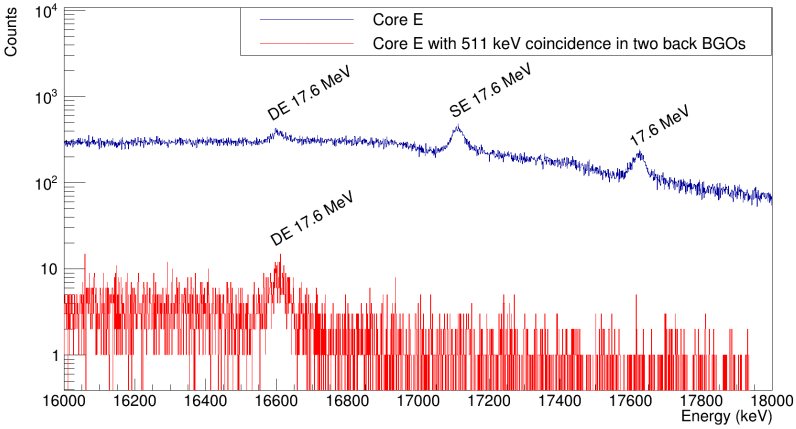

(b)

Figure 4.18.: Blue: γ-ray energy spectrum of the core signal from the Miniball detector. Red: Energy spectrum of the core in coincidence with two 511 keV γ rays in two BGOs from the back part of the pair spectrometer. (a) shows the spectra for the region from 4.5 to 7.5 MeV and (b) from 16 to 18 MeV.

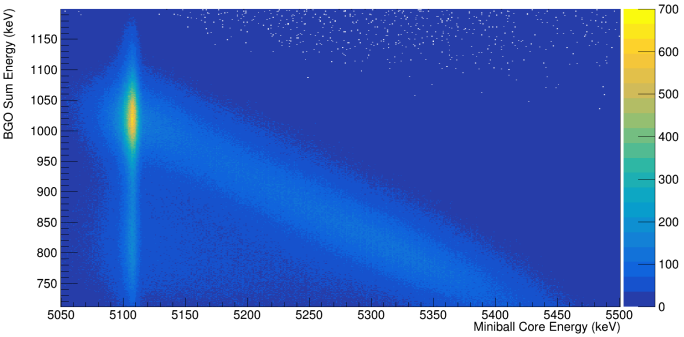

Figure 4.19.: The x axis shows the Miniball core energy and the y axis the sum energy of two back BGOs. The diagonal line starting at the core energy of around 5.1 MeV and the BGO sum energy of 1022 keV goes to the right bottom and marks the events that were partly absorbed by the germanium and deposited the rest of their energy in the BGOs.

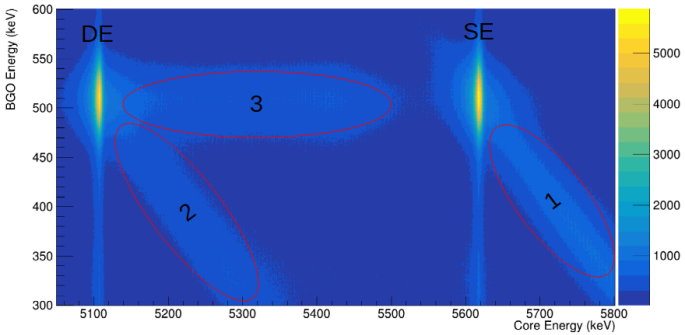

Figure 4.20.: The x axis shows the Miniball core energy and the y axis the energy of one back BGO. The yellow spots mark the single-escape and double-escape peaks in the germanium in coincidence with one detected 511 keV γ ray in the BGO. The diagonal line marked with numbers 1 and 2 show the events that were partly absorbed by the germanium and deposited the rest of their energy in the BGOs. In area number 3 the BGO detected one γ ray with an energy of 511 keV while the second one was Compton scattered in germanium.

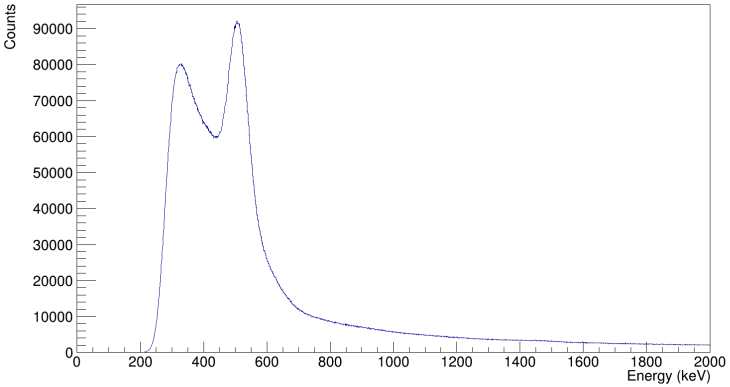

Figure 4.21.: Spectrum of one BGO crystal from the back part of the pair spectrometer.

The single spectra as well as the correlation plots for the other segments are attached in the Appendix C.

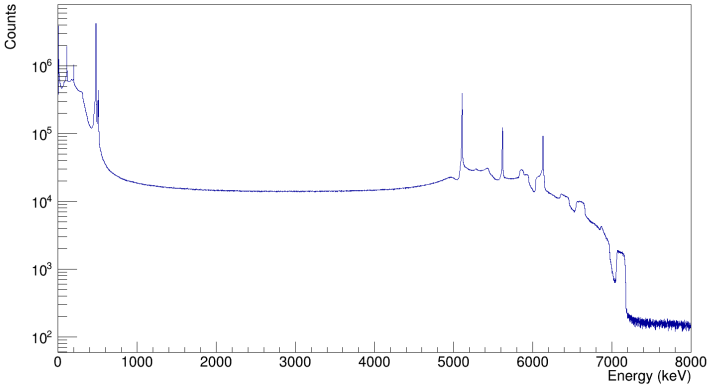

Figure 4.22.: Spectrum of one segment from the Miniball detector taken during the LiF(p,γ) reaction.

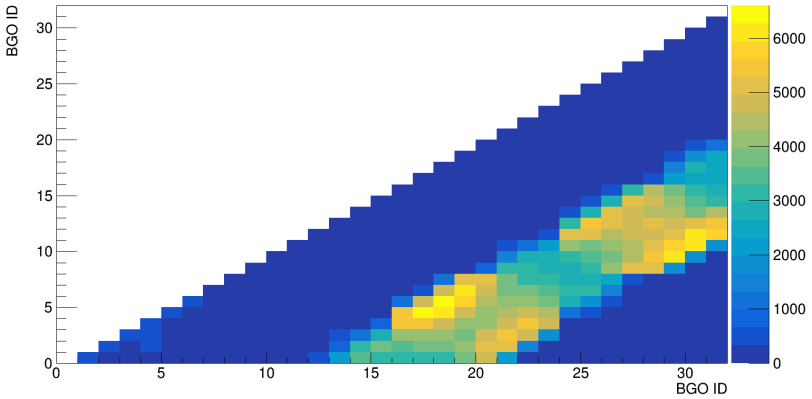

Figure 4.23.: Correlation plot of the BGOs that detected 511 keV γ rays in coincidence with the double-escape peak at 5.1 MeV from the Miniball core.

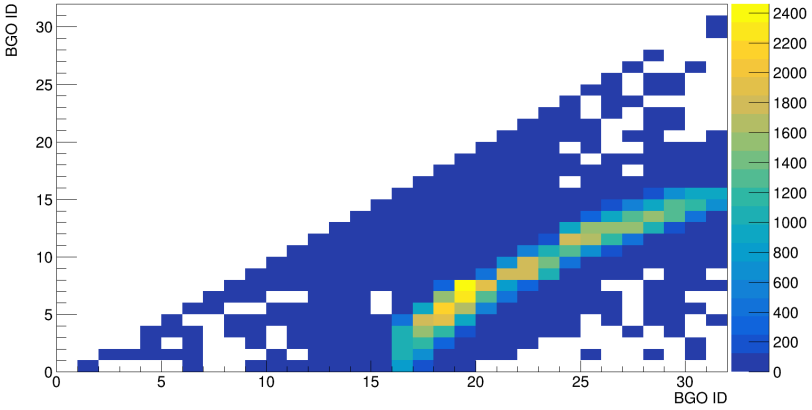

Figure 4.24.: Correlation plot of the BGOs that detected 511 keV γ rays in coincidence with the double-escape peak at 5.1 MeV from the Miniball segment number 2.

4.3. Experiment at the ILL

4.3.1. IFIN-HH Clover Detector

At the **I**nstitut **L**aue-**L**angevin (ILL) in Grenoble, France, a clover detector was placed in the center of ELIPS. The detectors from the IFIN-HH (Institute of Physics and Nuclear Engineering) in Magurele, Romania, and consists of 4 HPGe crystals without segmentation. Each crystal from this clover has a close to cylindrical shape with a length of 70 mm and a diameter of about 46 mm. Approximately 36 mm of the front of each crystal are tapered with an angle of 7° (see Fig. 1.2 (b)). The clover is accommodated in an aluminum can and is cooled with liquid nitrogen during the time of operation. Fig. 4.25 shows the detector with the dewar on a support structure.

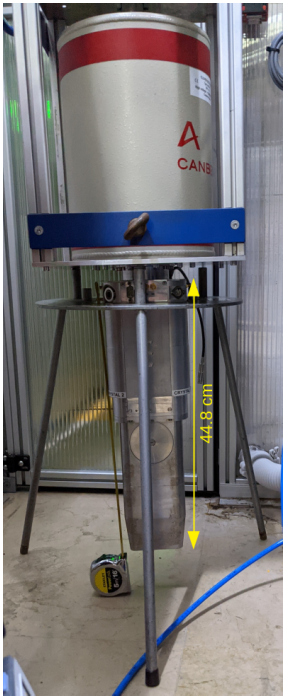

Figure 4.25.: Picture of the used clover detector with dewar on a holding structure at the ILL.

4.3.2. Measurement with Neutrons on NaCl

For this experiment, neutrons with a high energy around a few MeV were produced in the reactor by fission. These neutrons were slowed down with water to thermal energies in the meV region and guided to the setup through neutron guide H22, where they hit a NaCl target with a weight of 5g. The target was attached inside of the beam pipe where the neutron flux was in the order of $\phi \approx 5 \cdot 10^7 \frac{\text{neutrons}}{\text{s} \cdot \text{cm}^2}$ [51]. The setup looks similar to the one from Cologne, see Fig. 4.26. Between the pair spectrometer and the beam pipe a lead collimator shielded the BGOs from the direct beam stemming from the target. The clover detector was placed mainly in the front part inside of ELIPS with an angle of 90° to the beam pipe. The data acquisition with the NaCl target was running for 65 hours. NaCl consists of stable ^{23}Na as well as from the stable isotopes ^{35}Cl and ^{37}Cl with abundances of 75.8 % and 24.2 % respectively. 19 of the 23 most intense γ transitions of the $^{35}\text{Cl}(n,\gamma)^{36}\text{Cl}$ reaction with a capture cross section of $\sigma = 43$ b are in the energy region between 1.1 and 8.6 MeV [52] in which pair production is possible. The cross sections for the thermal neutron capture reaction of ^{23}Na and of ^{37}Cl are with 0.54 mb [53] and with 0.43 mb [54] around a factor 100 smaller and can be neglected. Table 4.1 shows the relative Intensities for some of the strongest lines from the $^{35}\text{Cl}(n,\gamma)^{36}\text{Cl}$ reaction [55].

Table 4.1.: Relative intensities for some strongest lines from the $^{35}\text{Cl}(n,\gamma)^{36}\text{Cl}$ reaction [55].

E (keV)	I (%)
6111	100.0(9)
7414	49.9(8)
7790	40.4(5)
5715	27.59(24)
4979	18.69(15)
3062	17.10(11)
8579	13.40(20)

The crystal alignment looking at the front of the detectors is illustrated in the sketch of Fig. 4.27. The outer numbers mark the positions of the front BGO crystals while the numbers 0, 1, 2 and 3 in the central part stand for the four clover crystals.

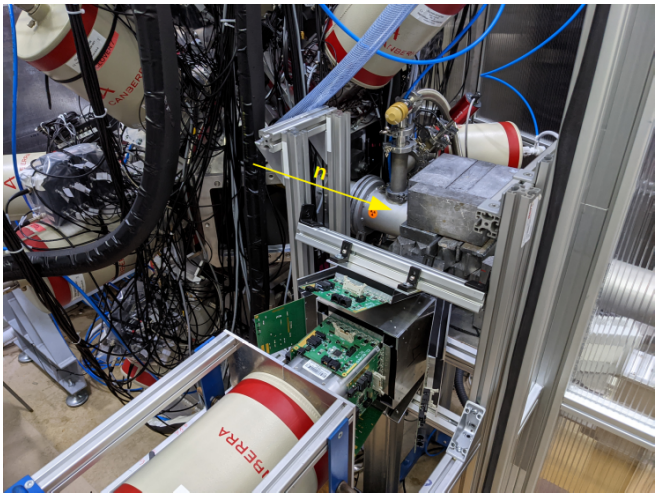

Figure 4.26.: The clover detector inside of ELIPS with a lead collimator standing next to the beam pipe at the ILL.

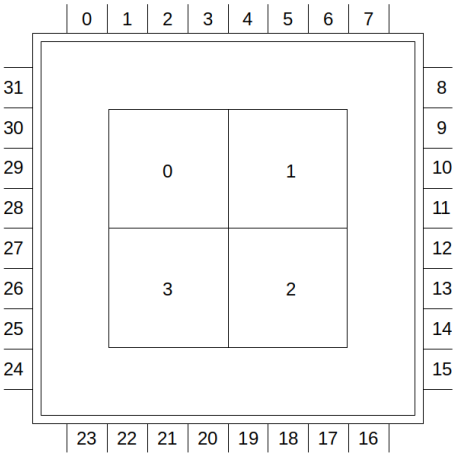

Figure 4.27.: The crystal alignment of front BGOs and clover detector from the front view. The four numbers in the center indicate the 4 clover crystals. The outer numbers show the positions of the front BGO crystals.

4.3.3. Data Preparation

The calibration for the IFIN-HH clover detector was performed with a ^{152}Eu source. The calibration point with the highest energy was around 1.4 MeV. Nevertheless, all of the clover crystals show a good calibration and linearity even for the high energy region of about 6.1 MeV in the NaCl measurement as shown in the residual plot in Fig. 4.28. The relative energy resolution for each of the 4 clover crystals at an energy of 6.1 MeV is between 0.11 % and 0.14 % FWHM. The singles spectrum from all of the clover crystals is shown in Fig. 4.29 and the corresponding partial level scheme of ^{36}Cl in Fig. 4.30.

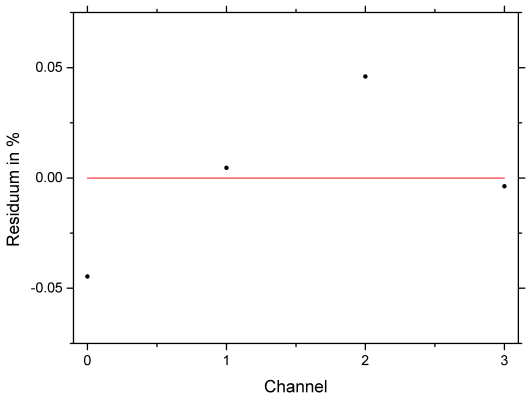

Figure 4.28.: Plot of the residua of the 6.1 MeV peak in percent for the clover crystals.

The BGOs were calibrated with the 511 keV γ ray, originating from the annihilation of the positron from pair production. The BGOs from the back part of the pair spectrometer were not considered for the analysis, because of their small contribution, since the clover detector was sitting only in the front part. The difference in peak statistics between the front and back BGOs is visible in Fig. 4.31, which shows the spectrum of all clover crystals in coincidence with two γ rays with an energy of 511 keV in two front (blue) and two back (red) BGOs.

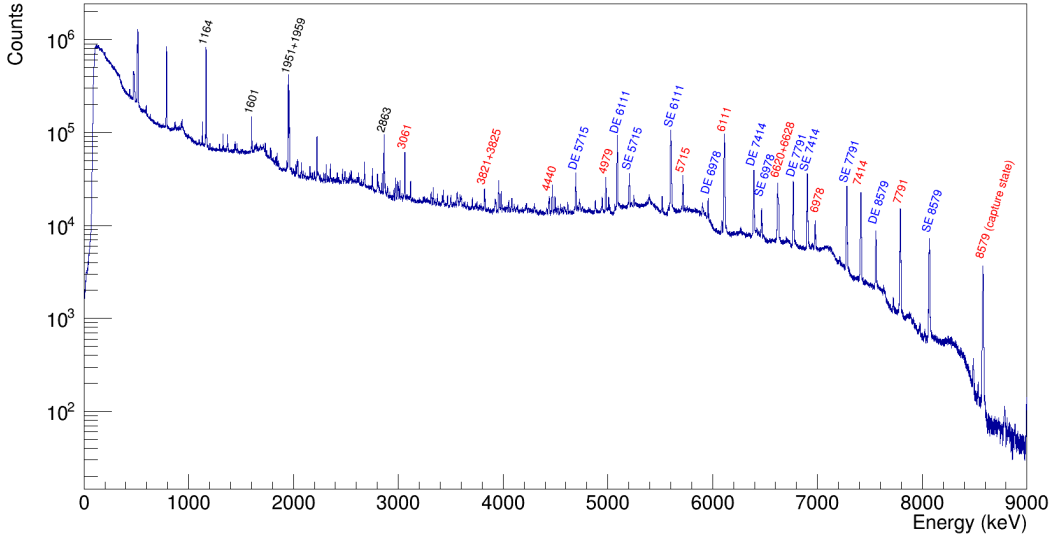

Figure 4.29.: Singles spectrum from all of the clover crystals from the NaCl measurement. The red marked lines are transitions which directly depopulate the capture state. The lines marked in blue show the corresponding single- and double-escape peaks. The black lines are secondary transitions from the decay chain.

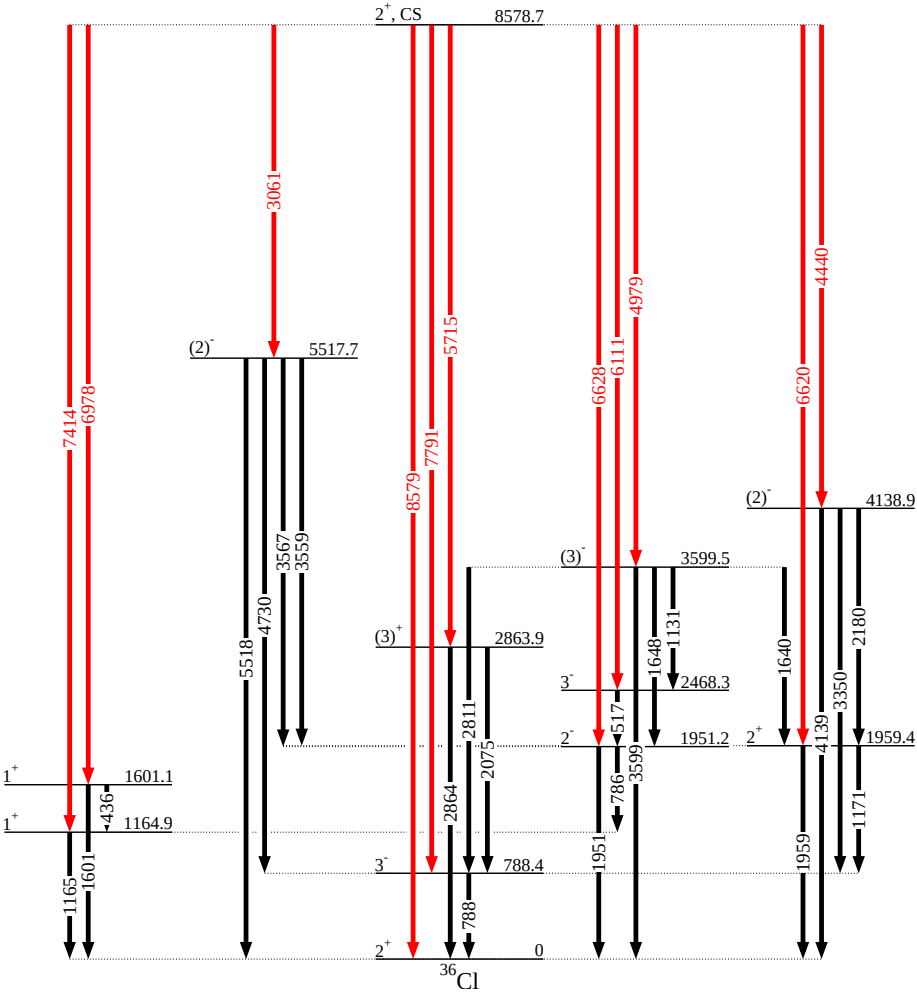

Figure 4.30.: Partial level scheme with prominent lines from ^{36}Cl. The red lines depopulate the capture state, which is the highest bound state from neutron capture. The black lines are secondary transitions in the decay chain [52].

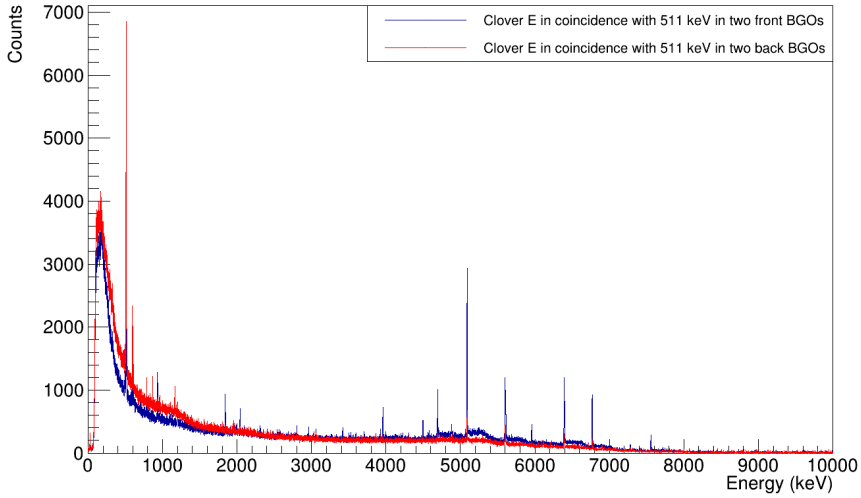

Figure 4.31.: Comparison of the energy of all clover crystals in coincidence with two 511 keV γ rays in two front BGO crystals (blue) and with two 511 keV γ rays in two back BGOs (red).

For the coincidence window 200 ns was set, since the time difference between more than 99 % of the related signals from clover and BGO are within that range. Fig. 4.33 shows the energy-dependent time difference between clover and BGO crystal. Note the energy dependence of the timing difference like for Miniball in Chapter 4.2.3. The time frame for 95 % of the coincident BGO events as well as for 81 % of the coincident events between the clover crystals is at 100 ns, which was dedicated as the coincidence window for these cases. The time difference peak lies on a background which is for the BGO-BGO coincidences at 0.2 %, for the clover-clover coincidences at 1.1 % and for the clover-BGO coincidences at 3.1 %. These numbers show a small background contribution, therefore the background has not been deducted.

The region between 0 and 620 keV was taken to select the 511 keV events in the BGOs. Since the triple coincidence between two BGOs and a clover crystal is a very strict condition it allows to set a wider range for 511 keV selection in this experiment to increase the efficiency. Fig. 4.32 shows the difference between the spectra of clover crystal 2 in coincidence with two front BGOs where the energy range for the 511 keV selection is once between 0 and 620 keV (blue) and once between 430 and 620 keV (red). The DE peaks of the 5715, 7414

and 8579 keV lines in the blue spectrum are 1.5-1.6 times higher than the ones from the red spectrum. The background grows by approximately a factor of 2 as well. However, since for both cases the background stays small, the effect on the peaks is more noticeable and makes the triple coincidence a much stronger filter than the range for the energy selection.

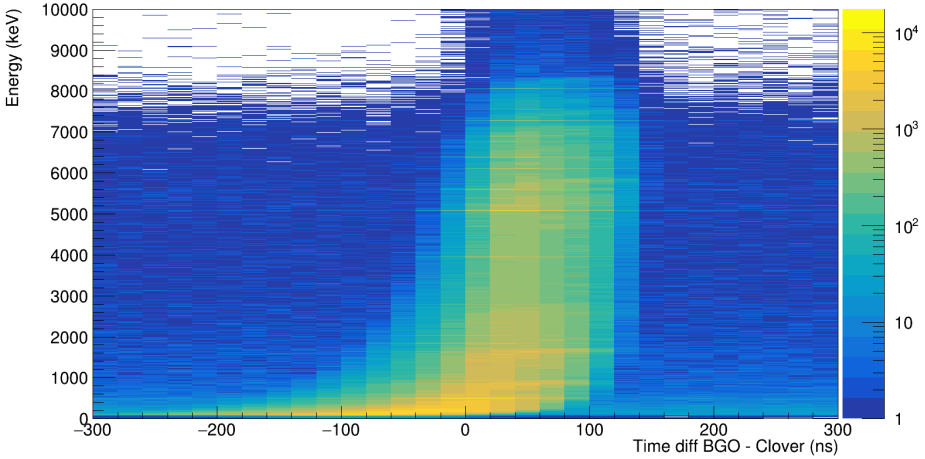

Figure 4.33.: Plot of the γ-ray energy in the germanium clover in dependence of the time difference between the clover signal and a 511 keV γ ray in the BGOs from the front part of the pair spectrometer.

4.3.4. Results

Fig. 4.34 shows a hit pattern with the distribution of the front BGO pairs that detected 511 keV γ rays in coincidence with the double escape events from the 6.1 MeV peak in clover crystal 2. As expected most events are visible in the opposite BGOs from the perspective of clover crystal 2 (see Fig. 4.27).

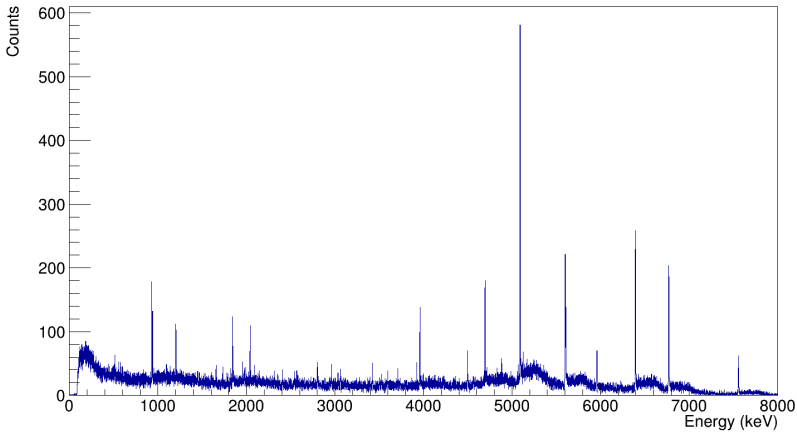

(a)

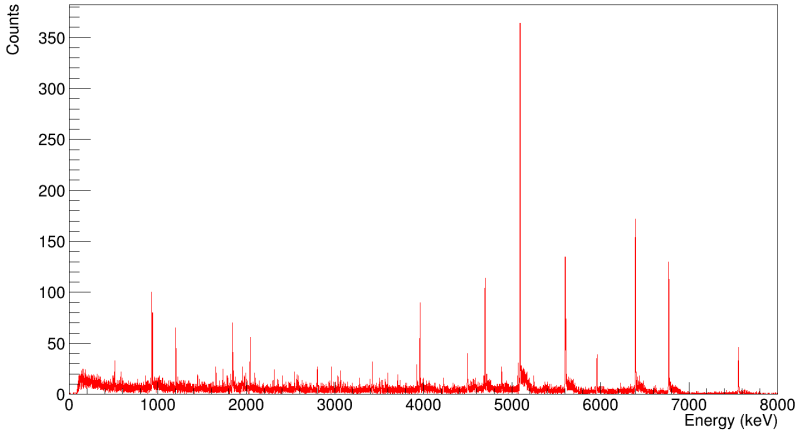

(b)

Figure 4.32.: Comparison of the spectrum of clover crystal 2 in coincidence with two front BGOs with an energy selection for 511 keV from (a) 0 to 620 keV (blue) and from (b) 430 to 620 keV (red).

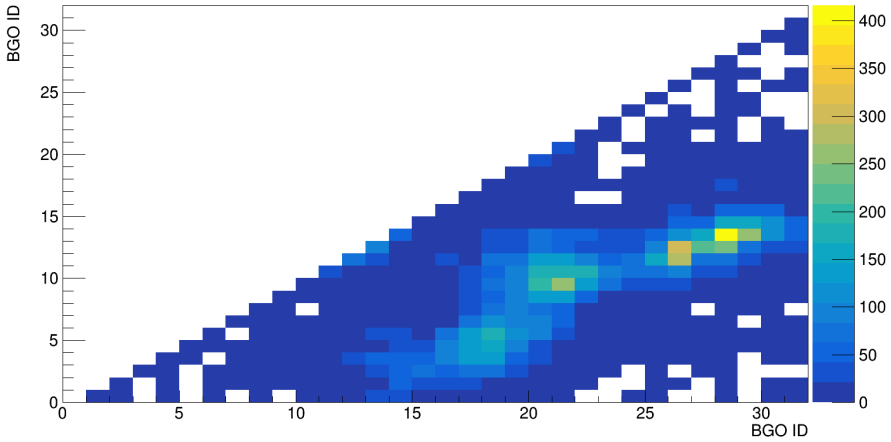

Figure 4.34.: Front BGOs that detected 511 keV γ rays in coincidence with the double-escape events from the 6.1 MeV line in clover crystal 2.

In the following the changes of the spectra employing distinct conditions are discussed.

Histogram (A) of Fig. 4.35 shows the raw spectrum of clover crystal 2 and serves as reference for the following spectra.

As a next step the Compton suppression is activated. This means that no BGOs were firing within the coincidence time window (B). Thus the clover multiplicity was $N_{\text{Clover}} = 1$, which means that the other three germanium crystals serve effectively as part of an AC shield, and the BGO multiplicity was $N_{\text{BGO}} = 0$. This action should decrease the background from the Compton scattered events as well as the single- and double-escape peaks in the spectrum. The expected results are visible in the spectrum of Fig. 4.36 for clover crystal number 2. The 6.1 MeV peak shrinks compared to the raw spectrum as the SE events from the γ rays with energies of 6620 keV and 6628 keV are suppressed.

The application of energy addback from clover crystal 2 and one other crystal while excluding BGO coincidence ($N_{\text{Clover}} \leq 2, N_{\text{BGO}} = 0$), which leads to Compton suppression, is visible in Fig. 4.37 (C). The addback algorithm adds the energy of one crystal to the energy of another crystal if the events of both crystals happened within the coincidence time frame. This step increases the number of counts in the full-energy peaks and scales down the SE and DE peaks.

The spectrum of clover crystal 2 with energy addback for the whole clover and excluded BGO coincidence ($N_{\text{Clover}} > 0, N_{\text{BGO}} = 0$) is shown in Fig. 4.38 (D). In this case the SE and

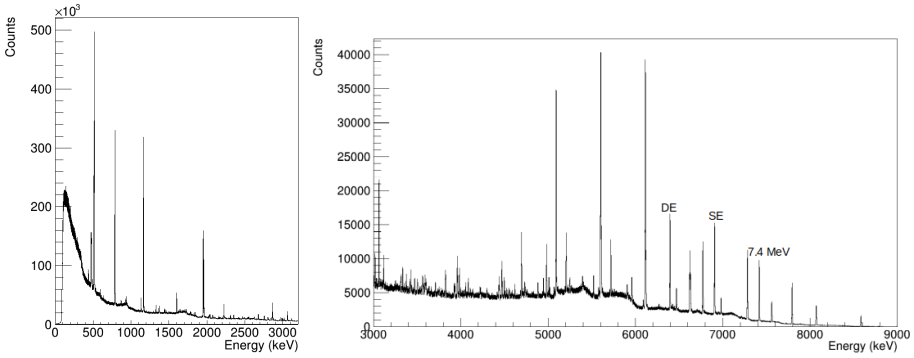

(a) (b)

Figure 4.35.: (A) Raw γ-ray energy spectrum of clover crystal 2 during the NaCl(n,γ) reaction without any conditions for energies (a) up to 3000 keV and (b) above 3000 keV.

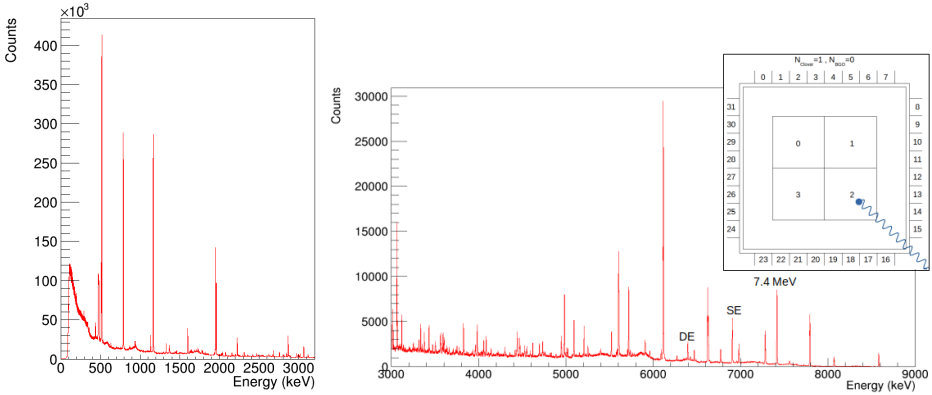

(a) (b)

Figure 4.36.: (B) Spectrum of clover crystal 2 for the NaCl(n,γ) reaction without any other crystals or BGOs firing in coincidence ($N_{\text{Clover}} = 1, N_{\text{BGO}} = 0$) for energies (a) up to around 3000 keV and (b) above 3000 keV.

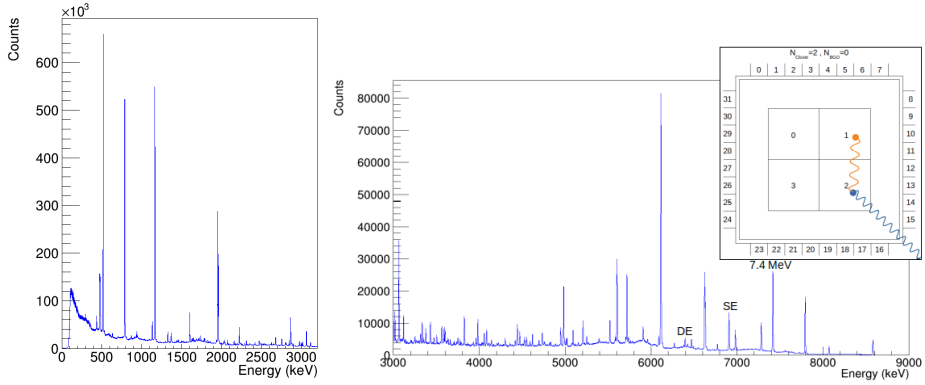

(a) (b)

Figure 4.37.: (C) Spectrum of clover crystal 2 with addback from another crystal and no BGOs firing in coincidence ($N_{\text{Clover}} \leq 2, N_{\text{BGO}} = 0$) for energies (a) up to around 3000 keV and (b) above 3000 keV.

DE peaks are reduced even more and there are more counts in the FE peaks.

The following step activates ELIPS as a pair spectrometer by taking into account the coincidences with the BGO crystals. Fig. 4.39 shows the spectrum of only clover crystal 2 in coincidence with two 511 keV γ rays in two BGOs ($N_{\text{Clover}} = 1, N_{\text{BGO}} = 2$) (E). This procedure lowers the background and highlights the DE peaks. This coincidence spectrum can be shifted to the right by 1022 keV and thus the DE peaks can be used for the reconstruction of the corresponding FE peaks.

The last condition of two 511 keV coincidences in two BGOs with included addback to clover crystal 2 ($N_{\text{Clover}} > 0, N_{\text{BGO}} = 2$) can be observed in Fig. 4.40 (F).

The high number of lines[1] in the histograms allows not to determine the total number of events corresponding to one γ energy to find out the peak-to-total ratio. Therefore, the response of ELIPS to one specific γ energy had to be determined from simulations. The simulations were performed for some of the most intense lines with energies of 3062, 4980, 5715, 6111, 7414, 7790 and 8579 keV and normalized to the counts in the full-energy peaks from the experiment. The comparison of simulation and real experiment for the raw spectrum of clover crystal 2 in Fig. 4.41 shows a good agreement in the higher energy region for the lines that were implemented in the simulation. The divergence around 6 MeV is caused due to non-simulated lines at 6620, 6628 and 6780 keV. Since the lines and

[1] For this reason a γ beam from ELI-NP would be preferred

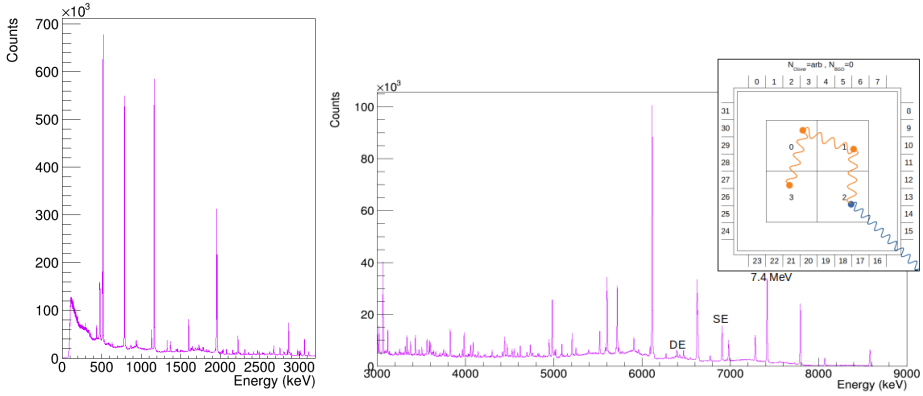

(a) (b)

Figure 4.38.: (D) Spectrum of clover crystal 2 with addback from other crystals and no BGOs firing in coincidence ($N_{\text{Clover}} > 0, N_{\text{BGO}} = 0$) for energies (a) up to around 3000 keV and (b) above 3000 keV.

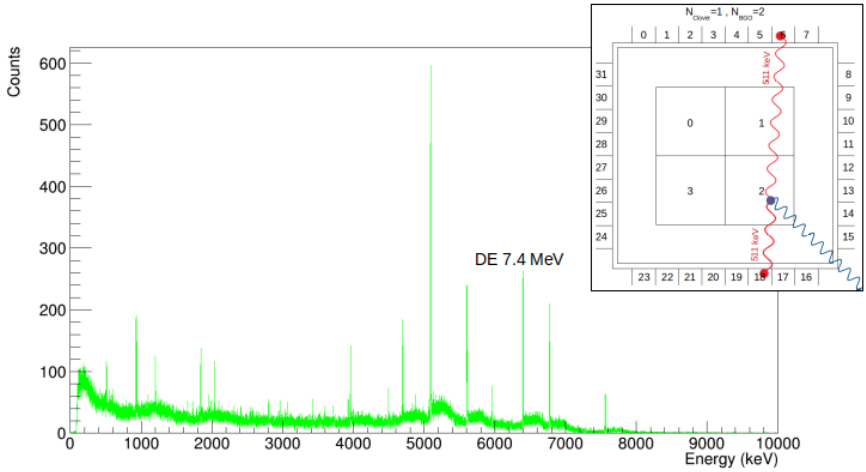

Figure 4.39.: (E) Spectrum of clover crystal 2 in coincidence with two 511 keV γ rays in two front BGOs ($N_{\text{Clover}} = 1, N_{\text{BGO}} = 2$).

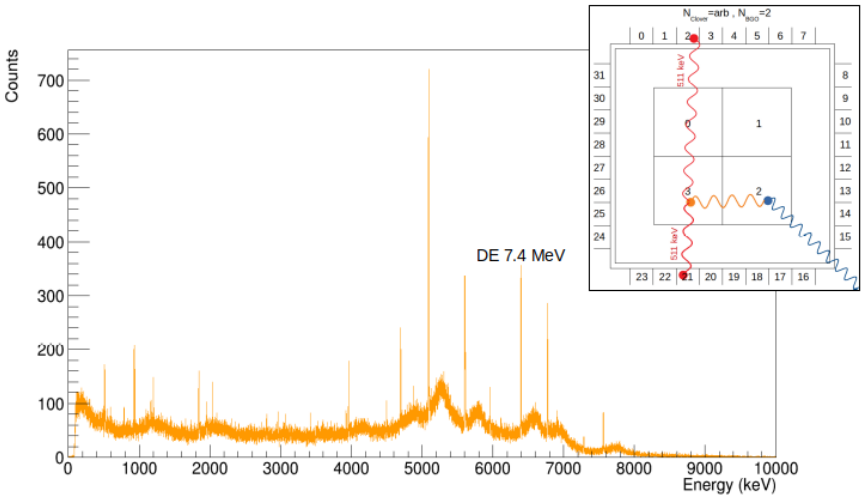

Figure 4.40.: (F) Spectrum of clover crystal 2 in coincidence with two 511 keV γ rays in two front BGOs ($N_{\text{Clover}} > 0, N_{\text{BGO}} = 2$).

background above 8.6 MeV were not simulated as well there is a small deviation at 8.5 MeV. Nevertheless, with the help of the simulation a peak-to-total ratio of $\frac{P}{T} = 0.984(3)$ % could be determined for the 7414 keV line in histogram (A). The corresponding DE peak in histogram (E) has a much better peak-to-total ratio. This was determined via another simulation, which is shown for clover crystal 2 in coincidence with two 511 keV γ rays in two BGOs compared to the real data in Fig. 4.42. The difference in the height of the peaks is caused by slightly different peak widths. The peak-to-total ratio of the DE peak from 7414 keV here is $\frac{P}{T} = 8.33(16)$ %, again employing the results from the simulation. A comparison between these two numbers, which are also presented in Table 4.2, shows an increase of this ratio by a factor higher than 8 through the involvement of the BGOs from ELIPS. Even for the lower statistics the spectrum looks much cleaner by a strong suppression of the background.

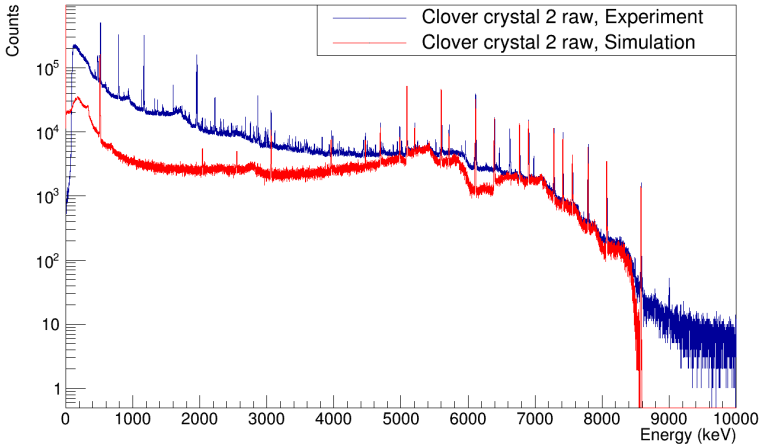

Figure 4.41.: Raw spectrum of clover crystal 2 compared with a simulation ($N_{\text{Clover}} > 0, N_{\text{BGO}} > 0$).

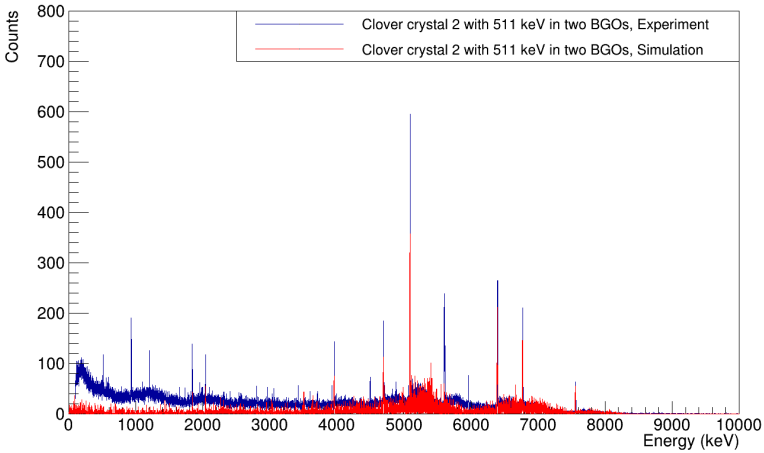

Figure 4.42.: Spectrum of clover crystal 2 in coincidence with two 511 keV in two BGOs compared with a simulation ($N_{\text{Clover}} = 1, N_{\text{BGO}} = 2$).

Table 4.2.: Counts of the 7414 keV FE and DE peak and the corresponding peak-to-total ratio from the spectra of Fig. 4.35 and 4.39.

A:	**Clover crystal 2, raw** $N_{\text{Clover}} > 0, N_{\text{BGO}} > 0$ (Fig. 4.35)
FEP:	109555(331)
$\frac{P}{T}$:	0.984(3) %
E:	**Clover crystal 2, BGO-BGO coincidence** $N_{\text{Clover}} = 1, N_{\text{BGO}} = 2$ (Fig. 4.39)
DEP:	2984(55)
$\frac{P}{T}$:	8.33(16) %

A look into the region between 5.5 and 6.7 MeV allows Fig. 4.43. In the zoomed in

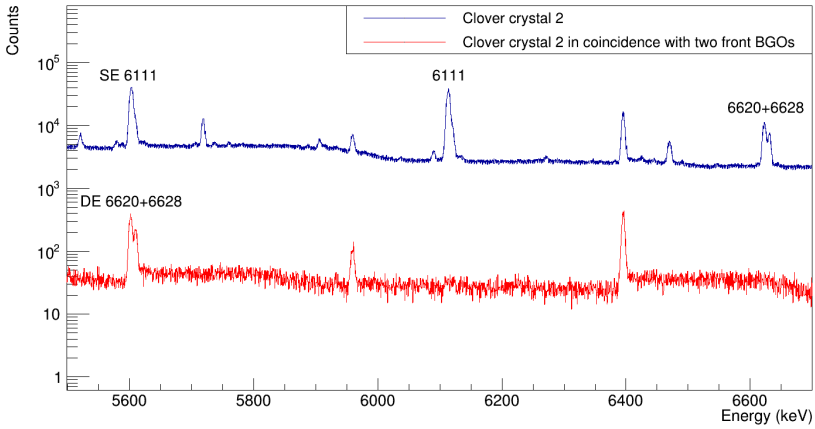

Figure 4.43.: Blue: Zoomed in spectrum from clover crystal 2 with double peak structure at 6.6 MeV. The corresponding DE peaks are covered by the 6.1 MeV SE peak. Red: Zoomed in spectrum from clover crystal 2 in coincidence with two γ rays in two front BGOs. The DE peaks from the 6.6 MeV lines are visible as the SE peak from the 6.1 MeV line is removed.

single spectrum from clover crystal 2 (blue spectrum) a double peak structure is visible in the region around 6.6 MeV. The corresponding DE peaks should be visible around the energy of 5.6 MeV, but they are covered by the SE peak from the 6.1 MeV line. By using the coincidence spectrum from the clovers with two 511 keV γ rays in the BGO crystals (red spectrum) it is possible to see the DE peaks of this double peak structure around 5.6 MeV as the SE peak disappears. This procedure shows just another opportunity for a better analysis of spectra measured with the pair spectrometer.

Tables 4.3-4.8 show the relative efficiencies for the FE, SE and DE peaks of different energies and conditions for clover crystal 2 normalized to the 7414 keV line. These numbers are helpful for the preparation and planning of future experiments with the ELIADE clover and ELIPS. In Table 4.3 the relative efficiencies for the raw spectrum of clover crystal 2 are presented. As expected the efficiency for the FE peak decreases with higher energy. At the same time the sum of $\epsilon_{\text{rel, SEP}}$ and $\epsilon_{\text{rel, DEP}}$ increases compared to the $\epsilon_{\text{rel, FEP}}$ of the corresponding energy. This is due to the increased likelihood for pair production.

Setting the clover multiplicity to 1 and excluding coincident events in the BGOs ($N_{\text{Clover}} = 1, N_{\text{BGO}} = 0$) reduces the SE peak efficiencies compared to the raw spectrum by more than

a factor of 2 and the DE peak efficiencies by a factor of up to more than 7, while the FEP efficiencies stay almost the same (see Table 4.4).

The addback of two or more clover crystals and no coincident events in the BGOs ($N_{\text{Clover}} \leq 2$ or arbitrary, $N_{\text{BGO}} = 0$) increases the FE peak efficiencies more than 2 times compared to the raw spectrum and at the same time the sum of $\epsilon_{\text{rel, SEP}}$ and $\epsilon_{\text{rel, DEP}}$ is up to a factor of almost 1.6 lower (see Tables 4.5 and 4.6) except for the energy of 3062 keV, which has a lower pair production rate as shown in Fig. 2.9.

Fig. 4.44 gives an impression of how the ratio of the relative efficiency for the FE peak to the sum of the relative efficiencies of FE, SE and DE peak behave for different energies and conditions. With higher energies this ratio for the full energy expectedly drops as the pair production rate increases. But under conditions like Compton suppression (red) and additional addback of the clover crystals (blue) the ratio for the FE peaks can be increased. The plots in Fig. 4.45 and 4.46 show the opposite behavior. The ratio for the SE and DE peaks increases with higher energy. Compton suppression (red) and addback of the clover crystals (blue) reduces the ratio for these peaks. Consequently there is a reduction of the ratio for SE and DE peaks and an increase for the ratio of the FE peaks, which is the desired effect.

The activation of the pair spectrometer by taking into account two coincidences in two BGOs while looking on the energy of clover crystal 2 alone or with addback ($N_{\text{Clover}} = 1$ or $> 0, N_{\text{BGO}} = 2$) shows only double-escape peaks in the spectrum and reduces their relative efficiencies up to more than 78 times (see Tables 4.7 and 4.8). The full-energy and single-escape peaks are not identifiable any more.

With the help of these tables it is possible to see how the lines in the spectra behave under different conditions. It is also possible for example to reconstruct the peak intensity of a FE peak in the raw spectrum just with its corresponding DE peak in the coincidence spectrum with two BGOs and the numbers that are given in Tables 4.7 and 4.8. This is helpful if a FE peak in the raw spectrum is covered by some SE or DE peak from another γ-ray energy, since the FE and SE peaks disappear in the coincidence spectrum and clear DE peaks are visible.

Table 4.3.: Relative efficiencies for some FE, SE and DE peaks of different energies in the raw spectrum of clover crystal 2 ($N_{\text{Clover}} > 0, N_{\text{BGO}} > 0$, see histogram (A)).

E (keV)	$\epsilon_{\text{rel, FEP}}$	$\epsilon_{\text{rel, SEP}}$	$\epsilon_{\text{rel, DEP}}$
3062	3.49(6)	0.64(1)	1.27(2)
4979	1.82(3)	1.35(3)	1.53(3)
5715	1.46(3)	1.51(3)	1.44(3)
7414	1.00(2)	1.56(4)	1.45(3)
7790	0.90(2)	1.51(3)	1.41(3)
8579	0.73(2)	1.41(3)	1.27(3)

Table 4.4.: Relative efficiencies for some FE, SE and DE peaks of different energies in the spectrum of clover crystal 2 without BGO coincidences ($N_{\text{Clover}} = 1, N_{\text{BGO}} = 0$, see histogram (B)).

E (keV)	$\epsilon_{\text{rel, FEP}}$	$\epsilon_{\text{rel, SEP}}$	$\epsilon_{\text{rel, DEP}}$
3062	3.21(6)	0.260(5)	0.589(11)
4979	1.74(3)	0.486(9)	0.464(9)
5715	1.42(3)	0.595(11)	0.209(4)
7414	0.94(2)	0.577(13)	0.204(5)
7790	0.85(2)	0.554(12)	0.195(4)
8579	0.70(2)	0.516(12)	0.166(4)

Table 4.5.: Relative efficiencies for some FE, SE and DE peaks of different energies in the spectrum of clover crystal 2 with another addbacked clover crystal and without BGO coincidences ($N_{\text{Clover}} \leq 2, N_{\text{BGO}} = 0$, see histogram (C)).

E (keV)	$\epsilon_{\text{rel, FEP}}$	$\epsilon_{\text{rel, SEP}}$	$\epsilon_{\text{rel, DEP}}$
3062	8.85(16)	0.79(1)	1.420(26)
4979	5.49(10)	1.31(2)	0.933(18)
5715	4.53(8)	1.68(3)	0.265(5)
7414	3.57(8)	1.67(4)	0.365(9)
7790	3.27(7)	1.59(3)	0.268(6)
8579	2.84(6)	1.53(3)	0.262(7)

Table 4.6.: Relative efficiencies for some FE, SE and DE peaks of different energies in the spectrum of clover crystal 2 with addback of all clover crystals and without BGO coincidences ($N_{\text{Clover}} > 0, N_{\text{BGO}} = 0$, see histogram (D)).

E (keV)	$\epsilon_{\text{rel, FEP}}$	$\epsilon_{\text{rel, SEP}}$	$\epsilon_{\text{rel, DEP}}$
3062	10.25(18)	0.89(2)	1.577(28)
4979	6.63(12)	1.42(3)	1.062(20)
5715	5.66(11)	1.92(4)	0.250(5)
7414	4.84(11)	2.00(5)	0.419(10)
7790	4.49(9)	1.90(4)	0.284(6)
8579	3.98(9)	1.88(4)	0.274(7)

Table 4.7.: Relative efficiencies for DE peaks of different energies in the spectrum of clover crystal 2 with 511 keV coincidences in two BGOs ($N_{\text{Clover}} = 1, N_{\text{BGO}} = 2$, see histogram (E)).

E (keV)	$\epsilon_{\text{rel, FEP}}$	$\epsilon_{\text{rel, SEP}}$	$\epsilon_{\text{rel, DEP}}$
3062			0.0171(7)
4979			0.0267(9)
5715			0.0252(8)
7414			0.0272(7)
7790			0.0255(6)
8579			0.0242(7)

Table 4.8.: Relative efficiencies for DE peaks of different energies in the spectrum of clover crystal 2 with addback and 511 keV coincidences in two BGOs ($N_{\text{Clover}} > 0, N_{\text{BGO}} = 2$, see histogram (F)).

E (keV)	$\epsilon_{\text{rel, FEP}}$	$\epsilon_{\text{rel, SEP}}$	$\epsilon_{\text{rel, DEP}}$
3062			0.0161(7)
4979			0.0275(10)
5715			0.0296(9)
7414			0.0335(8)
7790			0.0332(7)
8579			0.0326(8)

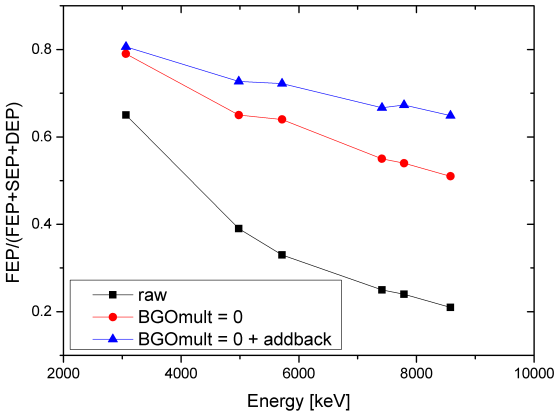

Figure 4.44.: Plot of the ratio of the relative efficiency of the FE peak to the sum of the efficiencies of FE, SE and DE peak under different conditions depending on the energy.

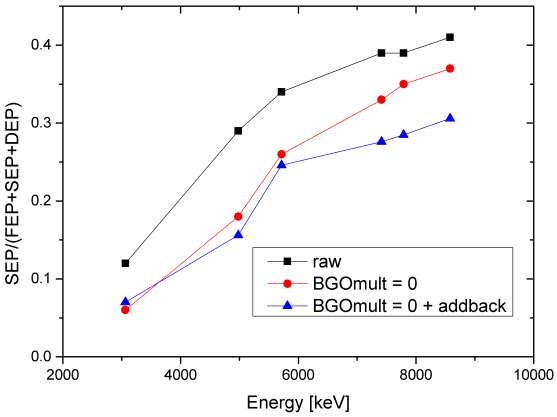

Figure 4.45.: Plot of the ratio of the relative efficiency of the SE peak to the sum of the efficiencies of FE, SE and DE peak under different conditions depending on the energy.

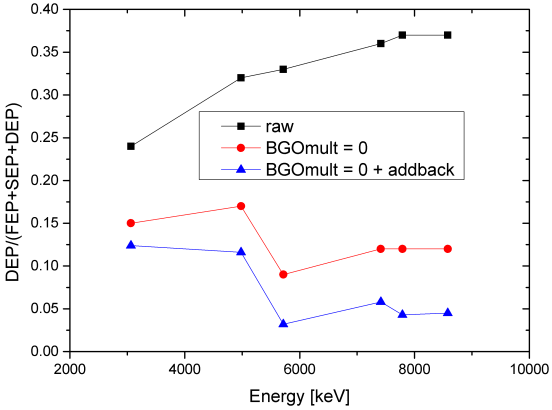

Figure 4.46.: Plot of the ratio of the relative efficiency of the DE peak to the sum of the efficiencies of FE, SE and DE peak under different conditions depending on the energy.

5. Simulation of the Pair Spectrometer

Experiments and detectors in the field of nuclear and particle physics are often very complex and require good planing and preparations beforehand. One effective solution for this kind of challenge are simulations. They also provide an opportunity for the comparison with and verification of already existing experiments and data.

GEANT4 is a powerful toolkit to write such applications in the object-oriented language C++ and has been developed with the help of physicists and software engineers from all over the world at CERN [56, 57, 58, 59]. The program offers a wide variety of materials, particles and interaction mechanisms within a large energy range. Additionally, any kind of setup geometry is either provided or implementable. This leads to the opportunity that any type of detectors, environments and setups can be simulated for a better understanding before and after an experiment. This toolkit is even used in fields like medical physics, space engineering and accelerator design.

Within this framework a Monte Carlo simulation has been created for ELIPS as well. The geometry of the front (white) and back (yellow) BGO crystals corresponds to the one of the real crystals just as the geometry of the aluminum boxes for the back part (green) of the pair spectrometer (colors refer to Fig. 5.1 and Fig. 5.2). For the boxes of the front part (blue) only the aluminum plates that are in between the BGO crystals and the HPGe detector or target and thus are facing to the interaction point were implemented while the side and outer plates were left out as they play a negligible role. Fig. 5.1(a) and (b) show only the back and the front part respectively while Fig. 5.2 shows the whole pair spectrometer as it was modelled in GEANT4.

5.1. Simulation with ^{22}Na

One simulation has been made with a ^{22}Na source in the center between the back part crystals corresponding to measurements described in Chapter 4.1. That source had a diameter of 1 mm and was enclosed in the center of a rectangular acrylic glass case (red) with a size of $(23.5 \times 11 \times 2)$ mm^3 (see Fig. 5.3). The simulation has been performed for $3 \cdot 10^6$ events where each run equals one decay of the sodium source. As the source was placed in the back part of the pair spectrometer only the back part crystals will be taken into account. The BGO energy resolution for 511 keV was set to 14 % corresponding to the experimental value in Chapter 3.2.1 and the gate for the 511 keV peak was from

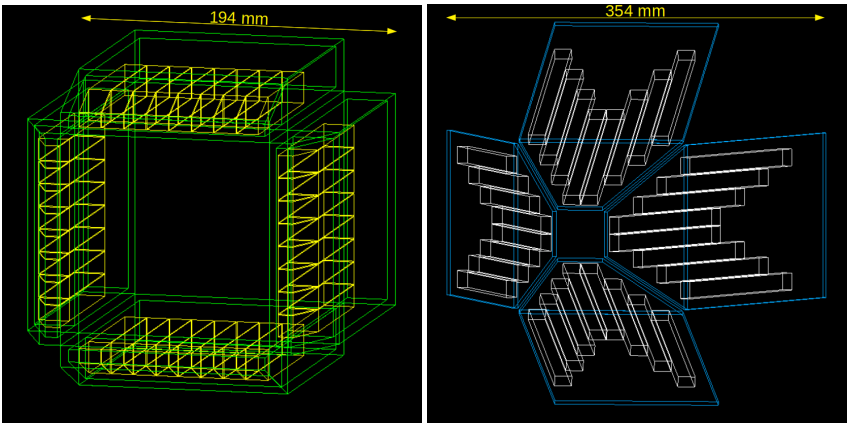

(a) (b)

Figure 5.1.: Visualization of the simulated (a) back part and (b) the front part of the pair spectrometer.

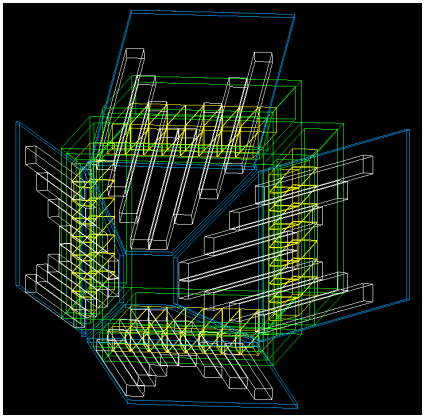

Figure 5.2.: Visualization of the whole simulated pair spectrometer looking on its front. The yellow crystals are the BGOs from the back part, the white ones from the front part. In green are the aluminum boxes from the back part and the blue plates belong to the front part.

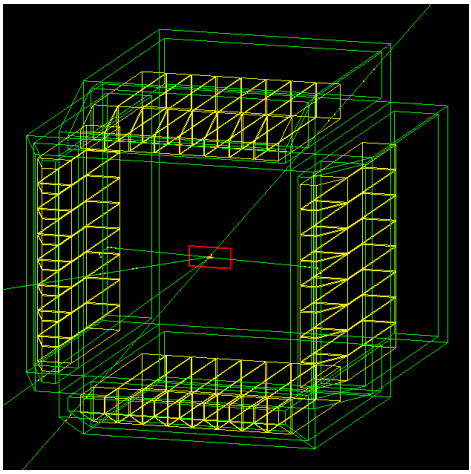

Figure 5.3.: Visualization of the simulated pair spectrometer with a few events emitted by the ^{22}Na source in the center between the back part BGOs. The neutrinos and the front part of the pair spectrometer are not visible.

470 to 550 keV. The simulation provides a number of $N_{\beta+} = 2711599$ β^+ decays, which corresponds to a branching of 90 %. All of these positrons follow the pair annihilation process with electrons and create the same number of correlated γ pairs with an energy of 511 keV[1]. $N_{\text{pairs}} = 252857$ is the number of pairs of 511 keV γ rays that were detected by two opposite BGOs with their full energy. Thus the detection efficiency corresponds to

$$\epsilon_{\text{det, sim}} = \frac{N_{\text{pairs}}}{N_{\beta+}} = 0.093 = 9.3\ \% \tag{5.1}$$

for the back part of the pair spectrometer taking also into account the solid angle of 51.4 %. The experiment with a sodium source in Chapter 4.1 provides a value of $\epsilon_{\text{det, exp}} = (7.4 \pm 1.1)$ %. The number of the detected γ rays with an energy of 511 keV from each individual crystal is shown in Fig. 5.4. The green and blue lines mark the opposed lying BGOs. The number in the center (entries) is the sum of all the counts from the BGOs and has to be divided by two to get the above mentioned number of 511 keV pairs N_{pairs}.

Fig. 5.5 shows the correlation of two BGOs from the back part that detected 511 keV gamma rays at the same time. The most coincidences are visible as expected in the opposing BGO crystal pairs.

[1]The decay into three photons can be neglected [60]

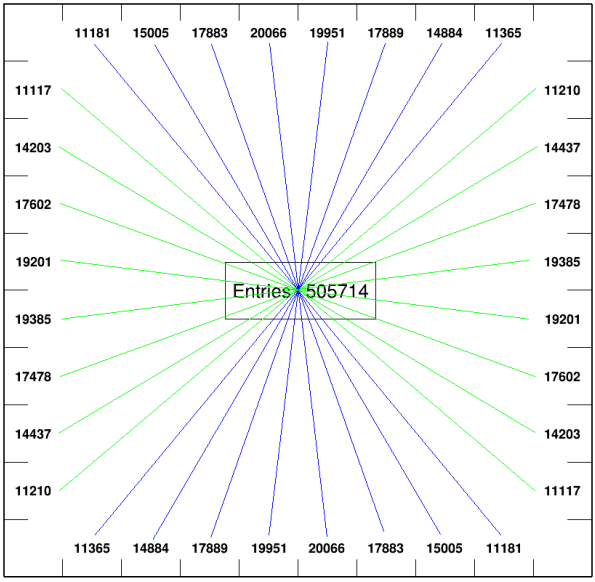

Figure 5.4.: Numbers of the coincident 511 keV γs detected by the opposite BGOs from the simulation. The source was placed in the center between the back part crystals. The sum of all numbers (entries) is shown in the center and has to be divided by two to get the number of pairs.

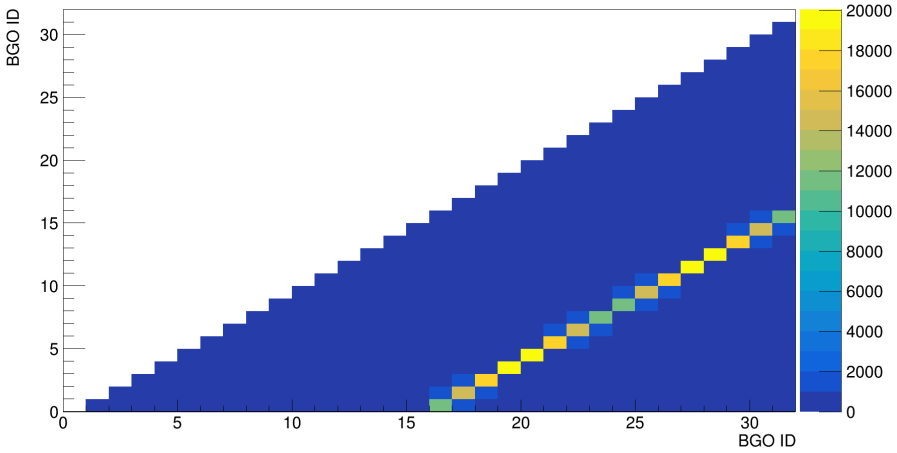

Figure 5.5.: Correlation plot of the two BGOs that detected 511 keV γs in coincidence.

5.2. Simulation as a γ-ray Beam-Intensity Monitor

Another intended purpose is to use ELIPS as a γ-ray beam-intensity monitor. In this case a target (converter) is placed inside of the BGO shield. A high-energy-γ beam hits the converter which leads to pair production and the number of γ-ray pairs with an energy of 511 keV is counted. Since the energy of the beam and the cross section for pair production in this material is known if the energy is well above the threshold, it is possible to conclude the primary beam intensity by the number of 511 keV pairs detected in the BGOs.

In the context of Diandra Richter's bachelor's thesis and this work such a simulation was implemented. A lead cylinder with a diameter and a length of 1 cm was placed into the center of the 32 back part BGOs, thus the front part crystals were neglected in the analysis. Fig. 5.6 shows a scheme of the alignment of the back BGOs around the target from the front view. The simulated back part of the pair spectrometer with the target is visible in Fig. 5.7 (a) and additionally with a beam hitting the target and producing a few 511-keV-γ pairs that escape out of it in Fig. 5.7 (b). For each energy starting from 1.5 MeV and increasing in 0.5 MeV steps up to 10 MeV a simulation was performed with $N_0 = 10^6$ γ rays [32] (ELI-NP provides $\approx 10^{10}$ γ rays/s, therefore the dead time of around 44 µs of the system has to be taken into account for the selection of the converter as well as the cross section for interarction of γ rays with the material, see Fig. 5.8 for lead). The number of detected

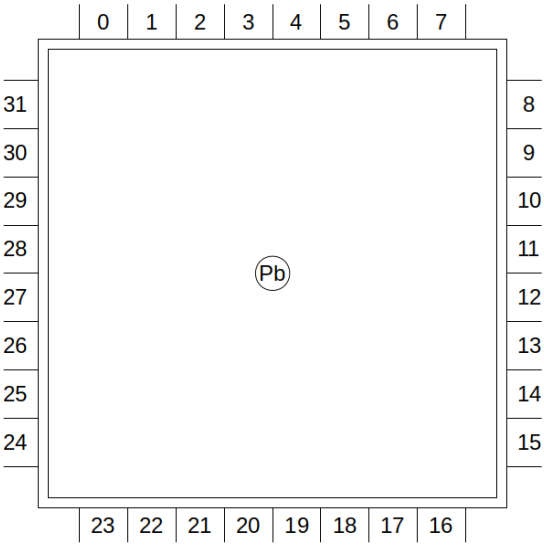

Figure 5.6.: Scheme of the alignment of the 32 back part BGOs and the Pb target from the front view.

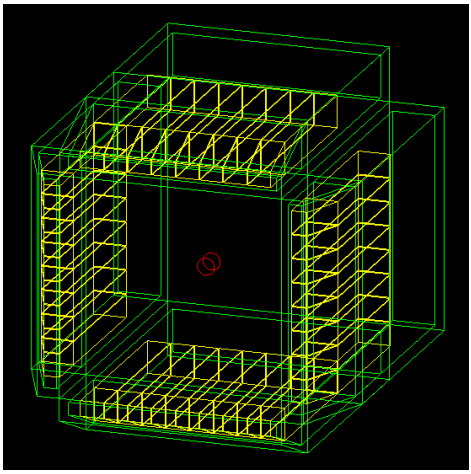

(a)

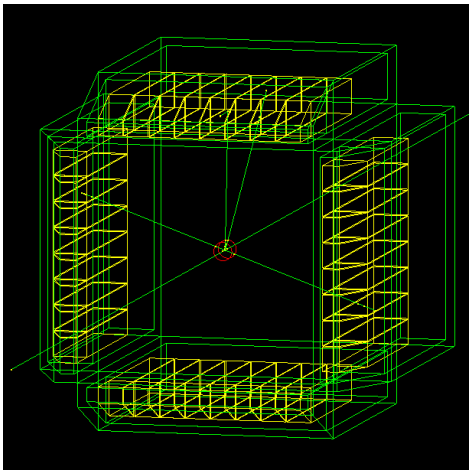

(b)

Figure 5.7.: Visualization of the simulated back part of the pair spectrometer with Pb target (red) (a) and (b) with a beam that hits the target and creates some 511 keV pairs that escape out of the lead.

γ rays with an energy of 511 keV N_{det} in opposite BGO crystals provides a direct value for the simulated detection efficiency of the back part of the pair spectrometer

$$\epsilon_{\text{det, sim}}(E) = \frac{N_{\text{det}}}{N_0}. \tag{5.2}$$

This efficiency has been compared with a theoretically calculated detection efficiency $\epsilon_{\text{det, theo}}(E)$. For the latter some simplified assumptions have been made. First the incoming beam hits the cylindrical target plane in the center and produces electron-positron pairs within the 10 mm thick target with a probability of $P_{\text{PP, Pb}}(E)$ depending on the energy of the beam. Both of the two γ rays with an energy of 511 keV originated from the positron-electron annihilation leave 5 mm of the target back-to-back perpendicular to the longitudinal axis without interaction with a likelihood of $P_{\text{Pb, esc}} = 0.4124^2 = 17.01$ %. Finally both pass the aluminum plate of 3 mm thickness and enter the 19 mm thick BGO crystals orthogonally. The probability for penetrating the aluminum without interaction is $P_{\text{Alu, esc}} = 0.9345^2 = 87.33$ % and for photoelectric absorption in the BGOs it is $P_{\text{PE, BGO}} = 0.5291^2 = 27.99$ %. The solid angle that is covered by the 32 back part crystals is $\epsilon_{\text{geo}} = 51.4$ %. The result of the theoretical detection efficiency depends on the beam energy and is the product of the above mentioned probabilities [32]

$$\epsilon_{\text{det, theo}}(E) = P_{\text{PP, Pb}}(E) \cdot P_{\text{Pb, esc}} \cdot P_{\text{Alu, esc}} \cdot P_{\text{PE, BGO}} \cdot \epsilon_{\text{geo}}. \tag{5.3}$$

As an example for a beam with an energy of 2 MeV the probability for pair production in the lead converter is $P_{\text{PP, Pb}}(2\text{ MeV}) = 0.06$. This value leads to a theoretical detection efficiency of $\epsilon_{\text{det, theo}}(2\text{ MeV}) = 0.001281 = 0.1281$ %. The initial number of γ rays can be determined by

$$N_{\text{in}} = \frac{N_{\text{det}}}{\epsilon_{\text{det, theo}}(E)} \tag{5.4}$$

with N_{det} as the number of detected 511 keV pairs in two opposite BGO crystals. The simulation provides $N_{\text{det}} = 1517$ of those 511 keV pairs out of $N_0 = 10^6$ shots of γ rays with an energy of 2 MeV on the target. This results in a simulated detection efficiency of $\epsilon_{\text{det, sim}}(2\text{ MeV}) = 0.001517 = 0.1517$ %. Taking the 1517 pairs from the simulation and the theoretical detection efficiency to calculate the initial number of γ rays from Eq. 5.4 leads to $N_{\text{in}} = 1183864$. The number is 18.4 % higher than N_0. For the other energies between 1.5 and 10 MeV the deviation lies between 10.8 % and 27.1 % [32]. Those discrepancies occur due to the above mentioned simple assumptions. Table 5.1 shows the detection efficiencies for energies between 1.5 to 10 MeV.

Table 5.1.: Theoretical and simulated detection efficiencies of the γ-beam-intensity monitor for different energies and a cylindrical lead converter of 1 cm diameter and 1 cm length [32].

E (MeV)	N_{det}	$P_{\text{PP,Pb}}(E)$	$\epsilon_{\text{det, theo}}(E)$ (10^{-3})	N_{in}	$\epsilon_{\text{det, sim}}(E)$ (10^{-3})
1.5	480	0.020	0.43	1107511	0.48
2	1517	0.060	1.28	1183864	1.52
2.5	2453	0.096	2.05	1195799	2.45
3	3411	0.127	2.71	1260807	3.41
3.5	4166	0.153	3.28	1271142	4.17
4	4673	0.177	3.78	1236018	4.67
4.5	5300	0.198	4.23	1252473	5.30
5	5747	0.217	4.64	1239316	5.75
5.5	6141	0.234	5.01	1226869	6.14
6	6604	0.250	5.34	1236297	6.60
6.5	6961	0.264	5.65	1231645	6.96
7	7402	0.278	5.94	1246529	7.40
7.5	7528	0.290	6.21	1213103	7.53
8	7788	0.302	6.46	1205929	7.79
8.5	8071	0.313	6.69	1206172	8.07
9	8188	0.323	6.91	1184200	8.19
9.5	8360	0.333	7.12	1173477	8.36
10	8498	0.343	7.32	1160220	8.50

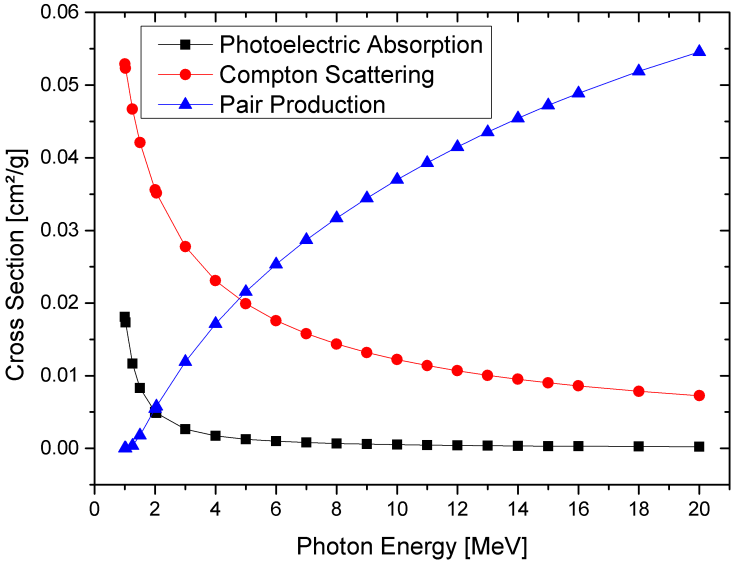

Figure 5.8.: Cross section for photoelectric effect, Compton scattering and pair production in lead depending on the photon energy [18].

6. Discussion

A comparison between a real test with a sodium source in Chapter 4.1 and a simulation in Chapter 5.1 shows similar results. This is a proof for reasonable assumptions in the implementation of the simulation as well as for the comparability of simulation and experiment. The still existing difference between experimental and simulated efficiency is expected to be caused among other factors by the dead time of the readout electronics (≈44 µs) and the background radiation (≈13 counts per second and MPPC) which exist in the real measurements but were not taken into account in the simulation.

With the first experiments outside of the TU Darmstadt the pair spectrometer has been successfully tested as it worked as expected and showed valuable results. The desired high-energy peaks are clearly visible in the spectra and the corresponding SE and DE peaks provide a high contribution. This contribution increases with higher energies hence the pair spectrometer gains in value as well, since more full-energy events can be reconstructed in connection with the 511 keV coincidences from the BGO crystals and Compton background can be suppressed which helps a lot for the analysis of the spectra.

In experiments with more different γ lines the spectrum looks more complicated and the analysis brings more difficulties. The Compton suppression alone which is excluding events with BGO or other clover crystal coincidences reduces the total amount of entries to 58.8 %. The largest reduction applies for the Compton scattered events as well as for the single- and double-escape peaks, while the full-energy peaks stay almost unaffected as shown in Fig. 6.1. The activation of the pair spectrometer by accepting only events of clover crystal 2 in coincidence with two BGOs removes more than 99.8 % of the entries. Anyway, the spectrum is of a much higher quality since most of the background is removed as well. Especially at high energies the natural lines can be overlapped by DE and SE peaks (see Fig 4.43). The coincidence spectrum with the BGOs can remove such overlaps and helps to find out which lines belong to which FE peak. The identified DE peaks and the known efficiency make it possible to find out the full intensity of the FE peaks.

Some common anti-Compton shields from BGO in connection with germanium detectors were used for example in projects like GAMMASPHERE [61], ν-ball [62], TIGRESS [63] or simulated and designed for the MINIBALL spectrometer at the HIE-ISOLDE facility at CERN [64]. The peak-to-total ratio for the ^{60}Co lines improves between the unsuppressed and suppressed spectrum by a factor of 2.8 for GAMMASPHERE, around 1.5 for ν-ball, 1.8 for TIGRESS and about 1.6 for MINIBALL. With ELIPS the peak-to-total ratio for the 7414 keV line shows an improvement of a factor of 8.5 for the spectrum of clover crystal 2

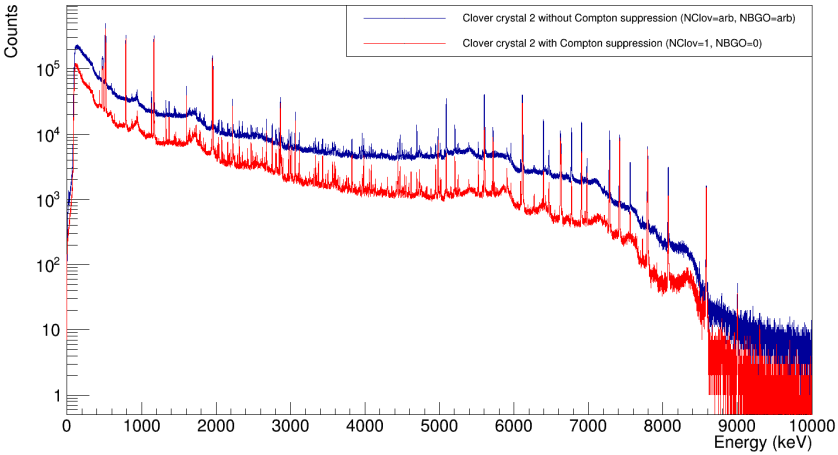

Figure 6.1.: Spectrum of clover crystal 2 without (blue) and with Compton suppression (red).

in coincidence with two BGOs. This demonstrates a significant increase of the quality of the spectra with the pair spectrometer even if a direct comparison is not possible due to the higher energy of the γ ray than those coming from the ^{60}Co source.

The results from the experiments with ELIPS show how the importance of this instrument for gamma spectroscopic investigations increases with higher energies. The rising pair production rate in the germanium leads to higher ratios of SE and DE peaks compared to the FE peaks. Features like addback of the germanium crystals, the activation of Compton suppression or the application of two BGO coincidences with the germanium detector increases the efficiency for the detection of FE peaks compared to the corresponding escape peaks. The use of the BGO coincidences reduces also the total amount of entries, but the reduction is not equally distributed, but rather removes the Compton scattered events. As a consequence the peak-to-total ratio improves and the peaks are more clearly visible.

In general, it is possible to estimate an overall efficiency for ELIPS using a simulation, provided the dimensions and position of the central γ-ray detector are known. With a bulky detector the mass attenuation for high-energy γ-rays gets higher but the probability for pair production is rising as well. This leads consequently to more pair annihilation events which potentially could leave the central detector and afterwards be detected and reconstructed by the BGO shield. But on the other hand the probability for γ rays with an energy of 511 keV to escape decreases with bigger detectors. In a small detector the situation is vice versa. The likelihood for pair production and thus for e^+e^- annihilation is reduced, but the probability for the gamma rays to escape out of less material becomes higher. Due to these facts a prediction for the efficiency of the pair spectrometer or the outcome of an experiment is only roughly possible with a simulation. Additionally, for the ELIADE detectors the data from the ^{35}Cl$(n,\gamma)^{36}$Cl experiment can be used for energies up to 8.6 MeV since the IFIN clover has comparable dimensions. For the experiments at ELI-NP ELIPS will be a very efficient instrument especially in NRF studies for the investigation of the Pygmy Dipole Resonance (PDR) where the energy range is around 5-9 MeV or the Giant Dipole Resonance (GDR) with even higher energies [65]. In these energy regions pair production has a high contribution or even dominates. A broad resonance can also decay into many discrete levels and result in many lines in the spectrum where the pair spectrometer could provide some order. The demand for a higher efficiency of the ELIADE detectors and the improvement of the quality of the spectra makes ELIPS a useful tool for these and other kind of measurements where γ rays of high energy are used.

7. Summary and Outlook

In this work a pair spectrometer based on a HPGe detector and a granular BGO detector has been developed, assembled and tested. Classic pair spectrometer reconstruct the full energy on the basis of the trajectory of positron and electron in a magnetic field. This magnetic field can disturb measurements and devices that are sensitive to magnetic fields. ELIPS, in contrast, uses the produced γ rays with an energy of 511 keV from pair annihilation for reconstruction. It consists in total out of 64 scintillators - 32 BGO crystals in its front and 32 in its back part. The development and design of the crystals and the pair spectrometer as a whole is based on the mechanical structure of ELIADE at ELI-NP and its 8 germanium clover detectors since all the components have to be compatible with each other. For the reason of high granularity MPPC arrays are used for the readout instead of PMTs. From a test with a ^{22}Na source the BGOs show relative energy resolutions of 11-14 % at 511 keV and are wrapped inside of an ESR foil. The efficiency to detect two back-to-back γ rays with an energy of 511 keV in the 32 BGO crystals from the back part was determined to 7.4 %.

To get clean γ-ray beams with high energies the original plan was to test ELIPS at ELI-NP. Due to delays in the construction of the accelerator this was not possible. Another proposal for a test at the NewSUBARU synchrotron radiation facility in Japan has already been accepted, but the experiment was cancelled due to the corona pandemic.

As an alternative in order to have high-energy γ rays a test experiment with protons shot on a LiF target at the University of Cologne has been performed. It showed two prominent lines in the high-energy region of the Miniball detector - one at 6.1 MeV and one at 17.6 MeV. The corresponding DE peaks made around 36 % and 83 % of the FE peaks, respectively. With the reconstruction mechanism of ELIPS more than 2 % of the 6.1 MeV FE peak and around 6 % of the 17.6 MeV FE peak could be reconstructed.

At the ILL a neutron capture experiment was performed with a NaCl target and an IFIN-HH clover detector. Several high-energy peaks between 1.1 and 8.6 MeV have been produced. The highest roughly corresponds to the point where the cross section for Compton scattering and pair production in germanium equal. Hence, this is an important region to challenge a pair spectrometer. The focus was directed on the 7414 keV peak. The activation of the Compton suppression by excluding the events with a BGO coincidence shows less statistics, but increases the relative full-energy-peak efficiency up to 4.8 times by adding an addback algorithm. The use of the double-escape events in two BGOs for reconstruction decreases the statistics even more. Nevertheless, the enhancement of the $\frac{P}{T}$ reaches a factor of >8 compared to the raw spectrum. Doublets of FE, SE and DE peaks with FE, SE and DE

events from other transitions could be disentangled. After this, the total intensities could be reconstructed.

One of the first and important parameters of a gamma-beam facility is the beam intensity. The pair spectrometer allows for beam-intensity measurements by placing a converter in the BGO shield. The sensitivity can be easily adapted to beam energy and intensity by an appropriate choice of the converter. A simulation of the pair spectrometer as a γ-ray beam-intensity monitor has also been implemented and compared to calculations. The simulated efficiency of ELIPS to detect two γ rays with an energy of 511 keV from a ^{22}Na source in two opposite BGOs of the back part is 9.3 %.

One potential physics case for the future of the pair spectrometer could be the investigation of the pair production cross section close to the threshold of $E_{\text{pair}} = 1022$ keV. Fig. 7.1 shows on its x axis the energy above 1022 keV where pair production is possible and on the y axis the cross section for pair production in units of the Bethe-Heitler formula. Previous cross-section measurements close to the threshold at 1022 keV resulted in values that are about 2 times that of the Bethe-Heitler prediction [66]. This requires further investigation. The pair spectrometer together with the fine tuneable γ-ray beam at ELI-NP could prove to be a perfect combination for this kind of measurement. In any case the enhancement of the efficiency, the peak-to-total ratio and the possibility to use it as a gamma-beam-intensity monitor will make the pair spectrometer a unique and powerful instrument for future experiments with high-energy γ rays.

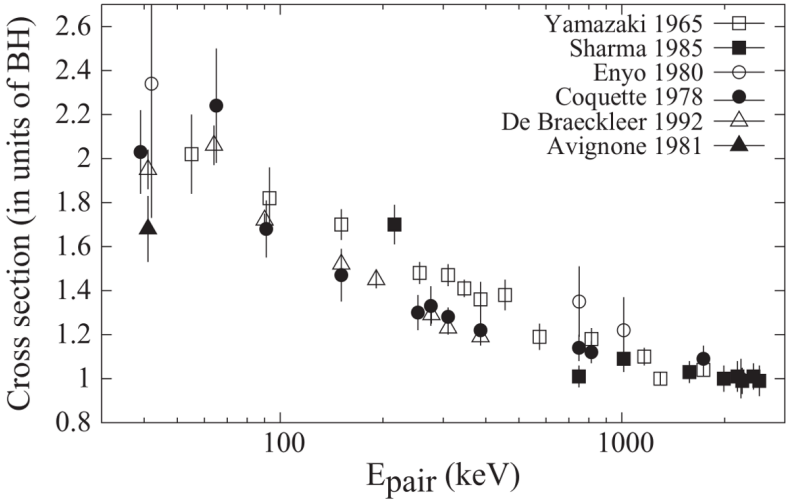

Figure 7.1.: Previous measurements of the pair production cross section in Germanium in units of the Bethe-Heitler formula. Reprinted Figure with permission from [66] Copyright 2022 by the American Physical Society.

A. Technical Drawings of BGOs

A.1. Back BGOs

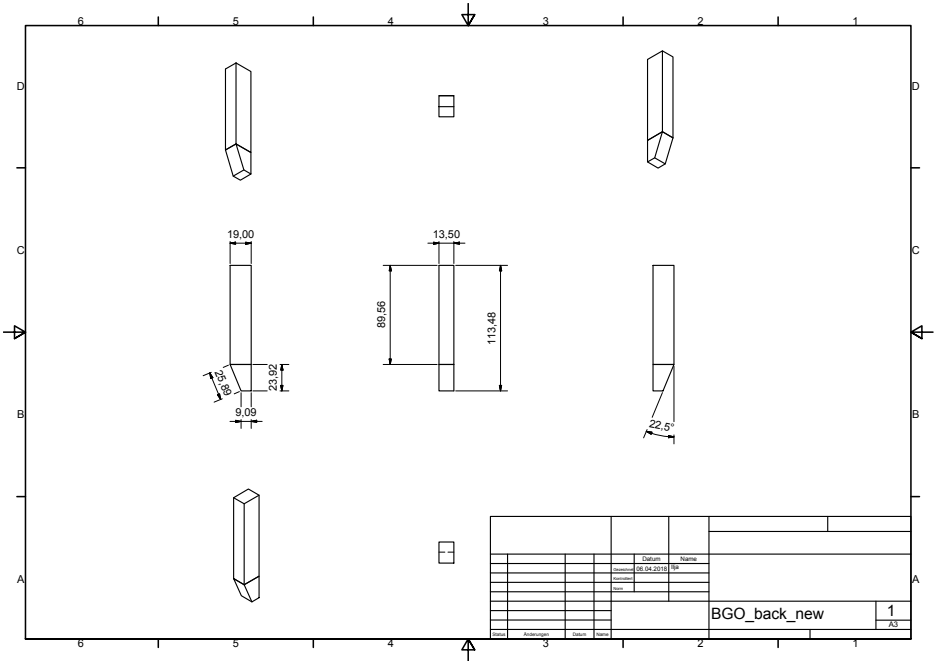

Figure A.1.: Technical drawing of a BGO from the back part of the pair spectrometer. The numbers are given in mm.

A.2. Front BGOs

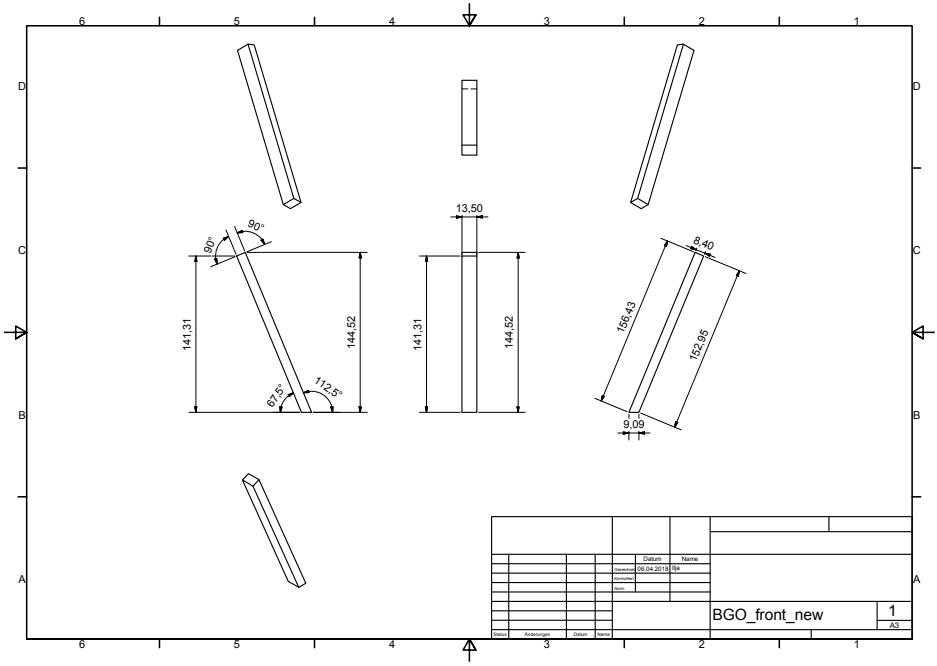

Figure A.2.: Technical drawing of a BGO from the front part of the pair spectrometer. The numbers are given in mm.

B. Technical Drawings of Aluminum Boxes

B.1. Back Part Boxes

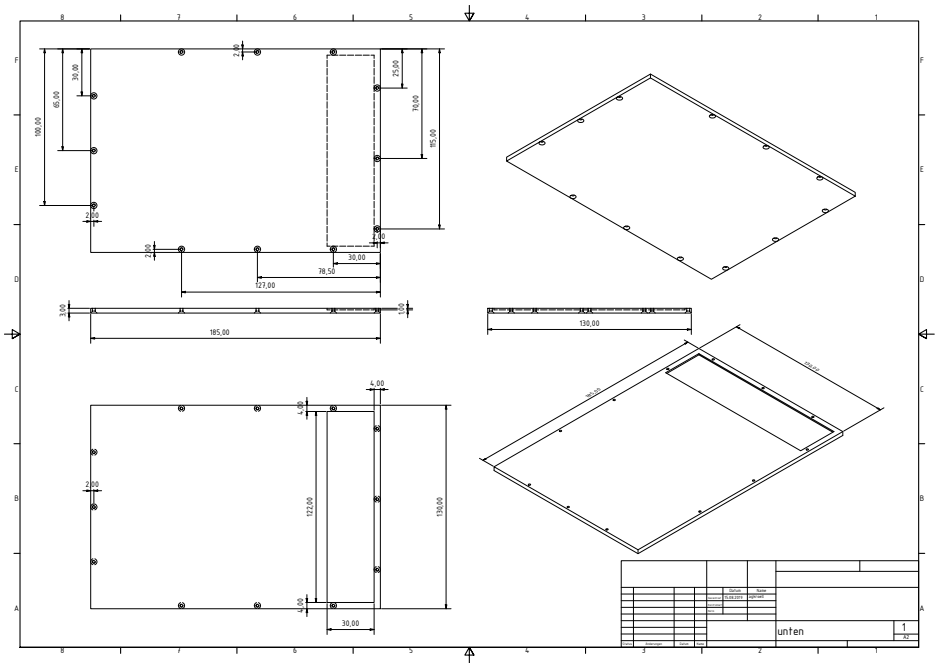

Figure B.1.: Technical drawing of the bottom plate of a box from the back part of the pair spectrometer.

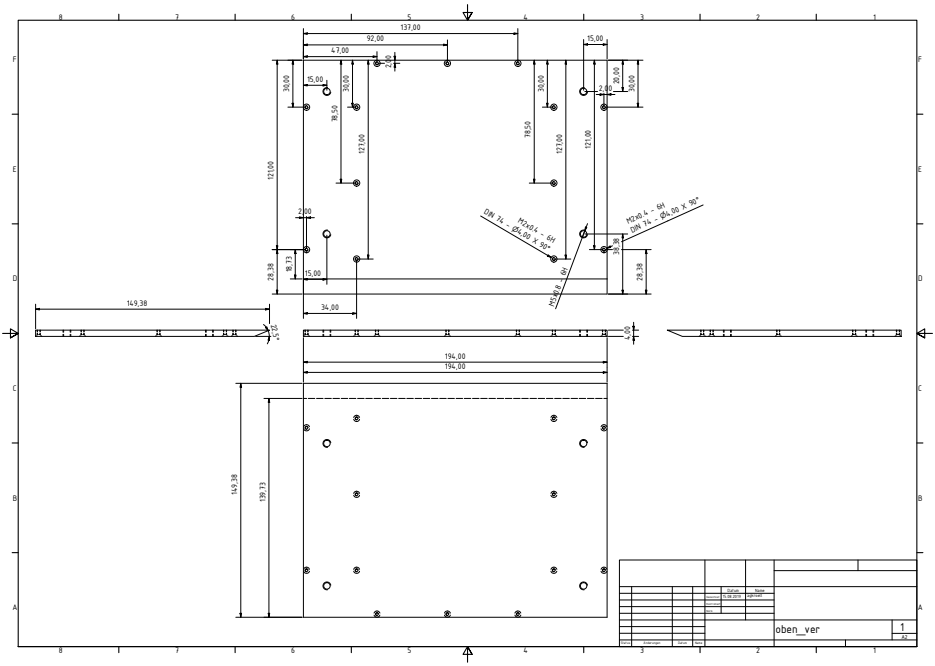

Figure B.2.: Technical drawing of the top plate of a box from the back part of the pair spectrometer.

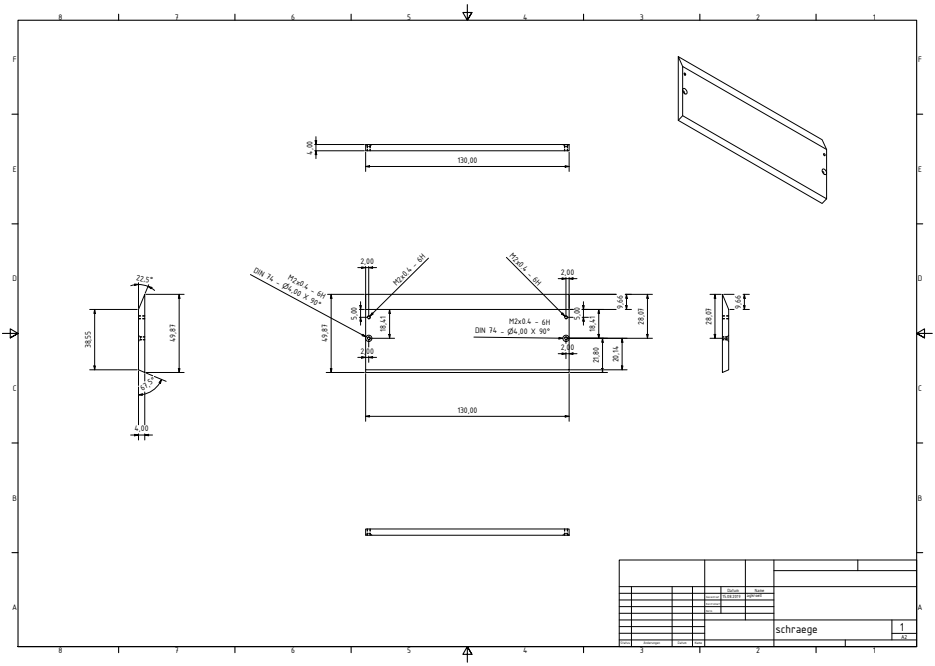

Figure B.3.: Technical drawing of the sloping plate of a box from the back part of the pair spectrometer.

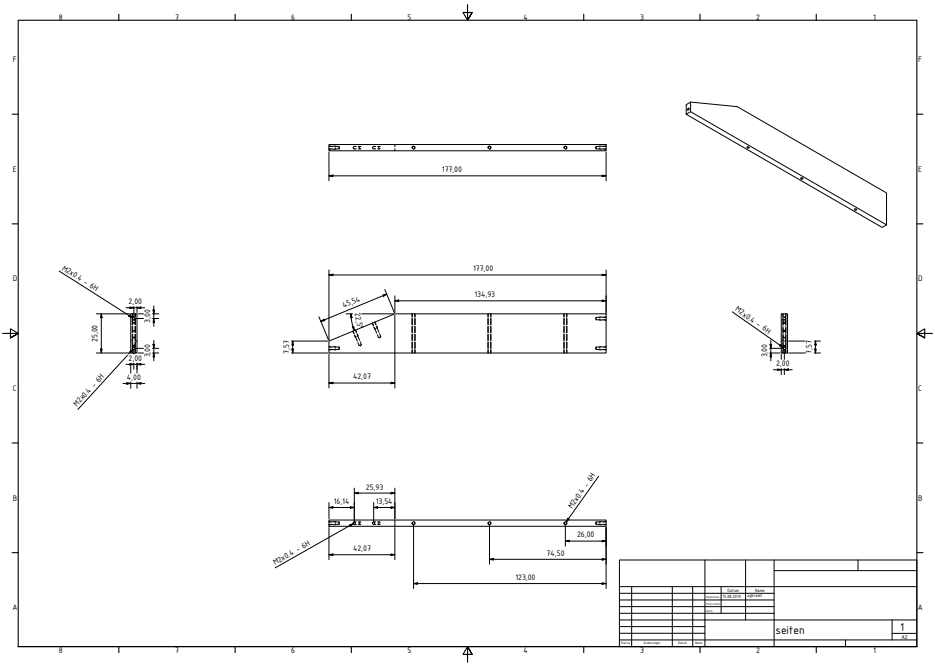

Figure B.4.: Technical drawing of the side plate of a box from the back part of the pair spectrometer.

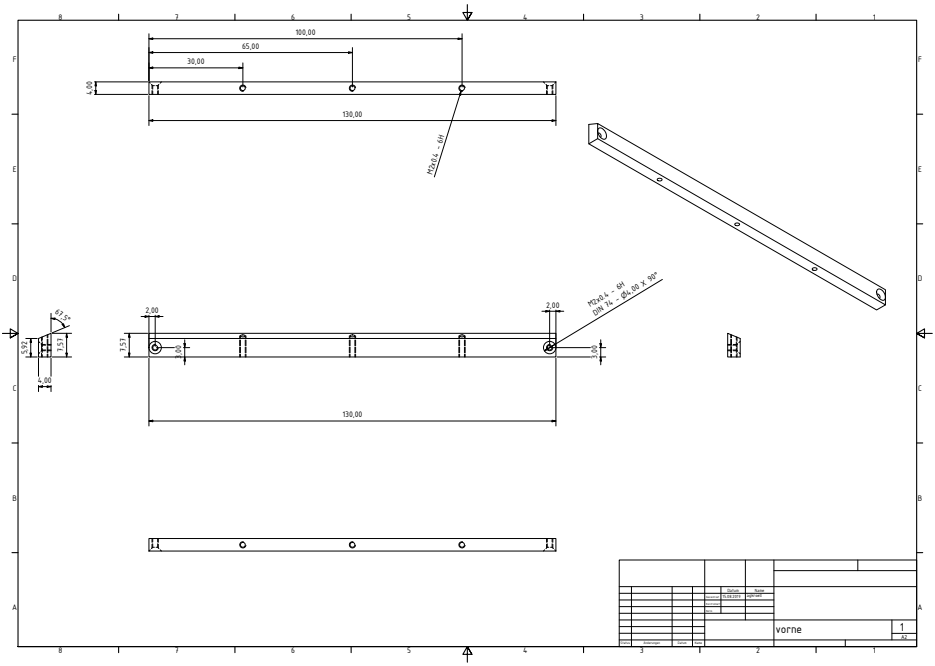

Figure B.5.: Technical drawing of the front plate of a box from the back part of the pair spectrometer.

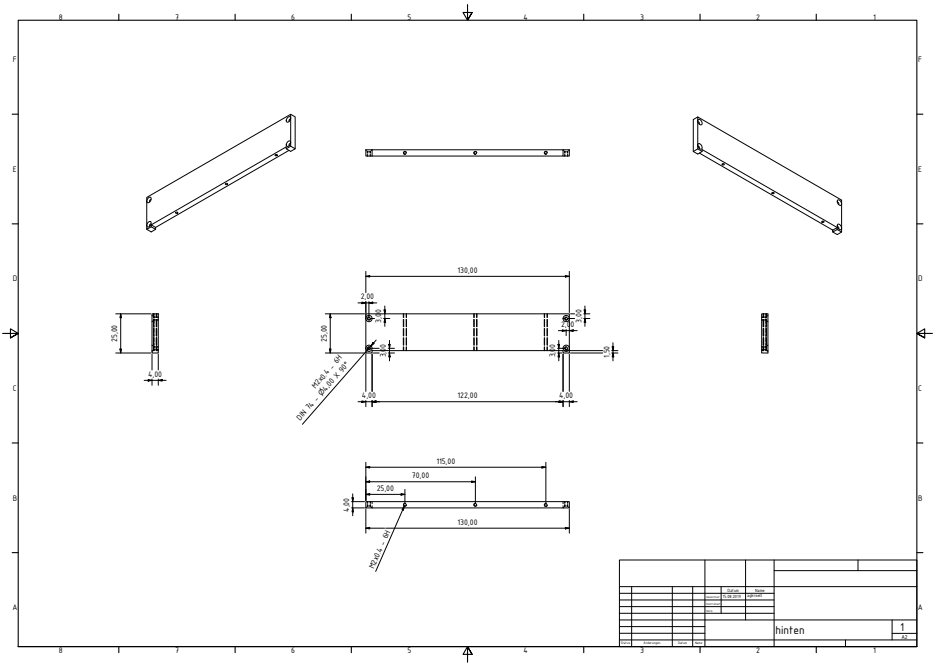

Figure B.6.: Technical drawing of the rear plate of a box from the back part of the pair spectrometer.

B.2. Front Part Boxes

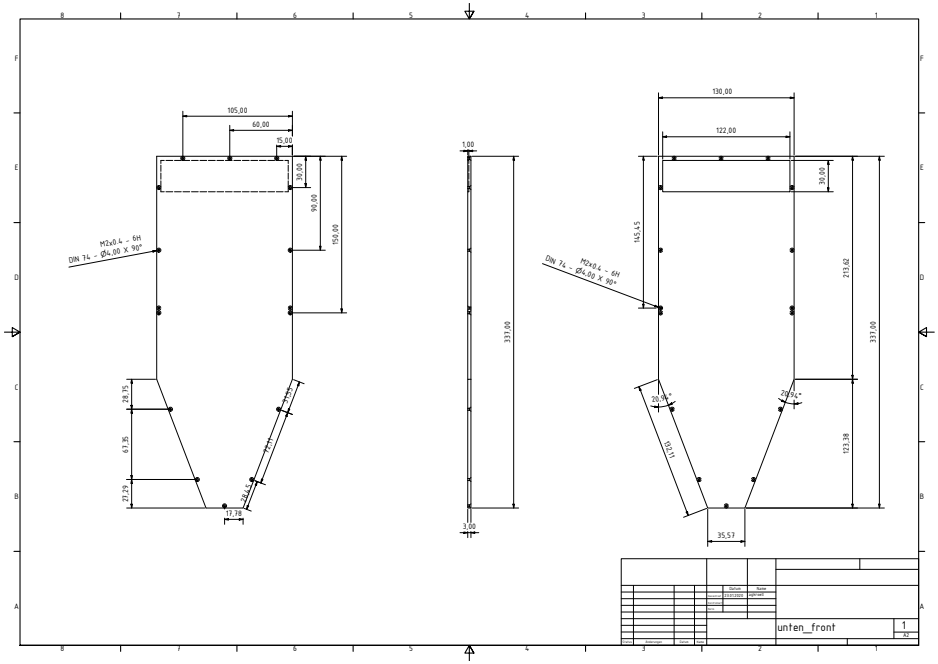

Figure B.7.: Technical drawing of the bottom plate of a box from the front part of the pair spectrometer.

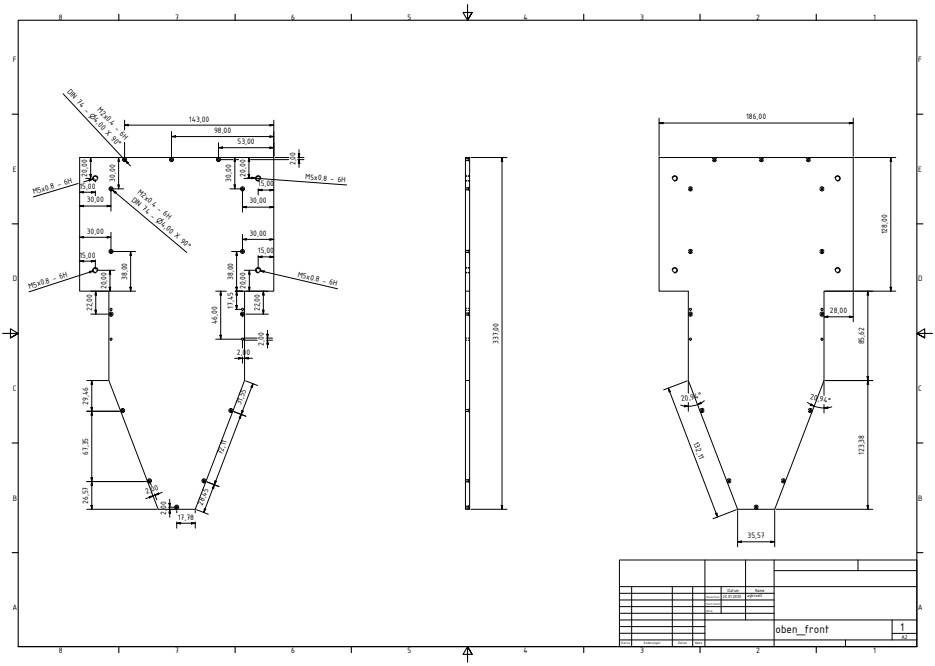

Figure B.8.: Technical drawing of the top plate of a box from the front part of the pair spectrometer.

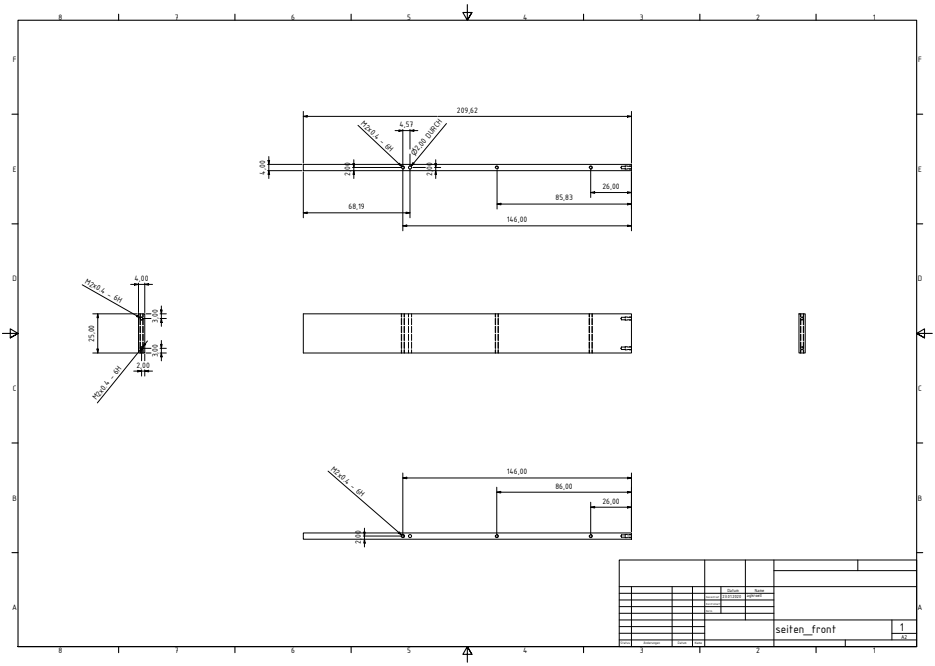

Figure B.9.: Technical drawing of the side plate of a box from the front part of the pair spectrometer.

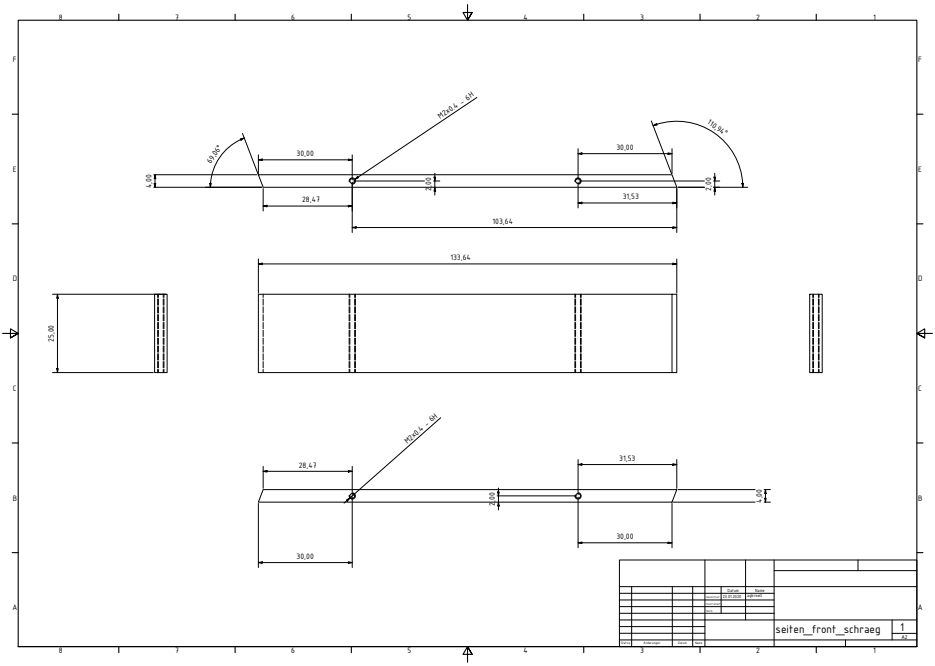

Figure B.10.: Technical drawing of the sloping side plate of a box from the front part of the pair spectrometer.

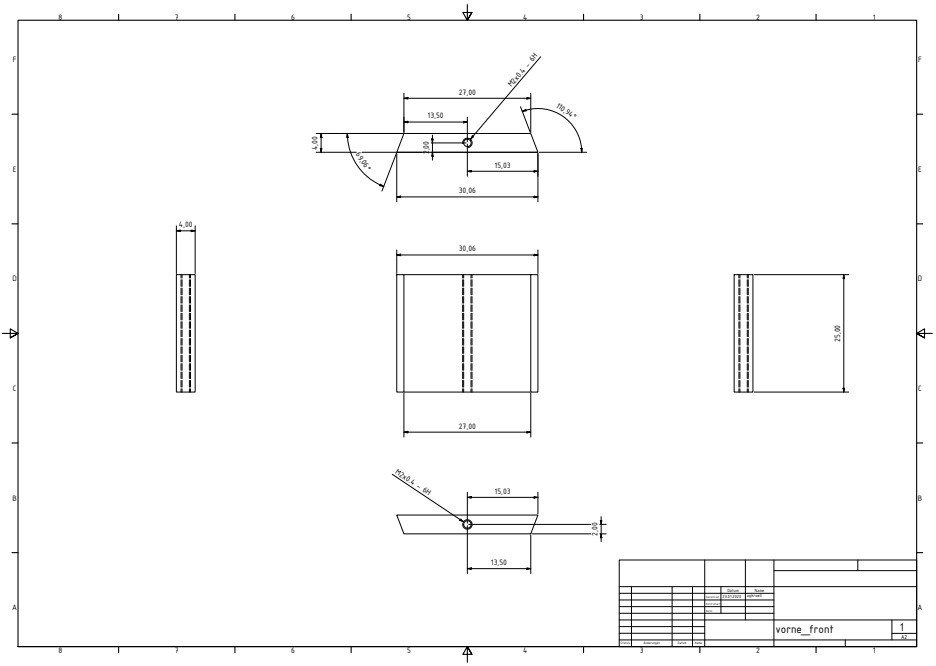

Figure B.11.: Technical drawing of the front plate of a box from the front part of the pair spectrometer.

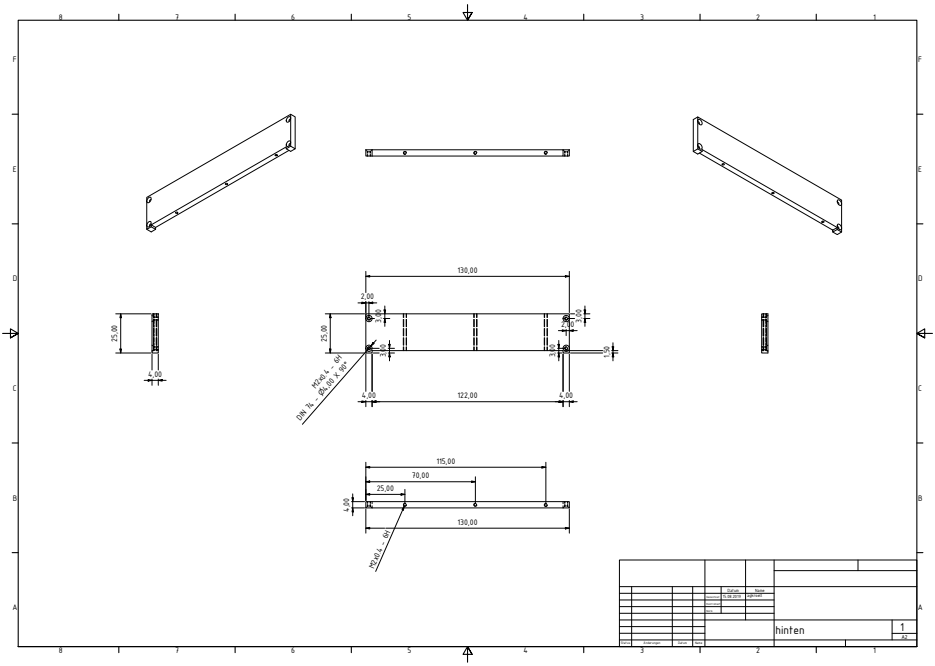

Figure B.12.: Technical drawing of the rear plate of a box from the front part of the pair spectrometer.

C. Miniball Segments

C.1. Single Spectra of each Segment

The Figures in this section show the single spectra from each segment of the Miniball detector. The even numbers belong to the shorter front segments, which show lower statistics for the FE peaks compared to the SE or DE peaks. The back segments with the odd numbers are longer and have a higher ratio of FE peak to SE or DE peak.

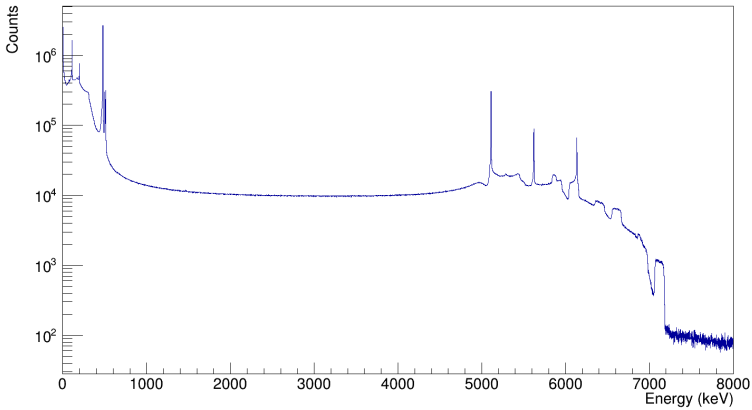

Figure C.1.: Spectrum of segment 0 from the Miniball detector taken during the LiF(p,γ) reaction.

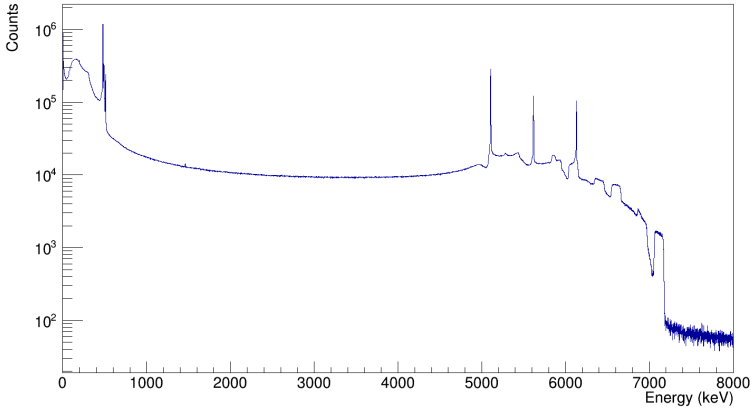

Figure C.2.: Spectrum of segment 1 from the Miniball detector taken during the LiF(p, γ) reaction.

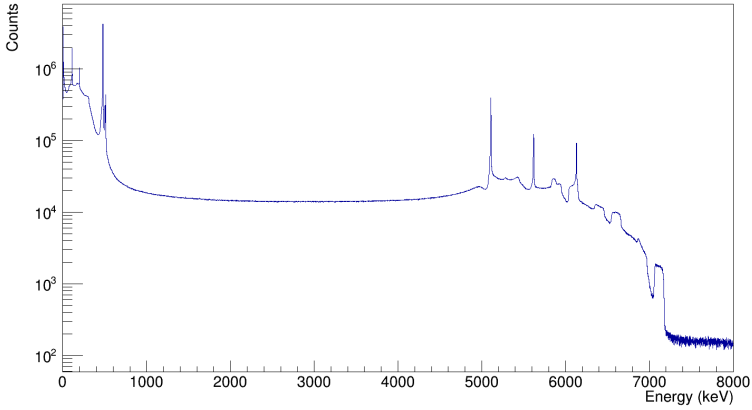

Figure C.3.: Spectrum of segment 2 from the Miniball detector taken during the LiF(p, γ) reaction.

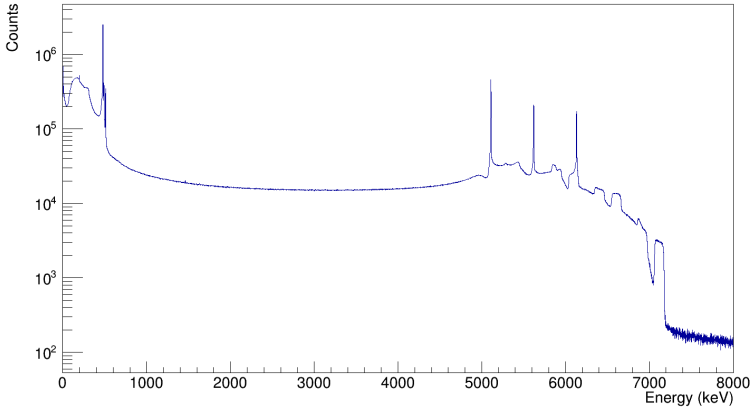

Figure C.4.: Spectrum of segment 3 from the Miniball detecto taken during the LiF(p, γ) reaction.

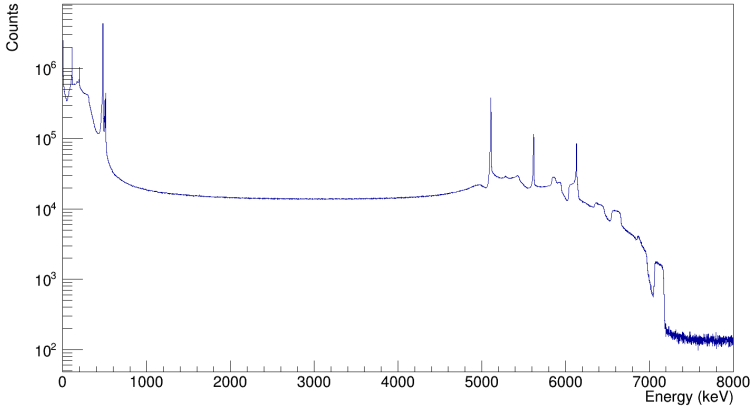

Figure C.5.: Spectrum of segment 4 from the Miniball detector taken during the LiF(p, γ) reaction.

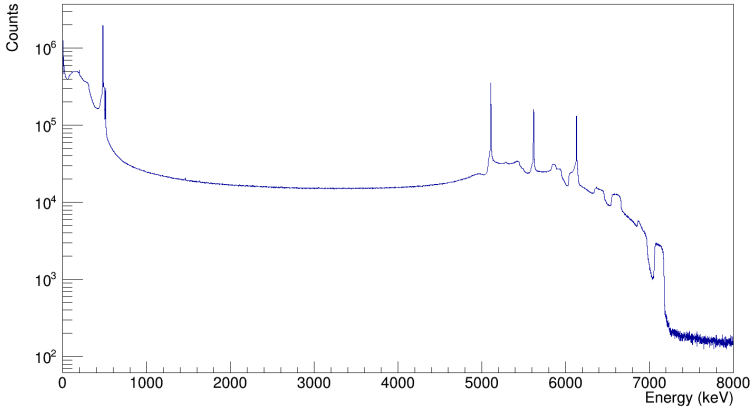

Figure C.6.: Spectrum of segment 5 from the Miniball detector taken during the LiF(p, γ) reaction.

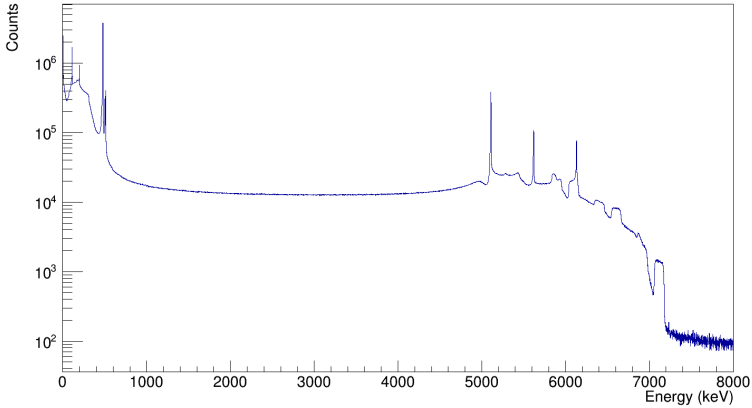

Figure C.7.: Spectrum of segment 6 from the Miniball detector taken during the LiF(p, γ) reaction.

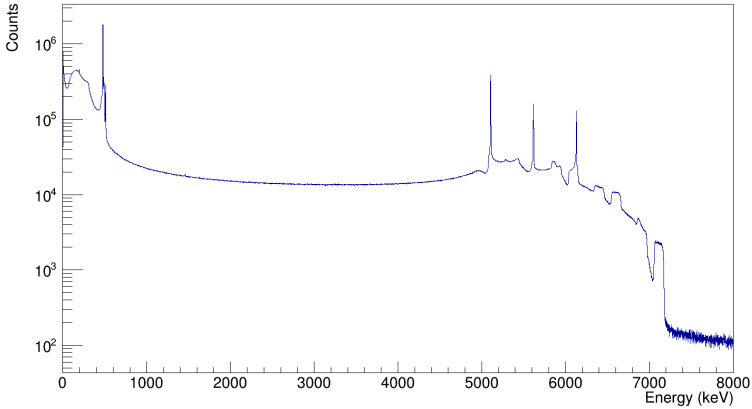

Figure C.8.: Spectrum of segment 7 from the Miniball detector taken during the LiF(p,γ) reaction.

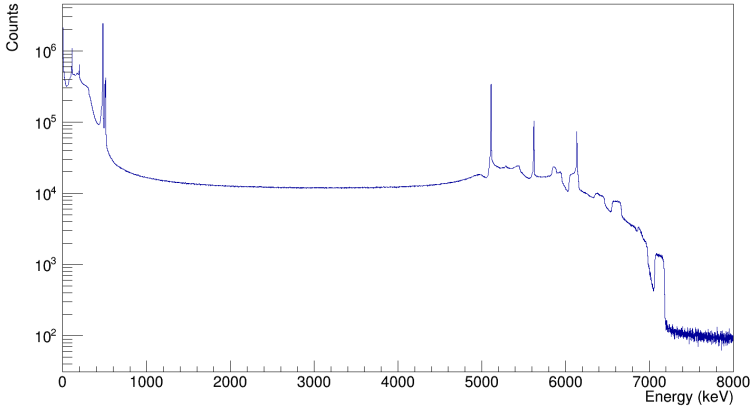

Figure C.9.: Spectrum of segment 8 from the Miniball detector taken during the LiF(p,γ) reaction.

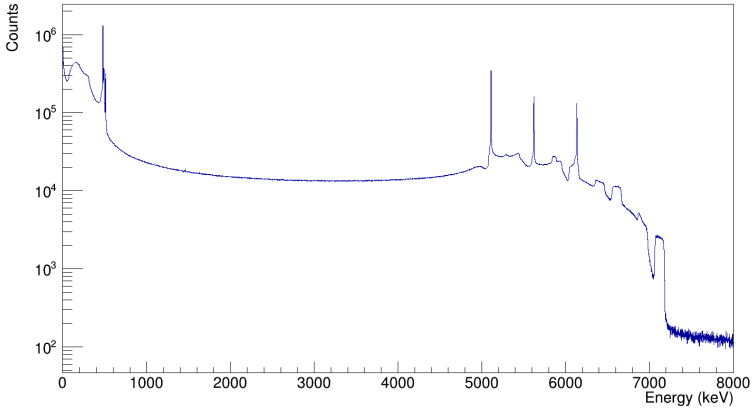

Figure C.10.: Spectrum of segment 9 from the Miniball detector taken during the LiF(p, γ) reaction.

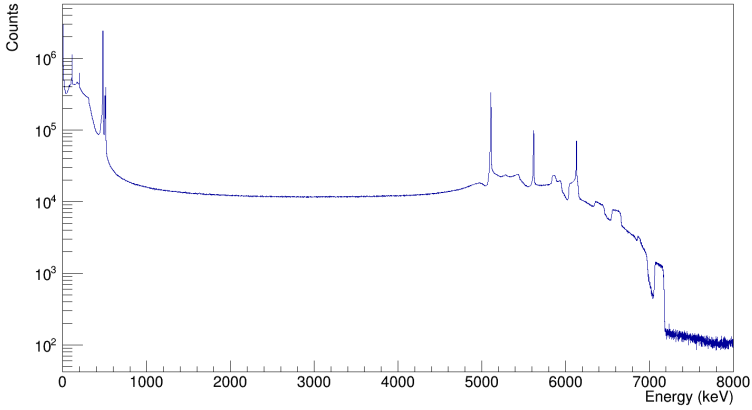

Figure C.11.: Spectrum of segment 10 from the Miniball detector taken during the LiF(p, γ) reaction.

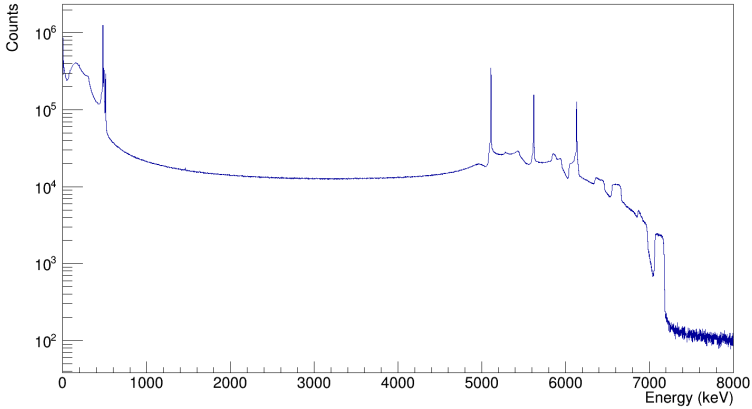

Figure C.12.: Spectrum of segment 11 from the Miniball detector taken during the LiF(p, γ) reaction.

C.2. Correlation Plot of back BGOs in coincidence with each Segment gated on 5.1 MeV

This section shows the correlation plots of the back BGOs that detected 511 keV in coincidence with a 5.1 MeV γ ray in each segment. The numbering of BGOs and segments is shown in Fig. 4.11.

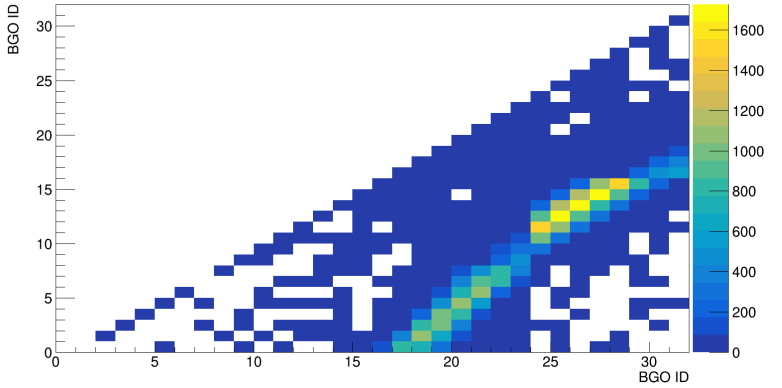

Figure C.13.: Correlation plot of the back BGOs that detected 511 keV γ rays in coincidence with the double-escape peak at 5.1 MeV from the Miniball segment number 0.

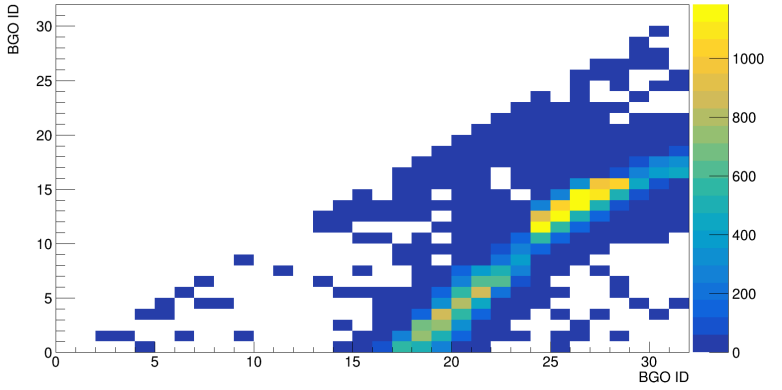

Figure C.14.: Correlation plot of the back BGOs that detected 511 keV γ rays in coincidence with the double-escape peak at 5.1 MeV from the Miniball segment number 1.

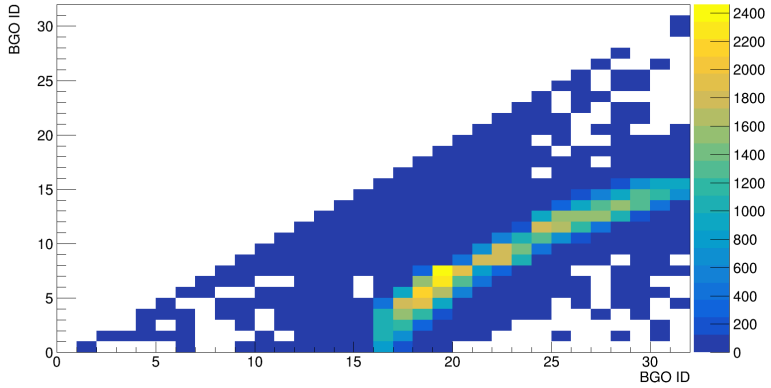

Figure C.15.: Correlation plot of the back BGOs that detected 511 keV γ rays in coincidence with the double-escape peak at 5.1 MeV from the Miniball segment number 2.

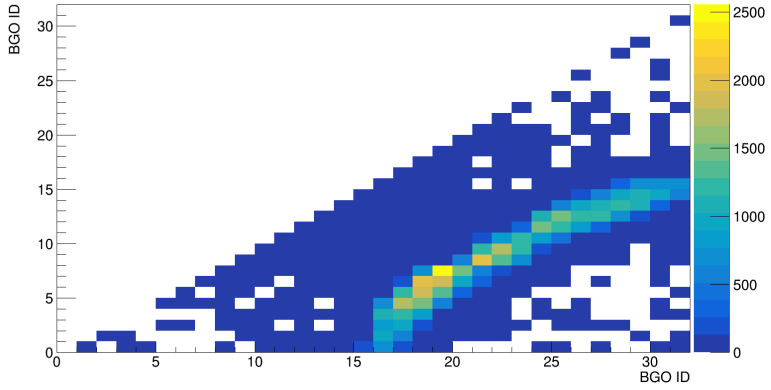

Figure C.16.: Correlation plot of the back BGOs that detected 511 keV γ rays in coincidence with the double-escape peak at 5.1 MeV from the Miniball segment number 3.

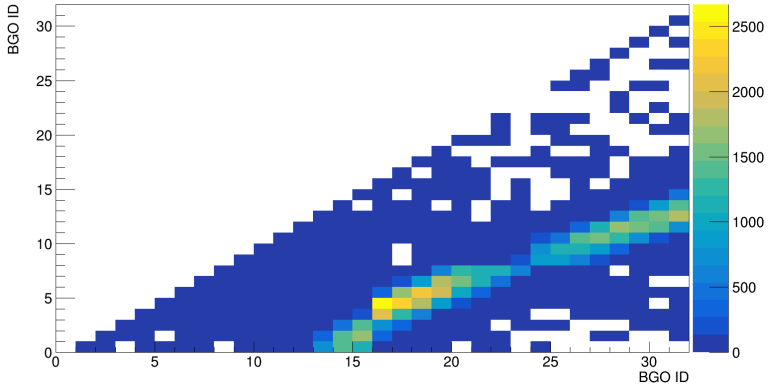

Figure C.17.: Correlation plot of the back BGOs that detected 511 keV γ rays in coincidence with the double-escape peak at 5.1 MeV from the Miniball segment number 4.

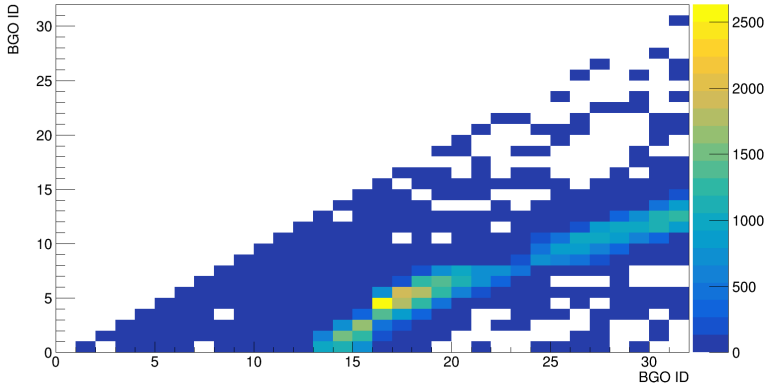

Figure C.18.: Correlation plot of the back BGOs that detected 511 keV γ rays in coincidence with the double-escape peak at 5.1 MeV from the Miniball segment number 5.

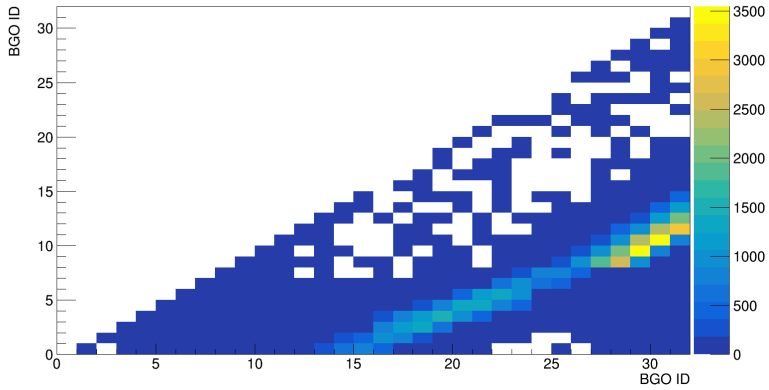

Figure C.19.: Correlation plot of the back BGOs that detected 511 keV γ rays in coincidence with the double-escape peak at 5.1 MeV from the Miniball segment number 6.

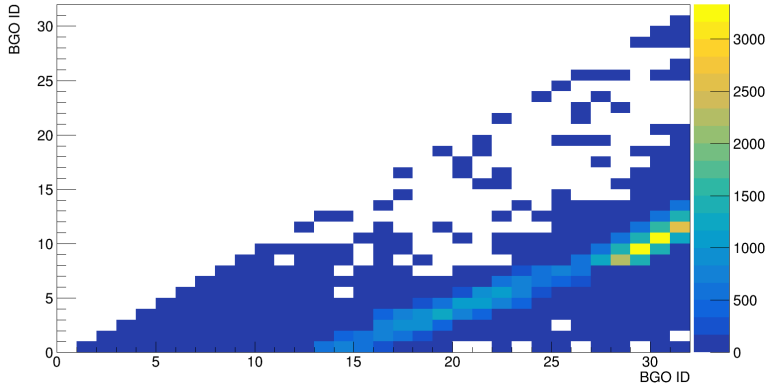

Figure C.20.: Correlation plot of the back BGOs that detected 511 keV γ rays in coincidence with the double-escape peak at 5.1 MeV from the Miniball segment number 7.

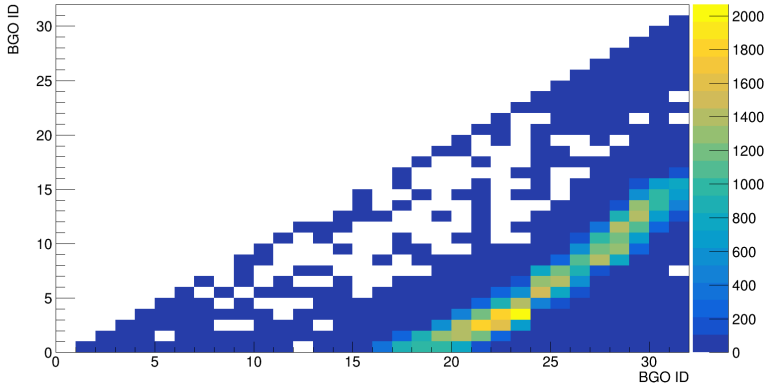

Figure C.21.: Correlation plot of the back BGOs that detected 511 keV γ rays in coincidence with the double-escape peak at 5.1 MeV from the Miniball segment number 8.

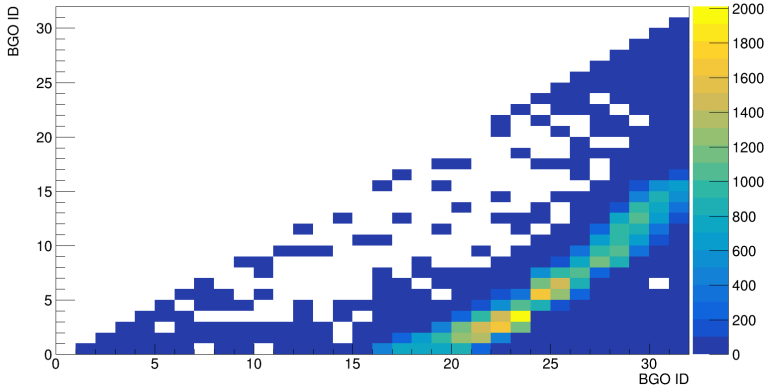

Figure C.22.: Correlation plot of the back BGOs that detected 511 keV γ rays in coincidence with the double-escape peak at 5.1 MeV from the Miniball segment number 9.

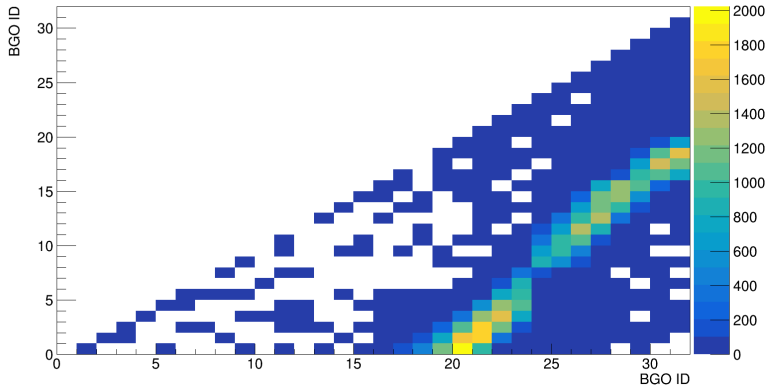

Figure C.23.: Correlation plot of the back BGOs that detected 511 keV γ rays in coincidence with the double-escape peak at 5.1 MeV from the Miniball segment number 10.

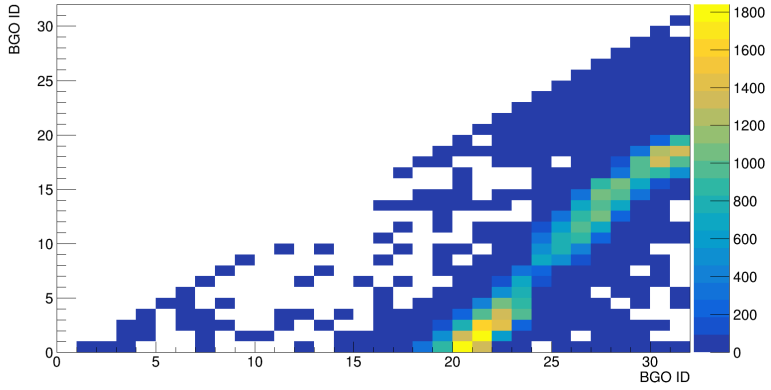

Figure C.24.: Correlation plot of the back BGOs that detected 511 keV γ rays in coincidence with the double-escape peak at 5.1 MeV from the Miniball segment number 11.

C.3. Correlation Plot of front BGOs in coincidence with all Segments

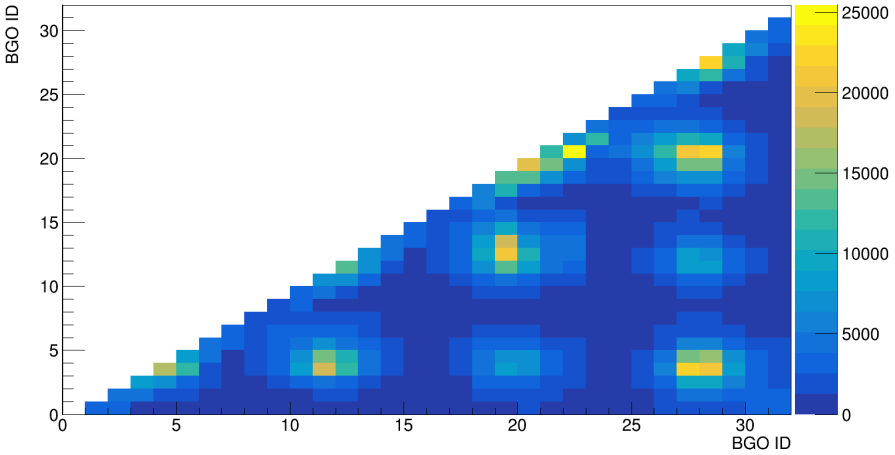

Figure C.25.: Correlation plot of the front BGOs that detected 511 keV γ rays in coincidence with all of the Miniball segments.

D. Clover Crystals

D.1. Single Spectra of each Clover Crystal

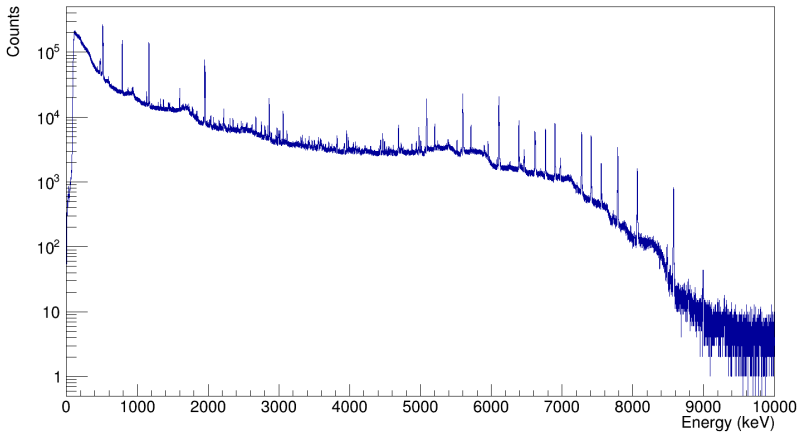

Figure D.1.: NaCl spectrum of clover crystal 0.

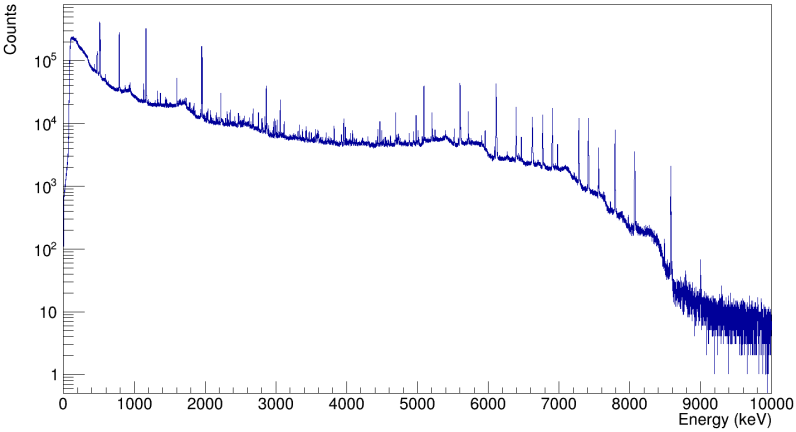

Figure D.2.: NaCl spectrum of clover crystal 1.

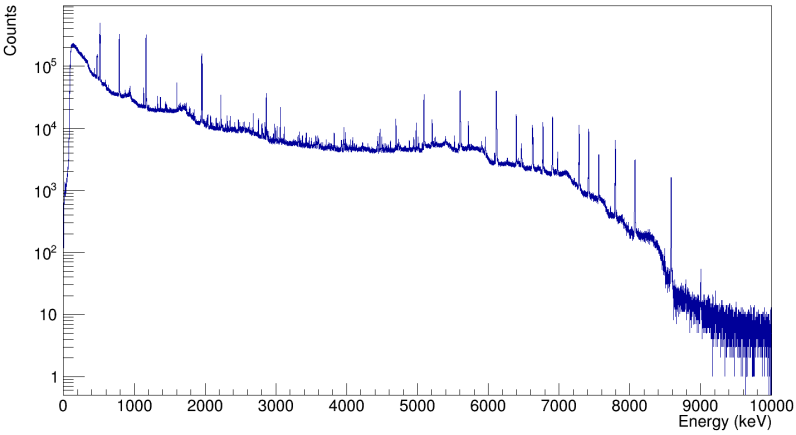

Figure D.3.: NaCl spectrum of clover crystal 2.

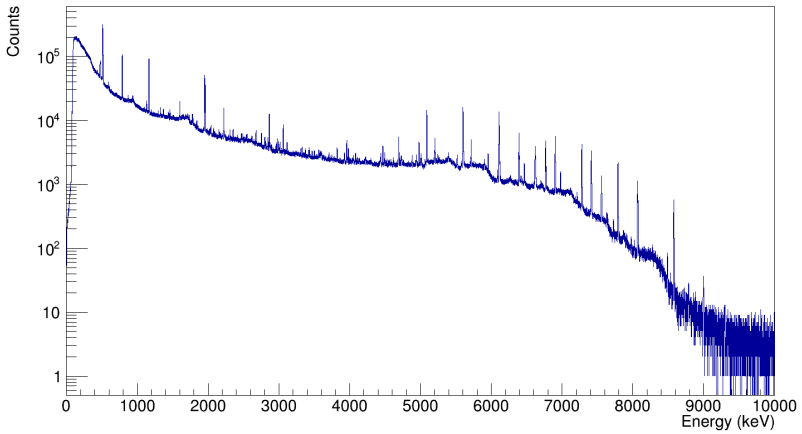

Figure D.4.: NaCl spectrum of clover crystal 3.

D.2. Correlation Plot of front BGOs in coincidence with each Crystal gated on 5.1 MeV

This section shows the correlation plots of the front BGOs that detected 511 keV in coincidence with a 5.1 MeV γ ray in each clover crystal. The numbering of BGOs and clover crystals is shown in Fig. 4.27.

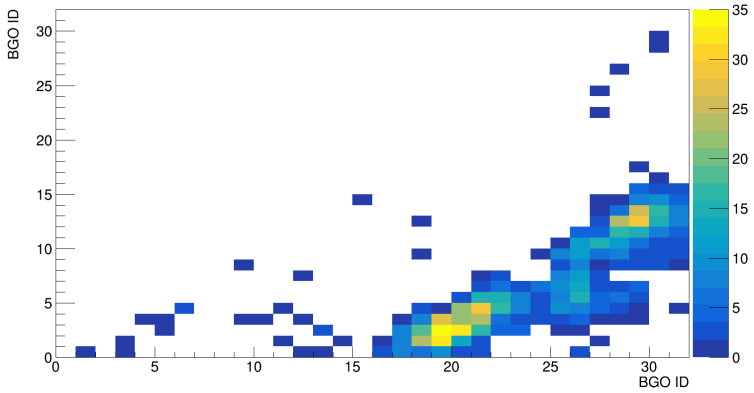

Figure D.5.: Correlation plot of the front BGOs that detected 511 keV γ rays in coincidence with the double-escape peak at 5.1 MeV from the clover crystal 0.

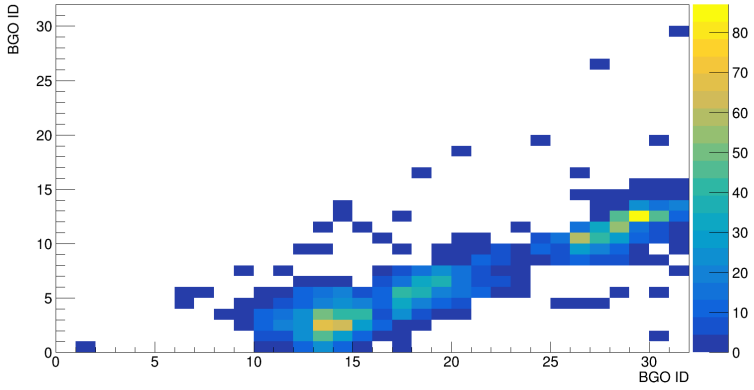

Figure D.6.: Correlation plot of the front BGOs that detected 511 keV γ rays in coincidence with the double-escape peak at 5.1 MeV from the clover crystal 1.

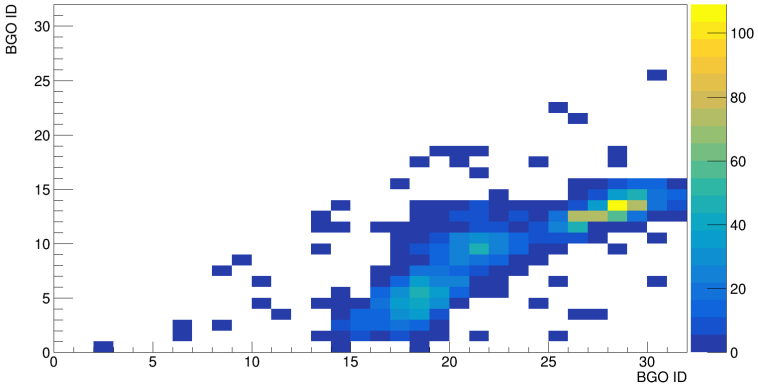

Figure D.7.: Correlation plot of the front BGOs that detected 511 keV γ rays in coincidence with the double-escape peak at 5.1 MeV from the clover crystal 2.

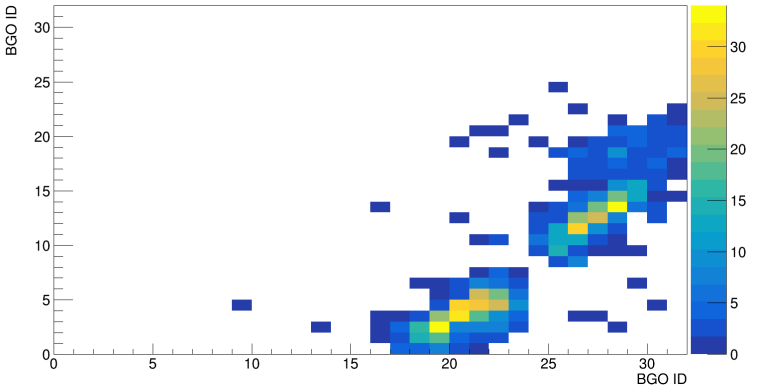

Figure D.8.: Correlation plot of the front BGOs that detected 511 keV γ rays in coincidence with the double-escape peak at 5.1 MeV from the clover crystal 3.

E. Instruction Manual for the Pair Spectrometer

E.1. Assembly

The pair spectrometer is divided in 8 boxes each with 8 BGO crystals inside. Boxes 1-4 built the rectangular back part of the spectrometer and boxes 5-8 form the front part (see Fig. E.2). Standing in front of the pair spectrometer and looking to its front the BGO crystals in the box are positioned from left to right with increasing numbers and the boxes should be set up starting from box 1 at the top and boxes 2,3 and 4 following clockwise as a rectangle (see Fig. E.1). The front part boxes should be connected clockwise to the back part boxes. This means box 5 is connected to box 1, box 6 to box 2, 7 to 3 and 8 to 4.

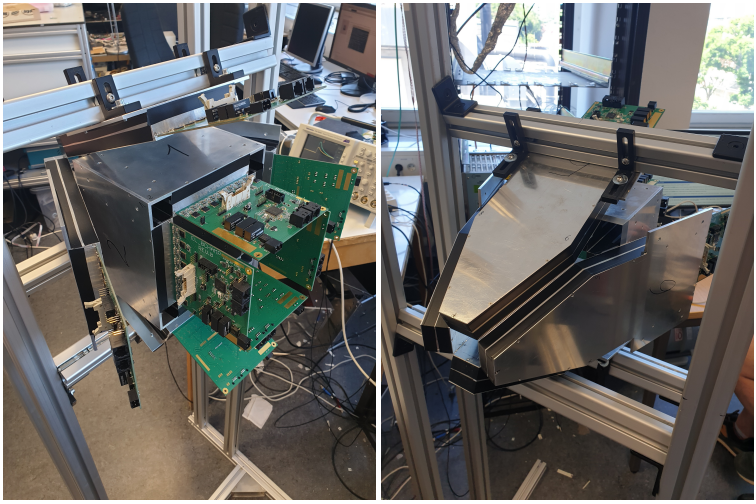

(a) (b)

Figure E.2.: Pictures of the (a) back part and (b) front part of the pair spectrometer with front part connected to the back part.

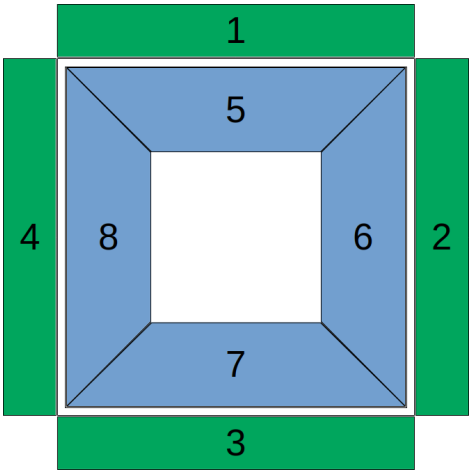

Figure E.1.: Scheme of the positions of the back part (green) and the front part (blue) boxes of the pair spectrometer from the front view.

E.2. Cabling

Box 1 (channels 1-8) and 2 (channels 9-16) should be connected with the flat cable to the first FEBEX card, box 3 (ch. 1-8) and 4 (ch. 9-16) to card 2, box 5 (ch. 1-8) and 6 (ch. 9-16) to card 3 and box 7 (ch. 1-8) and 8 (ch. 9-16) to card 4. Card 5 and higher should be used for additional detectors (see Fig. E.3).

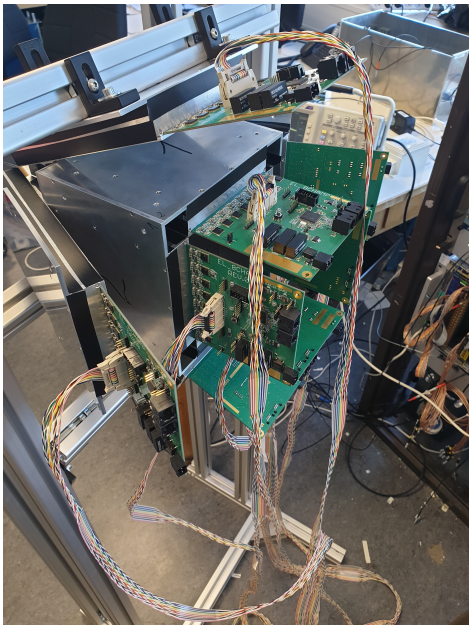

Figure E.3.: Photograph of the flat differential cables connected to the PCBs.

The PEAK CAN controller should be connected via USB with a notebook or some device which can be left in the experimental hall. Further, one has to connect the CAN adapter to one of the PCBs of the boxes (preferred to box 1 (CAN +5V (right socket))) and the rest of the PCBs should also be connected with each other via ethernet cable (see Fig. E.4).

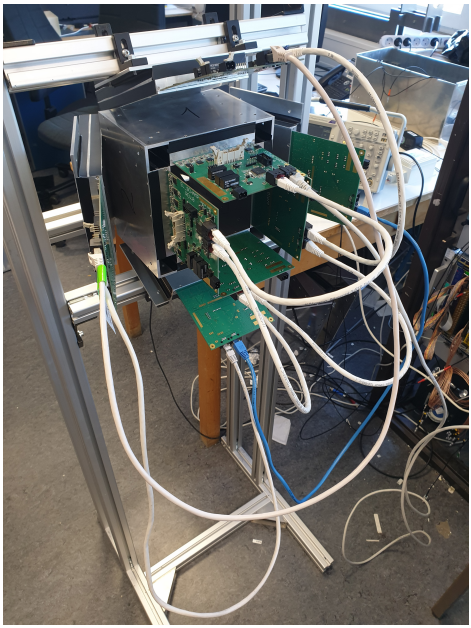

Figure E.4.: Picture of the PCBs connected with each other via Ethernet cables.

The on-board network interface card of the DAQ server (mbsdaq@agkroelldaq) has to be connected to the lab network (to the outside) via “Ethernet connection 1” and the PCIe interface to the first (left) Ethernet port of the lipc-6.

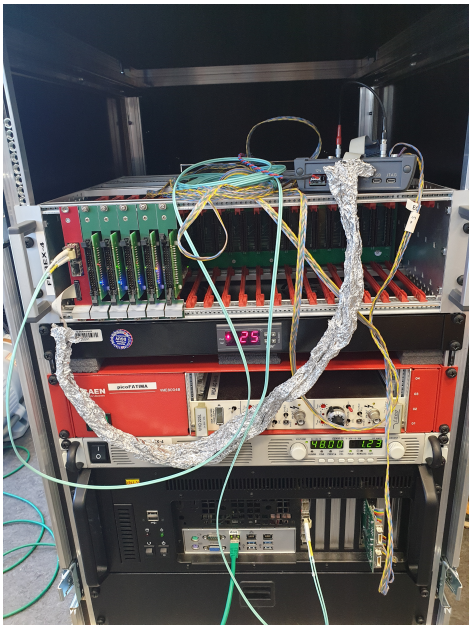

Figure E.5.: Picture of the mobile DAQ system including FEBEX4. The lipc-6 (PC on the bottom) is connected with a green Ethernet cable to the DAQ server (not visible on the picture).

Before booting the DAQ server the 5 TB external hard drive has to be connected otherwise the boot will not work.

E.3. Connection

First the PEAK CAN controller should be set up in the system. On the desktop there is a folder “CAN” with the “start_can0.sh” script which has the necessary commands. Otherwise it is possible to type in the terminal:

- sudo ip link set can0 up type can bitrate 1000000
- candump can0

This terminal can be left open as it will show the commands that are sent to or received from the PCBs.

Then the power cable has to be connected to the PCBs (see Fig. E.6) preferred ONE BY ONE. If more than two PCBs are connected at once and afterwards the plug is inserted it will not switch on the PCBs (maybe the power supply is to weak to turn on all the cards at once). The boxes with the crystals have also to be light-tight, otherwise the PCB of the corresponding box will not work. The terminal with the candump will receive some information from each PCB if it was connected successfully.

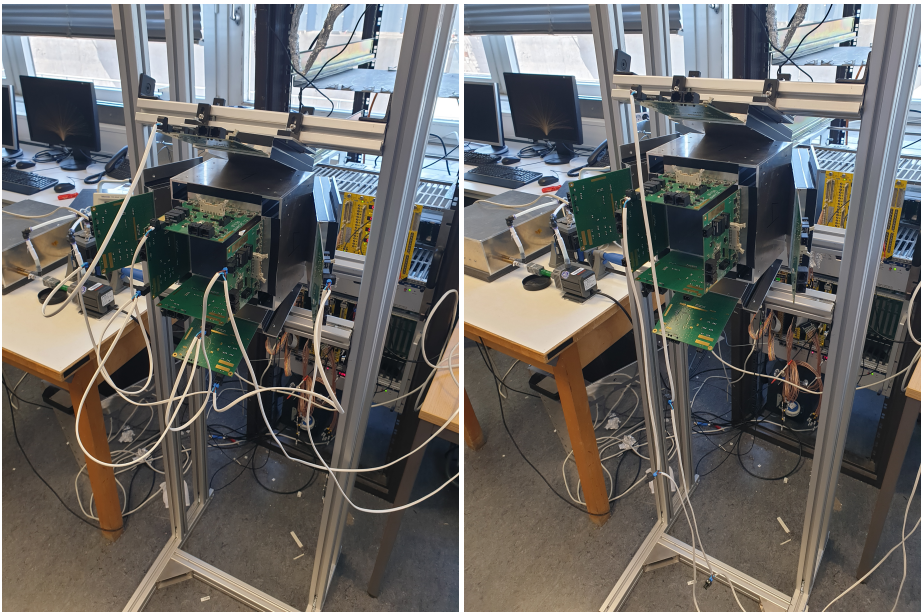

(a) (b)

Figure E.6.: Pictures of (a) two power cables and (b) all eight power cables connected to the PCBs.

Afterwards all the 8 PCBs can be ramped up with the script “rampup_8cards.sh” in the “CAN” folder or by copy and paste the commands from this file. To ramp down the file “rampdown_8cards.sh” can be used.

On the DAQ server it is possible to log in with: Username: mbsdaq PW: agkroell (sudo PW: agkroelldaq)

It is possible to connect from here to the lipc-6:

- ssh lipc-6 (or go2Lipc6)

Then go to folder:

- cd mbsrun/x86_debian/x86_febex4_HS

Start mbs and data acquisition from here:

- mbs
- @startup
- sho acq (shows the number of events)
- @shutdown (shutdown acquisition)
- exit (leave mbs)

In the folder mbsrun/x86_debian/x86_febex4_HS/python_gui is the GUI to control the FEBEX parameters:

- python febex4_gui.py

Open Go4 on the DAQ server and connect to the lipc-6 after the data acquisition is running.

List of Figures

List of Tables

Bibliography

[1] *ELI ERIC*. https://eli-laser.eu/. 19.09.2022.

[2] Călin A. Ur. *ELI-NP: VEGA System*. ELI-NP 1st User Workshop, Magurele. Oct. 2019.

[3] Henry R. Weller. "Research opportunities at the upgraded HIγS facility". In: *Progress in Particle and Nuclear Physics* 62 (2009), pp. 257–303.

[4] *ELI Nuclear Physics*. https://www.eli-np.ro/. 22.02.2021.

[5] *Nuclear resonance fluorescence experiments - ELIADE*. http://www.eli-np.ro/ro/user_experimental_areas.php. 24.04.2023.

[6] H.C. Scraggs et al. "TIGRESS highly-segmented high-purity germanium clover detector". In: *Nucl. Instrum. Methods Phys. Res. A* 543.2 (2005), pp. 431–440.

[7] Michael Thürauf, private communication, 06.01.2016.

[8] *ELIADE - Technical Proposal*. (Unpublished).

[9] Ilja Homm. "Development of a HPGe-BGO Pair Spectrometer for ELI-NP." MA thesis. TU Darmstadt, 2016.

[10] Glenn Frederick Knoll. *Radiation Detection and Measurement*. Fourth Edition. John Willey & Sons, Inc., 2010.

[11] National Institute of Standards and Technology. *Stopping-Power & Range Tables for Electrons, Protons, and Helium Ions*. https://www.nist.gov/pml/stopping-power-range-tables-electrons-protons-and-helium-ions. 04.01.2023.

[12] M. J. Berger, S. M. Seltzer. *Stopping Powers and Ranges of Electrons and Positrons*. https://nvlpubs.nist.gov/nistpubs/Legacy/IR/nbsir82-2550.pdf. 04.01.2023. Aug. 1982.

[13] Konrad Kleinknecht. *Detektoren für Teilchenstrahlung*. Fourth Edition. Vieweg+Teubner Verlag, 2005.

[14] William R. Leo. *Techniques for Nuclear and Particle Physics Experiments*. Springer-Verlag, 1987.

[15] The University of Liverpool. *Relative Efficiency*. https://ns.ph.liv.ac.uk/~ajb/radiometrics/practical_analysis/spectrum_analysis/relative_efficiency.htm. 28.06.2022.

[16] Gábor Talián. *Fluoreszenzspektroskopie*. http://www.biofizika.aok.pte.hu/data/2017/0407/561/FLUORESZENZSPEKTROSKOPIE.pdf. 28.07.2022.

[17] Semiconductor Components Industries, LLC. *Introduction to the Silicon Photmultiplier (SiPM)*. https://www.onsemi.com/pub/Collateral/AND9770-D.PDF. Technical note. July Rev. 8, 2021.

[18] National Institute of Standards and Technology. *XCOM: Photon Cross Sections Database*. https://www.nist.gov/pml/xcom-photon-cross-sections-database. 19.12.2022.

[19] Saint-Gobain Ceramics & Plastics, Inc. *BGO Bismuth Germanate Scintillation Material*. https://www.crystals.saint-gobain.com/sites/imdf.crystals.com/files/documents/bgo-material-data-sheet.pdf. Data sheet. 03.08.2021.

[20] Saint-Gobain Ceramics & Plastics, Inc. *CsI(Tl), CsI(Na) Cesium Iodide Scintillation Material*. https://www.crystals.saint-gobain.com/sites/imdf.crystals.com/files/documents/csitl-and-na-material-data-sheet.pdf. Data sheet. 03.08.2021.

[21] Saint-Gobain Ceramics & Plastics, Inc. *BrilLanCe 380 Scintillation Material*. Data sheet. 2014.

[22] A. Syntfeld-Kazuch et al. "Non-Proportionality and Energy Resolution of CsI(Tl)". In: *IEEE Trans. Nucl. Sci.* 54.5 (2007), pp. 1836–1841.

[23] Microscopy and Microanalysis. *XEDS Tools Solid Angle Calculator*. http://zaluzec.com/NJZTools/XEDSSolidAngleV6.html. 05.07.2022.

[24] SCIONIX. http://scionix.nl. 11.10.2021.

[25] 3M. *Vikuiti™Enhanced Specular Reflector (ESR)*. https://www.digikey.ch/de/pdf/3/3m/3m-vikuiti-enhanced-specular-reflector-esr. Data sheet. 21.06.2022.

[26] Adam Nepomuk Otte et al. "Characterization of three high efficiency and blue sensitive silicon photomultipliers". In: *Nucl. Instrum. Methods Phys. Res. A* 846 (2017), pp. 106–125.

[27] Hamamatsu Photonics K.K. *MPPC for Scintillation*. Product Flyer provided by Christian Dille, Private communication, 13.03.2018.

[28] Hamamatsu Photonics K.K. *Bias power supply with built-in temperature compensation function for MPPC*. https://www.hamamatsu.com/content/dam/hamamatsu-photonics/sites/documents/99_SALES_LIBRARY/ssd/c14156_kacc1265e.pdf. Data sheet. 06.01.2023. May 2022.

[29] PEAK-System Technik GmbH. https://www.peak-system.com/PCAN-USB.199.0.html. 24.06.2022.

[30] Henning Schaffner, private communication, December 2019.

[31] Han-Bum Rhee, private communication, July 2022.

[32] Diandra Richter. *Simulation eines Paarspektrometers zum Einsatz als Intensitätsmonitor für einen γ-Strahl*. Bachelor's thesis. TU Darmstadt, 2022.

[33] Eckert & Ziegler. *Overview - point sources*. https://www.ezag.com/home/products/isotope_products/isotrak_calibration_sources/reference_sources/gamma_sources/point_sources/. 04.07.2022.

[34] *Data of ^{22}Na*. https://www.nndc.bnl.gov/ensdf/. 04.07.2022.

[35] *Data of ^{40}K*. https://www.nndc.bnl.gov/nudat3/getdecayscheme.jsp?nucleus=40AR&dsid=40k%20ec%20decay%20(1.248eP9%20y)&unc=nds. 11.01.2023.

[36] Heiko Scheit. "The New Radioactive Nuclear Beam Facility REX-ISOLDE/MINIBALL: Sub-Barrier Coulomb Excitation of ^{30,32}Mg and the "Island of Inversion"". Habilitation. Ruprecht-Karls-Universität Heidelberg, 2005.

[37] N. Warr et al. "The Miniball spectrometer". In: *Eur. Phys. J. A* 49 (2013), pp. 1–32.

[38] Bart Bruyneel. "Characterization of Segmented Large Volume, High Purity Germanium Detectors". PhD thesis. Universität zu Köln, 2006.

[39] Christoph Fransen, private communication, April 2021.

[40] R. J. Van de Graaff. "Tandem Electrostatic Accelerators". In: *Nucl. Instrum. Methods* 8.2 (1960), pp. 195–202.

[41] D. B. Tridapalli et al. "^{19}F$(p,)^{16}$O reaction: HPGe detector response function and gamma-rayrelative yields". In: International Conference on Nuclear Data for Science and Technology. 2007.

[42] A. J. Krasznahorkay et al. "On the X(17) light-particle candidate observed in nuclear transitions". In: *Acta Physica Polonica B* 50.3 (2019), pp. 675–684.

[43] G. M. Lerner and J. B. Marion. "Measurement of (p,p) and (p,α) cross sections for lithium and fluorine". In: *Nucl. Instrum. Methods* 69.1 (1969), pp. 115–121.

[44] Jian-Jun He et al. "Thermonuclear ^{19}F(p,α_0)^{16}O reaction rate". In: *Chinese Phys. C* 42.1 (2018), p. 015001.

[45] D. Zhanow et al. "The $S(E)$ factor of ^{7}Li(p,γ)^{8}Be and consequences for $S(E)$ extrapolation in ^{7}Be(p,γ_0)^{8}B". In: *Z. Phys. A* 351 (1995), pp. 229–236.

[46] T. Saito et al. “Measurement of thick-target gamma-ray production yields of the ^{7}Li$(p,p')^{7}$Li and ^{7}Li$(p,)^{8}$Be reactions in the near-threshold energy region for the ^{7}Li$(p,n)^{7}$Be reaction”. In: *Journal of Nuclear Science and Technology* 54.2 (2017), pp. 253–259. ISSN: 0022-3131.

[47] A. Knyazev et al. “Properties of the CsI(Tl) detector elements of the CALIFA detector”. In: *Nucl. Instrum. Methods Phys. Res. A* 940 (2019), pp. 393–404.

[48] Stefanie Christine Hellgartner. “Probing Nuclear Shell Structure beyond the $N = 40$ Subshell using Multiple Coulomb Excitation and Transfer Experiments”. PhD thesis. Technische Universität München, 2015.

[49] Corinna Henrich. “Investigation of collectivity in the neutron-rich $^{1}42$Xe”. PhD thesis. Technische Universität Darmstadt, 2020.

[50] M. Descovich et al. “Effects of neutron damage on the performance of large volume segmented germanium detectors”. In: *Nucl. Instrum. Methods Phys. Res. A* 545 (2005), pp. 199–209.

[51] Caterina Michelagnoli, private communication, October 2022.

[52] B. Krusche et al. “Gamma ray Energies and ^{36}Cl level scheme from the reaction ^{35}Cl(n,γ)”. In: *Nucl. Phys. A* 386 (1982), pp. 245–268.

[53] R. B. Firestone. “Thermal neutron capture cross sections and neutron separation energies for ^{23}Na(n,γ)”. In: *Phys. Rev. C* 89.014617 (2014).

[54] R. B. Firestone. “Comparison of IUPAC k_0 values and neutron cross sections to determine a self-consistent set of data for neutron activation analysis”. In: *Proc. Radiochim. Acta* 1 (2011), pp. 305–312.

[55] *Data of ^{36}Cl*. `https://www.nndc.bnl.gov/nudat3/getdataset.jsp?nucleus=36Cl&unc=NDS`. 20.01.2023.

[56] GEANT4 collaboration. “GEANT4 - a simulation toolkit”. In: *Nucl. Instrum. Methods Phys. Res. A* 506.3 (2003), pp. 250–303.

[57] J. Allison et al. “Geant4 Developments and Applications”. In: *IEEE Trans. Nucl. Sci.* 53.1 (2006), pp. 270–278.

[58] J. Allison et al. “Recent developments in GEANT4”. In: *Nucl. Instrum. Methods Phys. Res. A* 835 (2016), pp. 186–225.

[59] *GEANT4*. `https://geant4.web.cern.ch/`. 19.01.2023.

[60] Hans J. Ache. “Chemistry of the Positron and of Positronium”. In: *Angewandte Chemie International Edition in English* 11.3 (1972), pp. 179–199.

[61] A.M. Baxter et al. “Compton-suppression tests on Ge and BGO prototype detectors for GAMMASPHERE”. In: *Nucl. Instrum. Methods Phys. Res. A* 317 (1992), pp. 101–110.

[62] M. Lebois et al. “The ν-ball γ-spectrometer”. In: *Nucl. Instrum. Methods Phys. Res. A* 960 (2020), p. 163580.

[63] M.A. Schumaker et al. “Measured and simulated performance of Compton-suppressed TIGRESS HPGe clover detectors”. In: *Nucl. Instrum. Methods Phys. Res. A* 570.3 (2007), pp. 437–445.

[64] D. Rosiak et al. “Escape-suppression shield detector for the MINIBALL γ-ray spectrometer”. In: *Eur. Phys. J. A* 55.4 (2019), p. 48.

[65] Călin A. Ur et al. “Nuclear Resonance Fluorescence Experiments at ELI-NP”. In: *Romanian Reports in Physics* 68 (2016), pp. 483–538.

[66] M. Jentschel et al. “Measurements of the pair production cross section close to the threshold energy.” In: *Phys. Rev. C* 84.052501(R) (2011).

Acknowledgement

First of all I would like to thank my supervisor Thorsten Kröll for giving me the opportunity to do my doctoral thesis in his group as well as for his support and patience.

A big thank you goes also to my working group, especially to Corinna Henrich, Han-Bum Rhee, Matthias Rudigier and Martin von Tresckow, who helped me a lot with the experiments, the analysis and other important issues.

I am grateful to the people at the University of Cologne and at the ILL, who gave us the possibility to perform our experiments at their sites and helped us before, during and after the measurements.

For the very important non-physical support and entertainment, especially during the coffee breaks I would like to thank Rudi Homm, Tobias Klaus, Marcus Wunderle and Sergej Bassauer.

Last but not least, special thanks to my wife, my parents and my brother, who have been a great moral support for me all these years and helped me a lot, where it was necessary.